Study of Particle Interaction in Matter, Gas based Detector Development and Simulation

A thesis Submitted
in Partial Fulfilment of the Requirements
for the Degree of

MASTER OF SCIENCE

by

ROHITH SARADHY

to the

School of Physical Sciences

National Institute of Science Education and Research

Bhubaneswar

24th April, 2017

For my parents,
even though they never bought me a robot

DECLARATION

I hereby declare that I am the sole author of this thesis in partial fulfillment of the requirements for a postgraduate degree from National Institute of Science Education and Research (NISER). I authorize NISER to lend this thesis to other institutions or individuals for the purpose of scholarly research.

Signature of the Student

Date:

The thesis work reported in the thesis entitled .....
was carried out under my supervision, in the school of .....
at NISER, Bhubaneswar, India.

Signature of the thesis supervisor

School:

Date:

ACKNOWLEDGEMENTS

I thank Professor Bedangadas Mohanty for giving me the opportunity to study and develop detectors, for giving me invaluable knowledge and insight into the field and guiding me towards the right direction each time I went astray.

I would like to thank Dr. Satyanarayana Bheesette for providing the help and guidance as well as the facilities in TIFR for fabricating and testing the RPC.I thank Mr. Ravindra Shinde without whose help, this developing the RPC would not have been possible.

I thank Prof. P.V Satyam, who suggested to me to build a two windowed proportional counter for the detection of Molybdenum X-rays. Along with this he also provide the facilities for testing and developing the detector.

I thank Dr. Varchaswi K S Kashyap and Dr. Meghna KK, for all the help they provided and this project would not have been possible if it weren't for them.

Last but not the least, I thank Dr. Chitrasen Jena, Dr. Ranbir Singh, Dr. Ashwini Kumar,Mr B.K Dash, Mr Samir Banik, Mr Vipul Bairathi, Mr Kishora Nayak, and Mr Amit Nanda who helped me with the concepts and practical problems that I faced. Discussion with them improved my understanding of the topics immensely.

ABSTRACT

We have studied the interaction of radiation with matter as well as the simulation and development of gaseous detectors: Resistive Plate Chamber(RPC) and Proportional Counter. In the first part we deal with the study of charged particle interaction mainly using the Bethe-Bloch equation. After which, we developed and characterised a 15×15 cm^2 bakelite RPC. Leakage current, efficiency, and noise rate have been studied. This was followed by the simulation of the same geometry using Geant4 for different charged particles. The effect of gas composition as well as the gap length were studied for protons of different energies. We extended the study of interaction of radiation by including the interactions of neutral particles like photons and neutrons. We designed, simulated and developed a double windowed proportional counter for the study of 17.5 keV X-rays for ongoing research purposes. The counter was tested in the X-ray diffractometer facility in the Institute of Physic, Bhubaneswar.

Contents

List of Figures

List of Tables

Chapter 1

Charged Particle Interaction

Our aim is to study, develop and test detectors and for this reason it is wise to first revise how different types of particles deposit energy in matter. The simplest of case is to study the charged particle interaction with matter which we shall cover in this chapter. A plethora of mechanisms can be utilised to convert the energy deposited into a detectable signal like fluorescent materials, chemical transformations intervening in photographic emulsions, condensation of droplets in saturated vapours or acoustic shock waves are but just a few examples [1].

In charged particle interaction, most of the energy dissipation is due to the electromagnetic interaction of the Coulombic fields of the incoming particles with that of the molecules of the medium[2]. And majority of the collisions that account for the energy deposition are due to multiple inelastic processes of excitation and ionisation; except for when the particles approach the end of their range where elastic process takes over.

These inelastic collisions are statistical in nature and here we shall work out the mean energy deposited per unit path length. This quantity is often called the Stopping Power or simply $\frac{dE}{dx}$ [2]. One of the first calculations were done by Niels Bohr(1913) using classical arguments, and later Bethe(1930), Bloch(1933) and others using quantum mechanics.[1]

1.1 Collisional Energy Loss of Massive Charged Particle

For an incoming particle of mass m_p, with velocity $v = \beta c$, charge number z (coefficient that, when multiplied by the elementary charge, gives the charge of the incoming projectile), and, thus charge ze. The theoretical expression for energy loss by inelastic collision is given by 1.1

$$-\frac{dE}{dx} = \frac{2\pi n z^2 e^4}{mv^2}\left\{ln\left[\frac{2mv^2W_m}{I^2(1-\beta^2)}\right] - 2\beta^2 - \delta - U\right\} \tag{1.1}$$

where m is the electron mass(we are deviating from the standard convention of m_e); n is the number of electrons per cm^3 of the transversed material,I is the mean excitation potential of the atoms of the material, W_m is the maximum transferable energy from the incident particles to the atomic electron(relativistic), δ is the correction for the density-effect, and U is the Shell Correction due to the non-participation of electrons of inner shells for very low incoming kinectic energies. If N is the Avagadro constant, ρ is the absorber density, in g/cm^3, and A is the atomic weight, then the number of electrons per cm^3, n, is given by 1.2

$$n = \frac{ZN\rho}{A} \tag{1.2}$$

For heavy particle , the collisional energy-loss dE/dx is also referred to as the stopping power and the negative sign implies the energy is lost by the particle.

1.1.1 Two Body Scattering

Collisions can be considered as a two body scattering in which the target particle(here it is the atomic electron) can be considered to be at rest. Let the incident particle have mass m and momentum $\vec{p}$, and a target particle of mass m_e at rest. After the interaction, two scattered particles emerge: the former with mass m and the momentum $\vec{p}'$ and the latter with mass m_e and momentum $\vec{p}'$. The latter has the direction of motion forming an angle θ with the incoming particle direction as shown in figure 1.1. θ is the angle at which the particle is scattered. The kinectic energy of

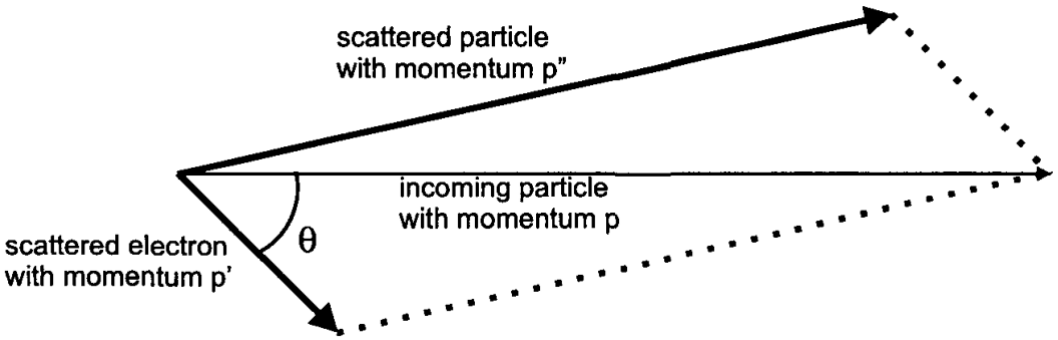

Figure 1.1: Incident particle of mass m and momentum[1]t

the scattered particle is related to its momentum by

$$E_k + m_e c^2 = \sqrt{p'^2 c^2 + m_e^2 c^4} \tag{1.3}$$

from which we get

$$p'^2 = \frac{(E_k + m_e c^2)^2 - m_e^2 c^4}{c^2} \tag{1.4}$$

Using the total energy conservation

$$\sqrt{p^2 c^2 + m^2 c^4} + m_e c^2 = \sqrt{p''^2 c^2 + m^2 c^4} + E_k + m_e c^2 \tag{1.5}$$

or

$$\sqrt{p''^2 c^2 + m^2 c^4} = \sqrt{p^2 c^2 + m^2 c^4} - E_k \tag{1.6}$$

and from momentum conservation

$$\vec{p}'' = \vec{p} - \vec{p}' \implies p''^2 = p^2 + p'^2 - 2pp' \cos\theta \tag{1.7}$$

Eqn 1.7 can be rewritten using eqn 1.4 to get

$$p''^2 = p^2 + \frac{(E_k + m_e c^2)^2 - m_e^2 c^4}{c^2} - 2p\cos\theta \sqrt{\frac{(E_k + m_e c^2)^2 - m_e^2 c^4}{c^2}} \tag{1.8}$$

and substituting in eqn 1.6 and squaring both sides of that equation we get

$$E_k \sqrt{p^2 c^2 + m^2 c^4} = -E_k m_e c^2 + pc\cos\theta \sqrt{(E_k + m_e^2 c^4)} \tag{1.9}$$

and

$$pc\cos\theta \sqrt{\frac{E_k^2 + 2E_k m_e c^2}{E_k^2}} = m_e c^2 + \sqrt{p^2 c^2 + m^2 c^4} \tag{1.10}$$

Now finally squaring both sides of the equation, we can derive the expression for the kinetic energy E_k of the scattered target particle as

$$E_k = \frac{2m_e c^4 p^2 \cos^2\theta}{(m_e c^2 + \sqrt{p^2c^2 + m^2c^4})^2 - p^2c^2\cos^2\theta} \tag{1.11}$$

From eqn 1.11 we note that the maximum energy transfer is for $\theta = 0$, i.e., when a head-on collision occurs. Then Eqn 1.11 becomes

$$W_m = \frac{p^2c^2}{\frac{1}{2}m_e c^2 + \frac{1}{2}(m^2/m_e)c^2 + \sqrt{p^2c^2 + m^2c^4}} \tag{1.12}$$

And we know the total energy of the particle can be written as

$$E = m\gamma c^2 = \sqrt{p^2c^2 + m^2c^4} \tag{1.13}$$

Implying that 1.12 can be written as

$$W_m = 2m_e c^2 \beta^2\gamma^2 \Big[1 + \Big(\frac{m_e}{m}\Big)^2 + 2\gamma\frac{m_e}{m}\Big]^{-1} \tag{1.14}$$

For massive particles whose masses are much much greater than electron mass we have $m \gg m_e$. At lower energies (p is $\ll \frac{m^2}{m_e}c$)the max energy can be approximated to

$$W_m \approx 2m_e c^2\beta^2\gamma^2 \tag{1.15}$$

1.1.2 Derivation of Stopping Power

Using equation 1.15 and substituting in equation 1.1 we get

$$-\frac{dE}{dx} = \frac{4\pi n z^2 e^4}{mv^2}\left\{ln\Big[\frac{2mv^2\gamma^2}{I}\Big] - \beta^2 - \delta/2 - U/2\right\} \tag{1.16}$$

We shall derive this formula following closely the previous approaches by [Fermi (1950); Sternheimer (1961); Fernow (1986)]. One of the assumptions is that the incoming particle will not deviate from the initial trajectory(i.e.,only a small fraction of K.E is transferred to the electron.)

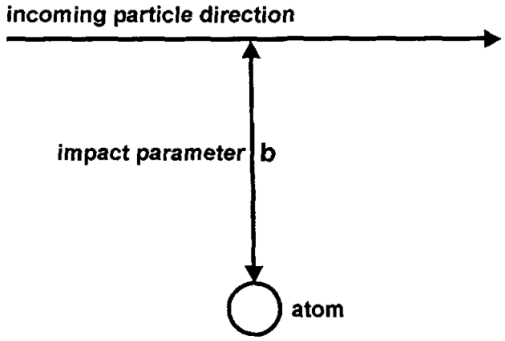

Figure 1.2: Impact parameter b is the minimum distnace between the incoming particle and the target by which it is scattered[1]t

Fig 1.2 shows the impact parameter, which is the minimal distance of the incoming particle to the target electron. In general, large b values correspond to the distant collisions, and small b values to close collision. We assume the electron to essentially be at rest throughout the interaction. This way, because of symmetry the transferred impulse $I_\perp$ will be almost along the direction perpendicular to the particle trajectory. We also assume that the interaction time is inversely proportional to v and directly proportional to b i.e., $\approx \frac{b}{v}$. In equation 1.17, $F_\perp$, and $E_\perp$ are the perpendicular(to the incident particle velocity) force and electric field that acts on the electron.

$$I_\perp = \int F_\perp dt = e \int E_\perp \frac{dt}{dx} dx = e \int E_\perp \frac{dx}{v} \tag{1.17}$$

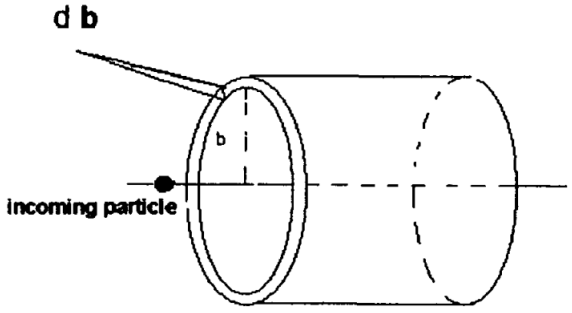

Figure 1.3: An incoming fast particle of charge ze interacts with electrons at impact parameter between b and b + db[1]t

Considering a cylindrical geometry we can use Gauss's Law over an infinitely long cylinder centred on the particle trajectory and passing through the position of the electron.Then we get

$$\int E_\perp 2\pi b dx = 4\pi z e \qquad \text{or}$$
$$\int E_\perp dx = \frac{2ze}{b}$$

Using this, we get

$$I_\perp = \frac{2ze^2}{bv} \tag{1.18}$$

and energy gained by the electron as

$$\Delta E(b) = \frac{I_\perp^2}{2m} = \frac{2z^2e^4}{mb^2v^2} \tag{1.19}$$

This is for one electron. Considering a material with electron density n, then the energy lost to all the electron located at a distance between b and $b + db$(look at figure 1.3) in a thickness dx will be

$$-dE(b) = \Delta E(b) n.dV = \frac{4\pi z^2 e^4}{mv^2}.n.\frac{db}{b}.dx \tag{1.20}$$

or

$$-\frac{dE(b)}{dx} = \Delta E(b) n.dV = \frac{4\pi z^2 e^4}{mv^2}.n.\frac{db}{b} \tag{1.21}$$

Integrating this with the safe bound of b_{max} and b_{min} so as to not blow up the function we get the energy deposited per dx length as

$$-\frac{dE(b)}{dx} = \frac{4\pi z^2 e^4 n}{mv^2}.ln\Big[\frac{b_{max}}{b_{min}}\Big] \tag{1.22}$$

The upper limit b_{max}can be estimated by considering that the collision time τ cannot exceed the typical time period associated with bound electrons, namely $\tau \simeq \frac{1}{\bar{\nu}}$ where $\bar{\nu}$ is the characteristic mean frequency of the excitation of electrons. If the collision time were much larger than the typical revolution period, the passage of the particle could be considered as similar to an adiabatic process which does not affect the electron energy. At relativistic energies the region of space at the maximum

electric field strength is contracted by the Lorentz factor γ. and consequently the collision time becomes $\simeq \frac{b_{max}}{\gamma v}$. This implies that

$$\tau \simeq \frac{1}{\bar{\nu}} \simeq \Big(\frac{b_{max}}{\gamma}\Big)\frac{1}{v} \tag{1.23}$$

and

$$b_{max} \simeq \frac{v\gamma}{\bar{\nu}} \tag{1.24}$$

Defining the mean excitation potential as $I = h\bar{\nu}$ we get b_{max} as

$$b_{max} \simeq \frac{v\gamma h}{I} \tag{1.25}$$

The lower limit b_{min} however, is evaluated considering the extent to which the classical treatment can be employed. In the framework of the classical approach the wave characteristics of particles are neglected. This assumption is valid as long as the impact parameter is larger (e.g., double) than the de Broglie wavelength of the electron in the center of mass system(cms) of the interaction. Thus $2b_{min} \simeq \frac{h}{P_{ecm}}$, where P_{ecm} us the electron momentum in cms. Because the electron mass is much smaller than the mass of the incoming heavy particle, the cms is approximately associated with the incoming particle and conversely the electron velocity in the cms is opposite and almost equal in absolute value to that of the incoming particle, v. We then have that $|P_{ecm}| \simeq m\gamma v = m\gamma\beta c$ and

$$b_{min} \simeq \frac{h}{2m\gamma\beta c} \tag{1.26}$$

Substituting the values of b_{min} and b_{max} in equation 1.22 we obtain

$$-\frac{dE(b)}{dx} = \frac{4\pi z^2 e^4 n}{mv^2}.ln\Big[\Big(\frac{v\gamma h}{I}\Big)\Big(\frac{2m\gamma\beta c}{h}\Big)\Big] = \frac{2\pi z^2 e^4 n}{mv^2}.ln\Big(\frac{2m\gamma^2 v^2}{I}\Big)^2 \tag{1.27}$$

Finally using the value of the maximum energy transfer we derived in equation 1.15 we can write equation 1.27 as

$$-\frac{dE}{dx} = \frac{2\pi n z^2 e^4}{mv^2}\left\{ln\left[\frac{2mv^2 W_m}{I^2(1-\beta^2)}\right]\right\} \tag{1.28}$$

This equation is equivalent to the energy-loss formula in equation 1.1 except for the -$2\beta^2$,$-\delta$ due to the density effect and -U which is the shell correction. The -$2\beta^2$ is

derived in the quantum treatment of the energy loss by collisions of a heavy, spin 0 incident particle. It has been noticed that spin plays an important role when the transferred energy is almost equal to the incoming energy(this occurs with very limited statistical probability).

By introducing the classical electron radius, $r_e = \frac{e^2}{mc^2}$ we can evaluate the numerical coefficient in Eq 1.1 using Eqn 1.2

$$\frac{2\pi n z^2 e^4}{mv^2} = 2\pi N mc^2 r_e^2 \Big(z^2 \rho \frac{Z}{A} \frac{1}{\beta^2} \Big) \tag{1.29}$$

$$= 0.1535 \frac{\rho z^2 Z}{A\beta^2} [MeV/cm] \tag{1.30}$$

then the equation becomes

$$-\frac{dE}{dx} = 0.1535 \frac{\rho z^2 Z}{A\beta^2} \left\{ ln \left[\frac{2mv^2 W_m}{I^2(1-\beta^2)} \right] - 2\beta^2 - \delta - U \right\} [MeV/cm] \tag{1.31}$$

or the working equation that we will use (with W_m given by equation 1.15) and the shell correction $U = \frac{2C}{Z}$ is

$$-\frac{dE}{dx} = 0.307 \frac{\rho z^2 Z}{A\beta^2} \left\{ ln \Big[\frac{2m\beta^2 c^2}{I(1-\beta^2)} \Big] - \beta^2 - \delta/2 - \frac{C}{Z} \right\} [MeV/cm] \tag{1.32}$$

Note we calculate the constant value of 0.307 in the unit such that ρ is in g/cm^3

1.1.3 The Mean Excitation Potential

The mean excitation potential is the main parameter of the energy loss formula, and is essentially the average orbital frequency $\bar{\nu}$ times the Planck's constant, $h\bar{\nu}$. It is theoretically a logarithmic average of ν weighted by the so called oscillator strengths of the atomic levels. In practice, this is a very difficult quantity to calculate since the oscillator strengths are unknown for most materials. Instead, values of I for several materials have been deduced from actual measurements of dE/dx and semi-empirical formula for I vs Z fitted to the points. For our data consumption we shall take the values from PDG-93-06 appendix 2. Almost all the values of mean ionisation potential for different materials are readily available there.

1.1.4 Density Correction

The density effect arises from the fact that the electric field of the particle also tends to polarize the atoms along its path. Because of this polarization, electrons far from the path of the particle will be shielded from the full electric field intensity. Collisions with these outer lying electrons will therefore contribute less to the total energy loss than predicted by the energy loss formula. This effect becomes more important as the particle energy increases, as b_{max} increases with the incident energy as can be seen from equation 1.25. This implies that the distant collision contributes more and more when the energy increases but in fact due to polarization shielding the far away electron will contribute less hence the density correction becomes prominent at higher energies. It is clear that this effect depends on the density of the material(hence the term "density" effect), since the induced polarisation will be greater in condensed materials than in lighter substances such as gases. At very high energies,

$$\delta/2 \rightarrow ln(\hbar\omega_p/I) + ln(\beta\gamma) - 1/2 \tag{1.33}$$

where $\delta/2$ is the correction introduced and $\hbar\omega_p$ is the plasma energy given by

$$\hbar\omega_p = \sqrt{4\pi n r_e^3 . mc^2/\alpha} = 28.816\sqrt{\rho\left\langle\frac{Z}{A}\right\rangle}eV \tag{1.34}$$

At some low energy the density effect is insignificant, and at some high energy it is sufficiently described by the asymptotic form given in 1.33. Sternheimer has proposed the following parametrization.

$$\delta = \begin{cases} 2(ln10)x - \bar{C} & \text{if } x \geq x_1 \\ 2(ln10)x - \bar{C} + a(x_1 - x)^k & \text{if } x_0 \leq x < x_1 \\ 0 & \text{if } x < x_0 (\text{nonconductors}) \\ \delta_0 10^{2(x-x_0)} & \text{if } x < x_0 (\text{conductors}) \end{cases} \tag{1.35}$$

where $x = log_{10}(\beta\gamma)$ and the other parameters are depend on the absorbing material the values of which will be taken from PDG-93-06 appendix 2 for our purpose.

1.1.5 Shell Correction

The shell correction accounts for effects which arise when the velocity of the incident particle is comparable or smaller than the orbital velocity of the bound electrons.

At such energies , the assumption that the electron is stationary with respect to the incident particle is no longer valid and the formula breaks down. The empirical formula taken from the PDG-93-06 is as follows.

$$C = (0.422377\eta^{-2} + 0.0304043\eta^{-4} - 0.00038106\eta^{-6}) \times 10^{-6} I^2 \quad (1.36)$$

$$+ (3.858019\eta^{-2} - 0.1667989\eta^{-4} + 0.00157955\eta^{-6}) \times 10^{-9} I^3 \quad (1.37)$$

where $\eta = \beta\gamma$ and this form is valid only for $\eta > 0.13$

1.1.6 dE/dx for Mixtures and Compound

The dE/dx formula which we have given so far applies to pure elements. A good approximate value can be found in most cases by averaging dE/dx over each element in the compound weighted by the fraction of electrons belonging to each element(Bragg's Rule). Then

$$\frac{1}{\rho}\frac{dE}{dx} = \frac{w_1}{\rho_1}\Big(\frac{dE}{dx}\Big)_1 + \frac{w_2}{\rho_2}\Big(\frac{dE}{dx}\Big)_2 + ... \quad (1.38)$$

where w_1, w_2 etc are the fractions by weight of elements 1,2,... in the compound. More explicitly, if a_i us the number of atoms of the ith element in the molecule M, then

$$w_i = \frac{a_i A_i}{A_m} \quad (1.39)$$

where A_i is the atomic weight of ith element, $A_m = \Sigma a_i A_i$

1.2 Calculations for Energy Loss

We shall calculate the energy deposited by a muon, proton on Cu, Germanium and Argon + Carbon Dioxide Mixture(with different concentrations) and we shall study how the energy loss varies.
We know Kinetic Energy to be

$$K.E = (\gamma - 1)m_0c^2 \quad (1.40)$$

or

$$\gamma = \frac{K.E}{m_0c^2} + 1 \quad (1.41)$$

or

$$\beta = \frac{\sqrt{\gamma^2 - 1}}{\gamma} = \frac{\sqrt{(\frac{K.E}{m_0 c^2} + 1)^2 - 1}}{\frac{K.E}{m_0 c^2} + 1} \tag{1.42}$$

And plugging in the value of β in Eqn 1.32 we can calculate the energy lost in the medium. Note that we have restricted the shell correction formula given in Eqn 1.36 to energies for which $\eta > 0.13$. C is set to zero for $\eta < 0.13$. Calculating the density correction factors was done by using the Sternheimer parameters given by Eqn 1.35. We have all the parameter from the appendix of PDG-93-06.

1.2.1 Calculating the energy deposition in Argon Carbon-Dioxide mixture.

For this we first calculate the energy deposited in Carbon Dioxide. We take the data from the appendix of PDG-93-06 for carbon and O_2. From there we calculate the energy deposited in each medium independently. Now using Eqn 1.38 we calculate the the total energy deposited in Carbon Dioxide medium using the following equation.

$$\frac{dE}{dx} = \rho_{CO_2}.\left(\frac{w_C}{\rho_C}\left(\frac{dE}{dx}\right)_C + \frac{w_{O_2}}{\rho_{O_2}}\left(\frac{dE}{dx}\right)_{CO_2}\right) \tag{1.43}$$

Which becomes

$$\frac{dE}{dx} = \rho_{CO_2}.\left(\frac{M_C}{M_{CO_2}.\rho_C}\left(\frac{dE}{dx}\right)_C + \frac{M_{O_2}}{M_{CO_2}.\rho_{O_2}}\left(\frac{dE}{dx}\right)_{CO_2}\right) \tag{1.44}$$

The values were taken from PDG-93-06. Similarly doing this for the Ar+CO_2 mixture (100-x):x we get

$$\frac{dE}{dx} = \rho_{Ar+CO_2}.\left(\frac{\rho_{Ar}(100-x)}{100\rho_{Ar+CO_2}.\rho_{Ar}}\left(\frac{dE}{dx}\right)_{Ar} + \frac{\rho_{CO_2}.x}{100.\rho_{Ar+CO_2}.\rho_{CO_2}}\left(\frac{dE}{dx}\right)_{CO_2}\right) \tag{1.45}$$

Giving

$$\frac{dE}{dx} = (1 - \frac{x}{100})\left(\frac{dE}{dx}\right)_{Ar} + \frac{x}{100}.\left(\frac{dE}{dx}\right)_{CO_2} \tag{1.46}$$

In our laboratory we have a combination of 70:30 Ar:CO_2 mixture, so x is set to 30 for the graphs.

1.2.2 Theoretical Curves and Discussion

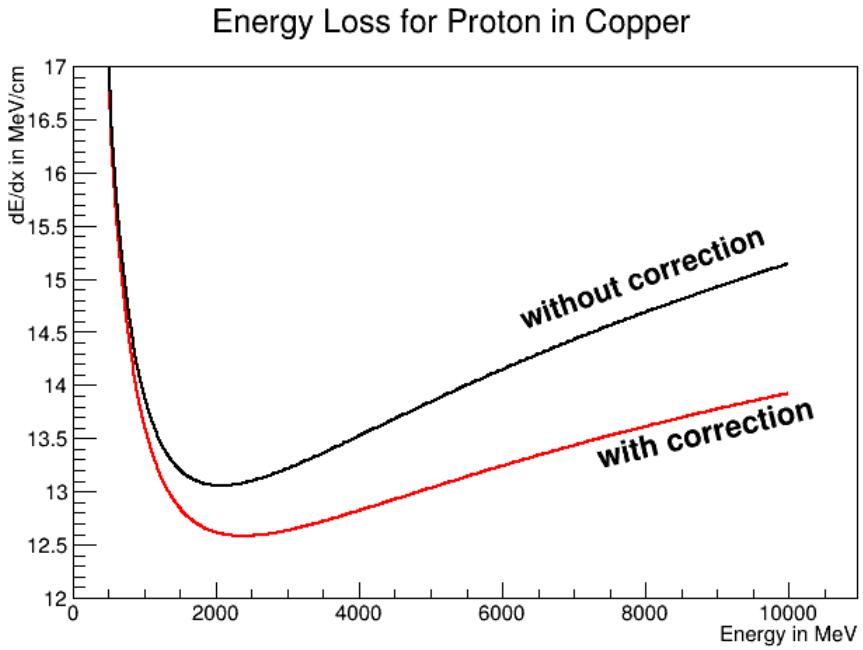

Figure 1.4: Energy Loss formula with and without shell and density corrections for proton incidented on Copper

Figure 1.4 shows how the Energy Loss formula commonly called Bethe-Bloch formula varies with and without the shell and density correction terms. Both the curves match at lower energies, and at higher energies they differ mainly due to the density correction factor. One thing to note is that the shell correction factor was set to zero for $\beta\gamma < 0.13$ which, for proton, is less than the 7.76 MeV of Kinetic Energy. This was done because the equation 1.36 doesn't hold below this limit. Figure 1.5 shows the plots of Bethe Bloch energy loss formula for different incident particle on Copper. Note that these all are average energy depositions per unit length of the material. At non-relativistic energies, dE/dx is dominated by the overall $\frac{1}{\beta^2}$ factor and decreases with increasing velocity until about $v \simeq 0.96c$, where a minimum is reached. Particles at this point are known as minimum ionizing. Beyond this point $\frac{1}{\beta^2}$ almost becomes constant and the logarithmic rise takes over. This relativistic rise however, is cancelled due to the density correction.Look at the muon-proton curve in

figure 1.6 for a better visualisation.
For Energies below the minimum ionizing value, each particle exhibits a dE/dx curve which , in most cases, is distinct from the other particle types. This characteristics is often exploited in particle physics as a means of identifying the particle in this energy range.

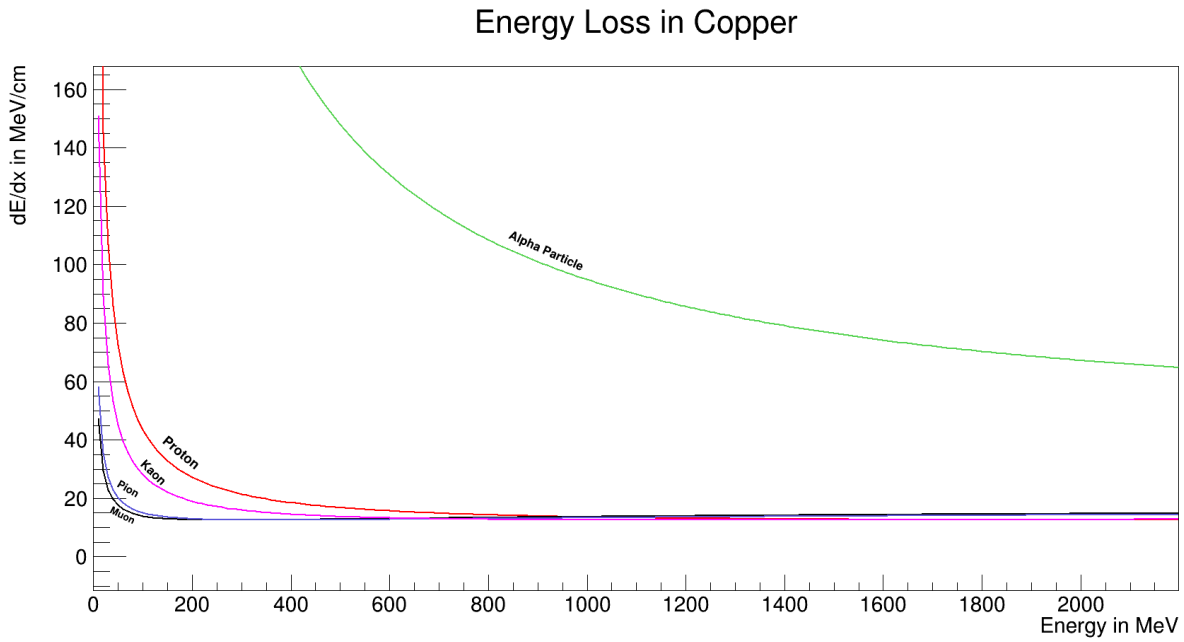

Figure 1.5: Energy Loss formula for different particles in Copper

In figure 1.5 all particles except for Alpha particle have charge number (z) as 1. The curves vary because of the different masses of the particles. As the mass increases, the β values decreases for a given kinetic energy there by increasing the energy deposition(shifting the graph towards the right side). For Alpha particle, the energy deposition is much greater compared to the other particles shown because it has double the charge and is very massive($\simeq$3.97 times massive compared to proton).Looking at Eqn 1.32 we can see that energy loss has a z^2 dependence.

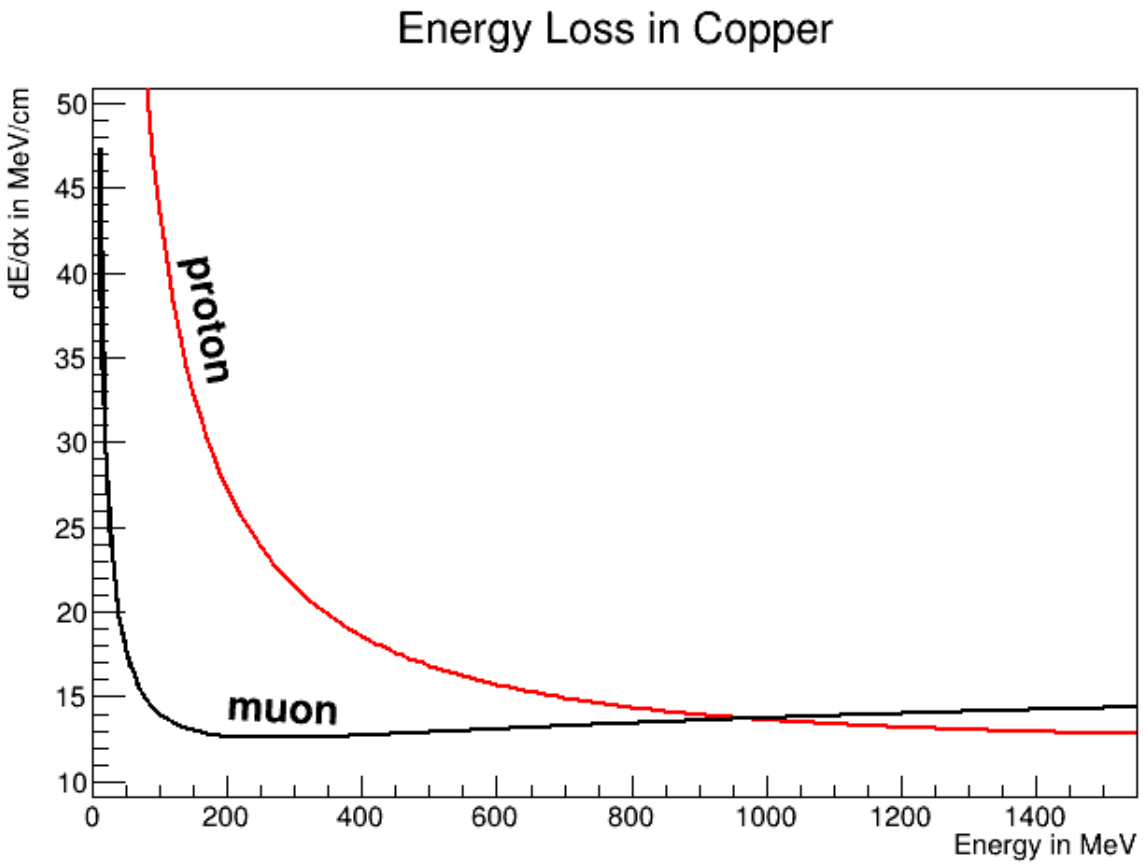

Figure 1.6: Energy Loss formula for different particles in Copper

In figure 1.5 all particles except for Alpha particle have charge number (z) as 1. The curves vary because of the different masses of the particles. As the mass increases, the β values decreases for a given kinetic energy there by increasing the energy deposition(shifting the graph towards the right side). For Alpha particle, the energy deposition is much greater compared to the other particles shown because it has double the charge and is very massive($\simeq$3.97 times massive compared to proton).Looking at Eqn 1.32 we can see that energy loss has a z^2 dependence.

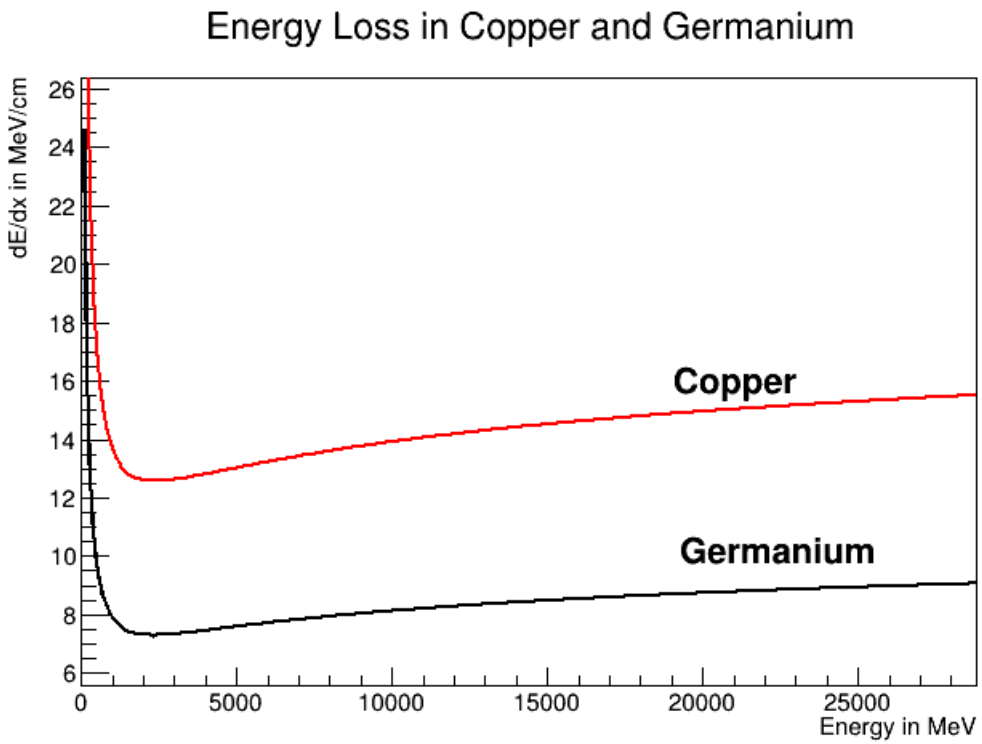

Figure 1.7: Energy Loss proton incidented on Ge and Cu

Now, if the incident medium is changed, the energy deposition will change too. This can be seen by looking at figure 1.7. We can infer that the energy is deposited more in the copper than in the Germanium material. Although the Ge has more atomic number(Z), the density of Cu is more and the mass number(which is inversely related to energy loss) of Cu is less, making the particle suffer more energy loss in Copper than in Germanium. One point to note from this graph is that the minimum ionization energy is dependant on the incident particle and not on the medium.

The mixture of Carbon Dioxide and Argon with 30:70 volume by volume mixture was calculated and plotted for muon and proton. The following are the plots:(figure 1.8 and 1.9).

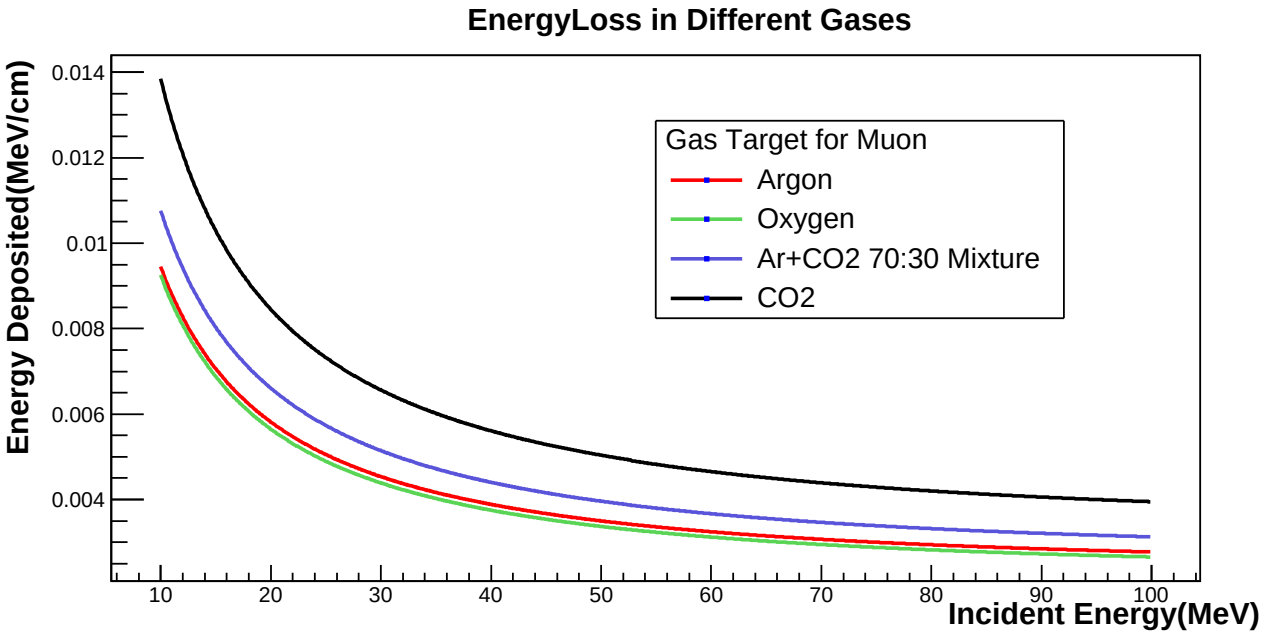

Figure 1.8: Energy Loss muon incidented on different gasses and mixtures

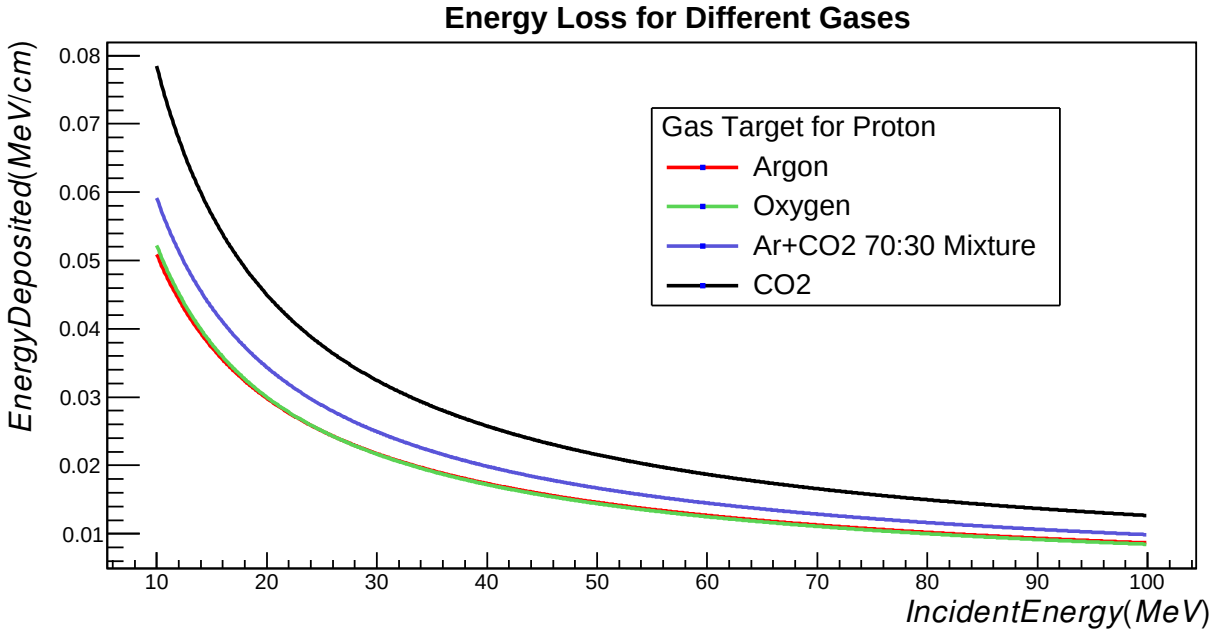

Figure 1.9: Energy Loss proton incidented on different gasses and mixtures

You can infer similar things from these graphs too as discussed earlier. As the

density increases, Energy loss increases. Carbon Dioxide is the densest gas in the plot with a density of 1.98 Kg/m^3. Argon and Oxygen has density at 1.66 Kg/m^3 and 1.33 Kg/m^3 respectively. This gives a $\frac{\rho Z}{A}$ value for carbon dioxide($\simeq$0.99)much higher than that of O_2($\simeq$0.66) and of Argon($\simeq$ 0.75). This explains the difference shown in the graph for energy deposition in CO_2 and Ar and Carbon.

1.3 Limitations of Bethe-Bloch Formula Energy Loss Formula

The energy loss formula, with the shell and density effect corrections as given in equation 1.32 is the usual expression employed in most energy loss calculations. For elementary particles and nuclei upto the α particle, this formula gives accurate results to within a few percent for velocity ranging from relativistic region down to $\beta \simeq 0.1$. For $\beta \leq 0.05$, many of the assumptions inherent in the Bethe-Bloch formula are no longer valid even with the corrections. For heavier nuclei this is even more the case because of the electron capture effects.

Chapter 2

Development and Testing of Bakelite Resistive Plate Chamber(RPC)

RPCs are fast, planar, rugged and low-cost gas detectors which are being used extensively in a number of high energy and astro-particle physics experiments. They find applications for charged particle detection, time of flight, tracking and digital calorimetry due to their large signal amplitudes as well as excellent position and time resolutions. It was first introduced in 1981 by R.Santonico and R. Cardarelli as an alternative to discharge spark counters. The problem with the spark counter was that the discharge energy was sufficiently large enough to damage the surface of the counter electrodes and it had quite a long dead time due to the fact that it used switching-off circuit to prevent the electrodes from being short-circuited by the spark produced in the gas. The RPCs were free from discharge damages due to the high bulk resistivity and provided a time resolution of the order of 1ns. Along with this the materials required for RPC were cheap like glass, bakelite or plastic and required lower mechanical precision in fabrication. [7]

2.1 Working

An RPC is a particle detector utilising a constant and uniform electric field produced by two parallel electrode plates, atleast one of which is made of a material with high bulk resistivity.[7] A gas mixture with a high absorption coefficient for ultraviolet light is flown through the gap between the electrodes. When the gas is ionised by

a charged particle crossing the chamber, free charge carriers that are deposited in the gas gap trigger avalanches of electrons in the externally applied electric field and originate a discharge. Due to the high resistivity of the electrodes, the electric field is suddenly dropped down in a limited area(locally) around the point where the discharge occurred. Thus the discharge is prevented from propagating through the whole gas volume. The sensitivity of the counter remains unaffected outside this small area.[7] On the other hand, due to the ultra-violet absorbing component of the gas mixture, the photons produced by the discharge are not allowed to propagate in the gas. This prevents secondary discharges from originating at other points of the detector.The potential drop is then picked up by a conductive strip which is placed outside the electrodes due to electrostatic induction. The schematic of a basic RPC is given in Figure 2.1.

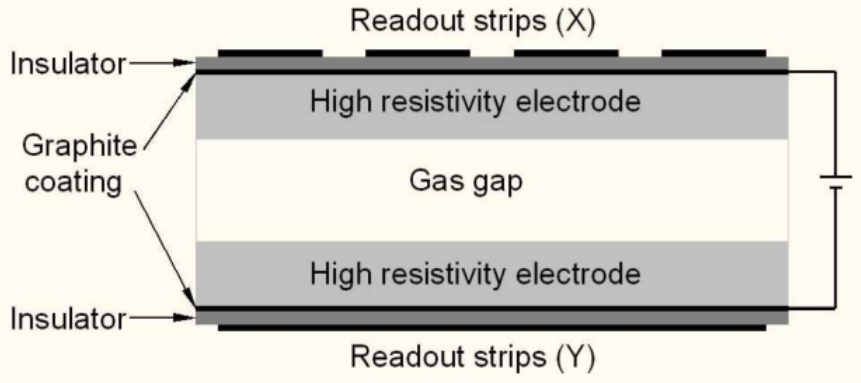

Figure 2.1: Schematics of a Resistive Plate Chamber [7]

2.2 Fabrication

Here we will outline the process through which the 15x15 cm^2 was fabricated at NISER. First is to cut bakelite panel of 2mm thickness into two squares of 225cm^2 area each. The edges are smoothed out with sandpaper. Afterwards we make spacers by cutting 2 mm panel of polycarbonate with width of 1cm and height of 14 cm and 11 cm, two of each so as to accommodate the 3cm gas nozzle with 1mm hole diameter with 2mm thickness. We require a single button spacer which will be spaced at the

center so as to support the gap at the center of the contraption. The thickness of this is also 2mm and diameter is 1cm. After cleaning everything with propanol we start to place together the RPC gap. Araldite standard epoxy adhesive was used to seal and fix the gap. The resin and the hardener were taken in 1:1 ratio on a crucible and mixed thoroughly. One of the bakelite plates was placed on a sheet of oil-paper and the side spacers were glued in towards the edge in such a way that there were no protrusions and was contained in the 15x15cm^2 geometry of the bakelite plate leaving aside the space for the gas nozzle. Button spacer was placed exactly in the middle and glued down.Note that we marked the center of the bakelite plate with a pencil before hand and the minimum amount of glue was used. Excess glue was removed using proponol. And caution should be maintained to make sure no dust particle or glue goes on to the surface of the bakelite plate other than the area covered by the spacers, otherwise these places will create dead regions. Now the gas nozzle was glued down diagonally opposite each other in the same manner as the edge spacers. Note that we didn't apply any silicon oil to make the surface smooth.

While gluing down the gas nozzle, one must make sure the araldite does not block the gas hole. For this purpose we had inserted a twisted copper wire to the thin hole on both the gas nozzle. After applying a thin paste of araldite on the spacers and the gas nozzle we placed the top bakelite panel carefully and waited for the araldite to cure. It is useful to put some heavy object, not too heavy, on the RPC while the araldite sets in. The photo of the RPC after applying the araldite is shown in figure 2.2.

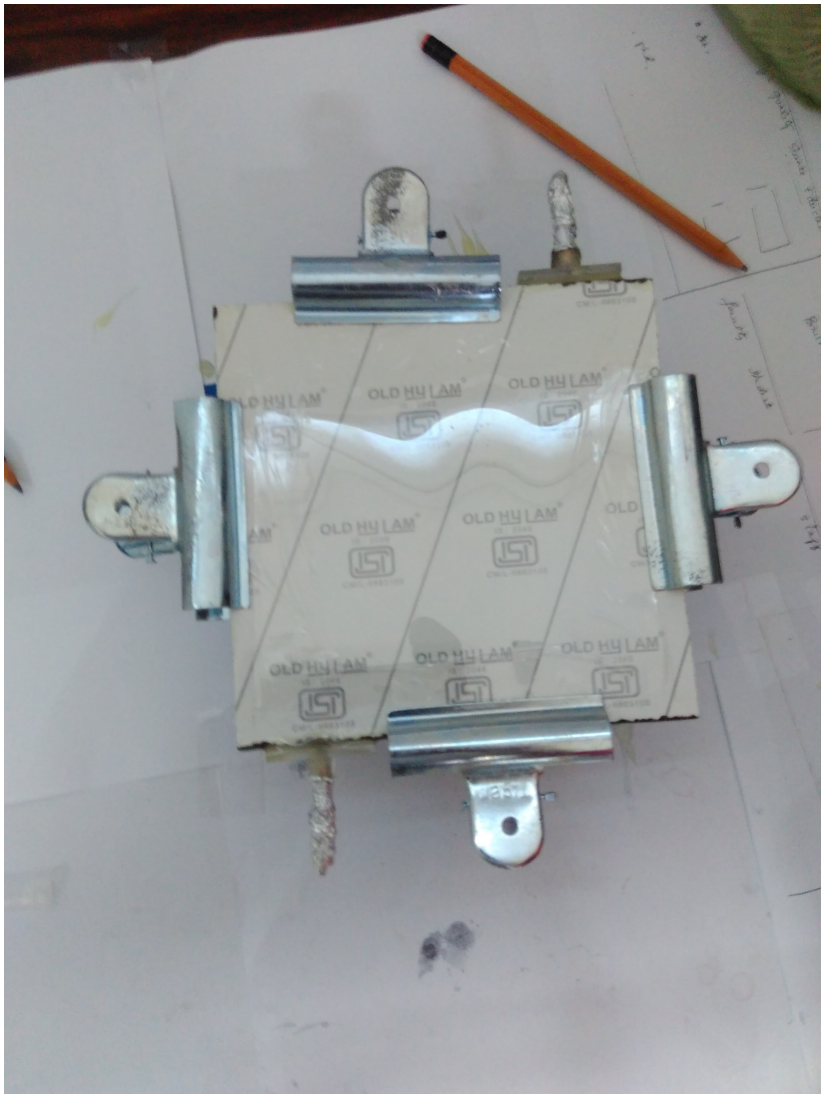

Figure 2.2: RPC after applying the araldite

After more than 12hrs we inspected the RPC to find that the copper-wire had got stuck inside the gas nozzle. For rectifying this we had to cut the gas nozzle off. We did this in TIFR INO Lab where we used DP-190 epoxy adhesive to glue back the cut gas nozzle.

2.2.1 Leak Test

The first test is to check for gas leak in RPC gap. This was done using a U-tube Manometer filled with water. One end of the manometer was connected to the RPC

gas nozzle. The other gas nozzle of the RPC was connected to a gas cylinder and the pressure was slowly turned on. The water level on the U-Tube manometer began to shift by 30mm. Then we closed the gas valve and observed whether the water level shifts back. It did, implying that there were leaks and the leaks were found using a gas sniffer. After resealing the places which leaked (mainly it was the gas nozzle area) using DP-190 epoxy adhesive, the unit was tested again and no leaks were found. Figure 2.3 shows the U-Tube manometer being checked for shift in water levels.

Figure 2.3: U-Tube manometer being checked for shift in water level.

2.2.2 Graphite paint

The bakelite was painted with graphite paint. This paint was specially manufactured as per the requirements of the Indian Neutrino Project RPCs by Nerolac kansai India. The paint was mixed with thinner in 1:10 ratio. After masking the edges of

the RPC using a masking tape(1cm away from the edges), we painted the RPC using a spray gun and care was taken so as to create a uniform layer of paint. After the paint dried(within minutes) the masking tape was removed. Then the average surface resistivity of the graphite coating was determined to be around 679 k$\Omega/\square$(5cmx5cm) of the instrument used.

2.2.3 Flushing of the Gas

Gas system connections were made to flow gas through the RPC. The gas mixture used was 95.2% Freon(R134A) 4.5% Isobutane and 0.3% SF_6. This RPC is going to be studied in avalanche mode. Other gases that were inside the RPC during fabrication were flushed out by flowing the gas mixture for more than four hours. The gas flow is kept on for the rest of the fabrication processes as it doesn't hinder it, and it is prepared for biasing.

2.2.4 Preparations for Biasing

Copper tape was used to provide the surface for applying the high voltage. After soldering the copper strip with High Voltage capable coaxial cable(with one end attached to the SHV connector) we stuck the copper tape on to the graphite surface of the RPC. This was done for either side. Kapton tape was used to secure the copper tape. Now 4 Mylar sheets were cut in the dimensions of the RPC. We placed two on each side of the RPC and secured it with Kapton tape. Figure 2.4 shows the RPC after attaching the transparent sheet and the SHV connectors.

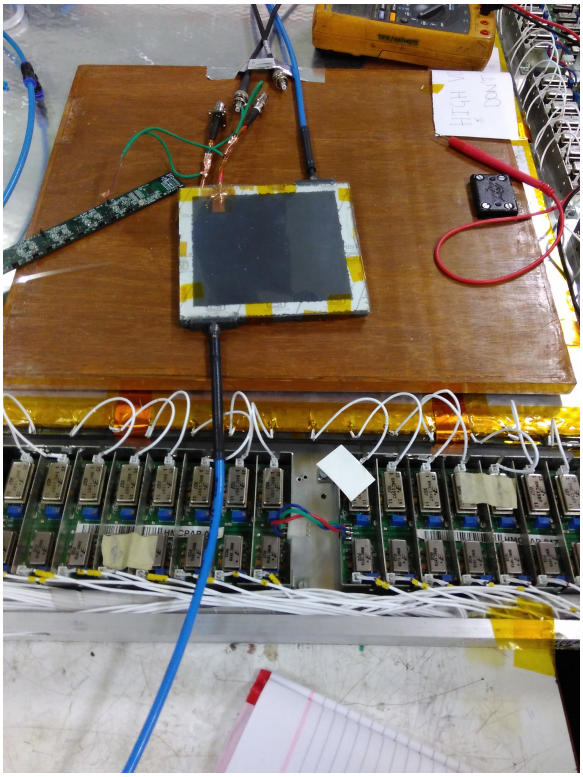

Figure 2.4: RPC after attaching the HV cable and Insulator.

2.2.5 Setting Up Pick-Up Panel

The pre-built pick-up panels made of honey-comb structure were used with one-side copper strips of 2.8cm width placed with 2mm gap and other side aluminium foil(completely covered). Two of such panels cut to the dimensions of the RPC were used. Each copper strip was connected to the Aluminium foil through a 39 Ωs resistor with a tolerance of 5%. And to each copper strip, we attach coaxial cables to readout the signal which will be fed to the pre-amplifier, the grounds of which are connected to the aluminium side. Now, both the pick-up panels are placed on either side of the RPC, copper strips facing down, and secured into place by kapton tape. The aluminium side of the pick-up panels are grounded. Figure 2.5 shows the copper strips of the pick-up panel.

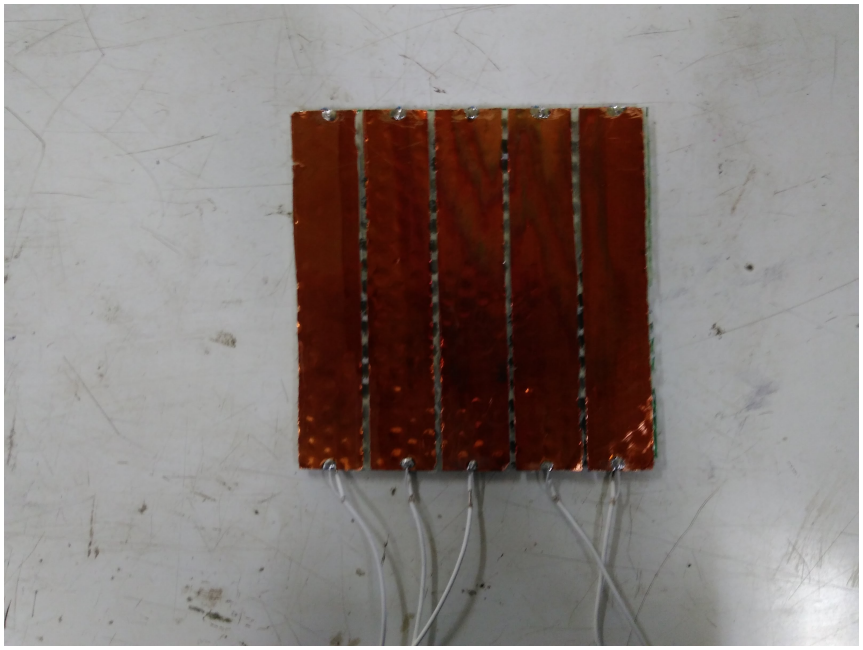

Figure 2.5: Copper strips of the pick-up panel after coaxial cables and resistors

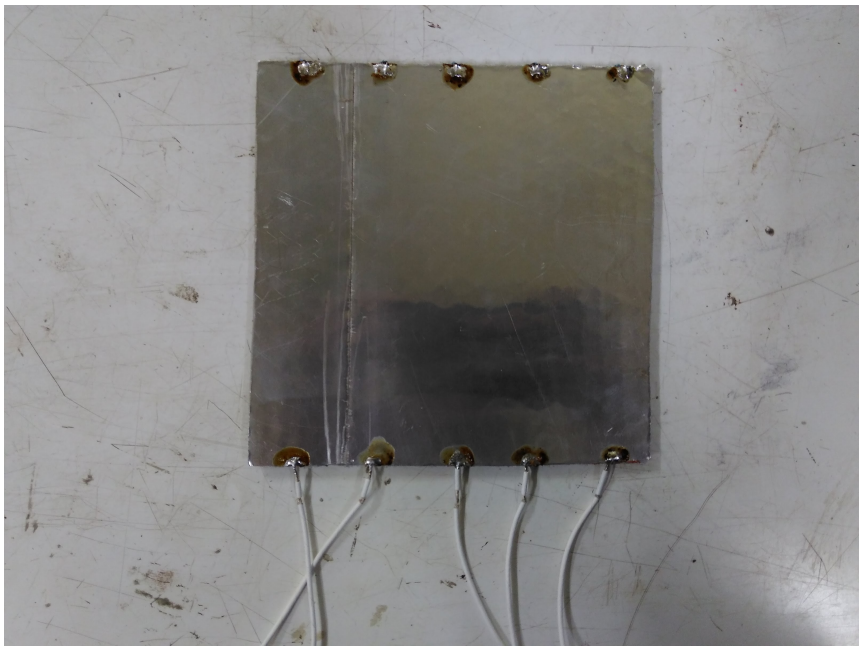

Figure 2.6: Aluminium side of the pick-up panel after connections

Figure 2.7: Copper strips grounded through resistors of 39 Ω

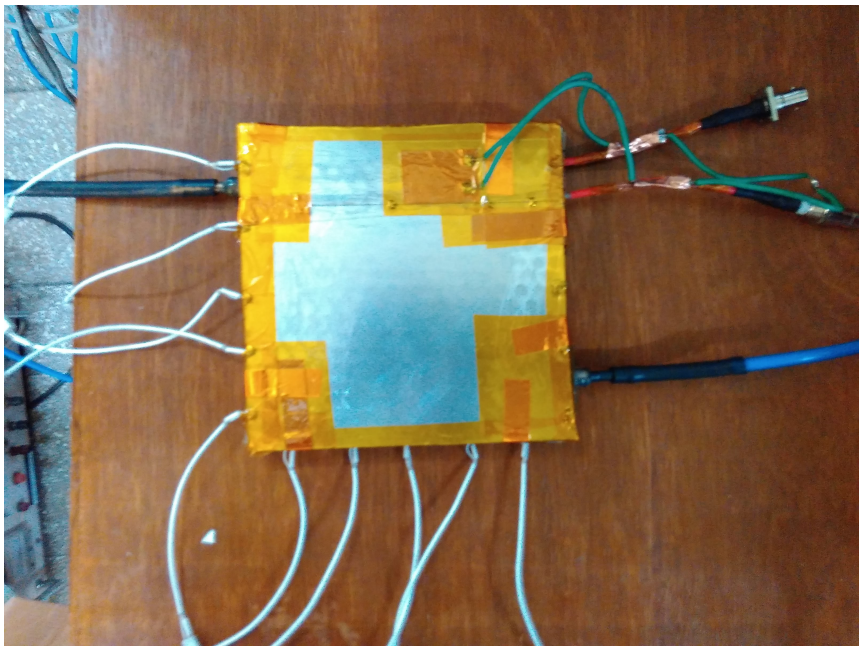

Figure 2.8: RPC after securing the read-out strips with kapton tape.

2.3 Testing the RPC

2.3.1 Biasing

Now we connected the RPC to the HV supply and started ramping up the voltage. And we varied the voltage in steps of 200V till 0-2500V on the top and bottom panel and 100V from 2500-5000V. So total of 10kV of biasing was applied. In between each steps an average time of 30 minutes was given for the current to settle down. It was kept at 10kV overnight and the leakage current test was done the day after when the current fluctuations stabilized. The leakage current was displayed by the High Voltage Supply itself. Figure 2.9 shows the leak current to the voltage graph of the RPC under biasing. After this we moved on to connect the RPC for testing the efficiency. The block diagram is given in figure 2.10 for the connections to the finger scintillators and RPCs connections.

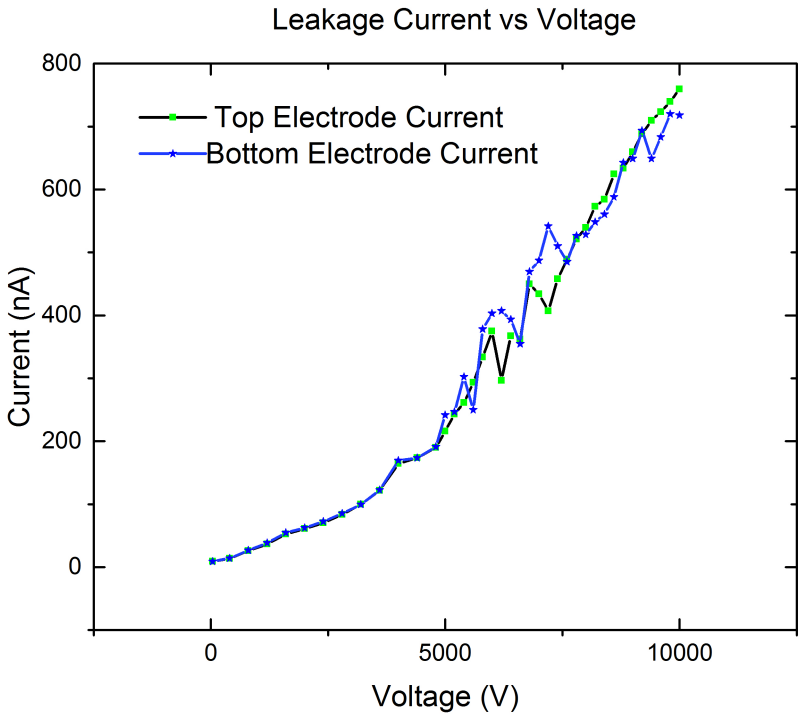

Figure 2.9: Leakage Current vs Voltage till 10kV biasing.

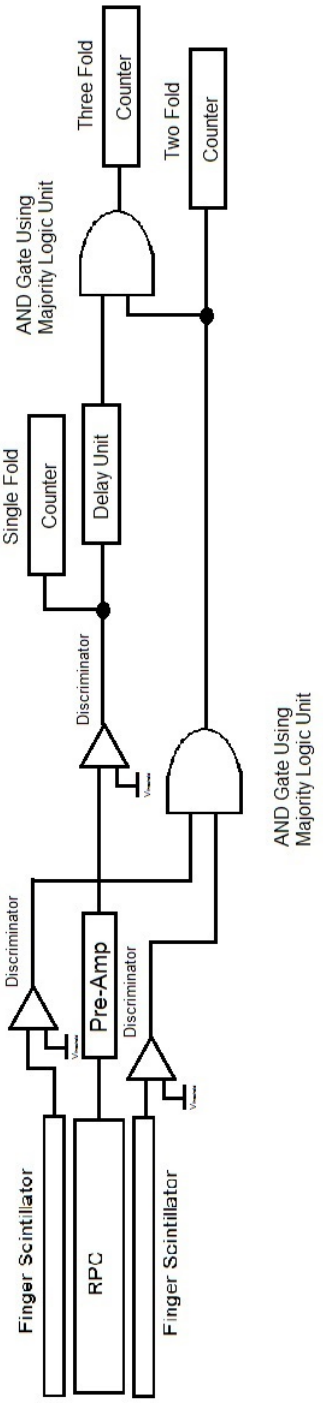

Figure 2.10: Schematic of the connections made.

2.3.2 Efficiency

The center pick-up strip of the top panel panel was connected according to figure 10 to take the efficiency test. Note that we biased positive high voltage to the top electrode. At first we connected the pre-amp(built by TIFR for testing Glass RPC) directly to the Digital Oscilloscope(LeCroy waveRunner 64Xi-A) to see the signal. And the two fold from the finger scintillators to D.O. Figure 2.11 shows the signal profile from the D.O. These signals are coming from the cosmic ray muons mostly. And the finger scintillators are kept on top and bottom of the middle pickup strip and aligned so both the finger scintillators cover the completed area of the copper strip. The photo is shown in figure 2.12. For delaying the signal we used coaxial cables as each meter of cable delayed the signal by 5ns.

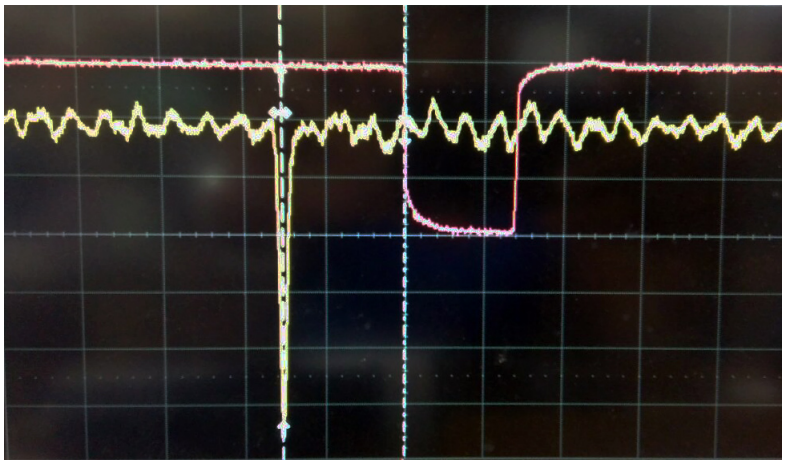

Figure 2.11: RPC signal profile from the Digital Oscilloscope with coincidence to finger scintillators.

The time scale is set to 50ns/div and for the voltage scale is set to 200mV/div for the RPC signal and 500mV/div. The time delay that occurred between the two pulses is 76.4 ns. The delay unit was used to correct for this in the three fold coincidence channel(look at figure 2.10). This signal was for 12.5kV of biasing. So we started our efficiency test from 12kV. The test was done over two day with irregular gaps in between measurement(which was unavoidable as I was running another experiment simultaneously). Figure 2.13 shows the efficiency of the RPC at different voltages.

The measurement counter was set to count for 30 mins for each measurement.

Figure 2.12: Photo of the Experimental setup.

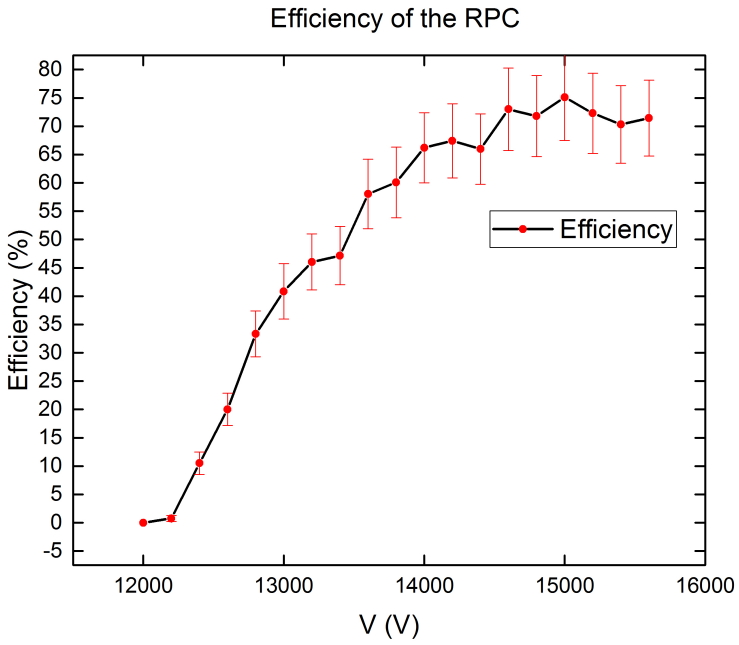

Figure 2.13: Efficiency of the RPC vs Voltage with statistical error bars

The Noise rate was calculated from the 1-Fold counter which was plotted against voltage and given in figure 2.14.

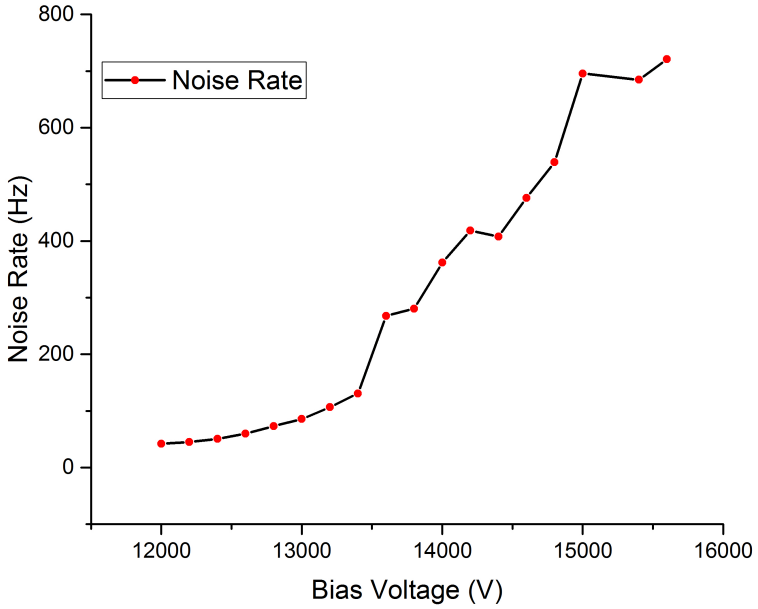

Figure 2.14: Noise rate of the RPC vs Bias Voltage

Chapter 3

Simulation using Geant4

Geant4 is a detector simulation toolkit written in C++ language which includes a complete range of functionality like tracking, geometry, physics models and hits. The physics processes that it uses include electromagnetic, hadronic and optical processes, and has a large set of long-lived particles, materials and elements, with a wide energy range starting from 250eV extending to 1 TeV range. It exposes the physics models utilised, to handle complex geometries, and to enable its easy adaptation for optimal use in different sets of applications.

3.1 Basics of Geant4

The main() method is implemented by two toolkit classes, G4RunManager and G4UImanager, and three classes, ExG4DetectorConstruction01, ExG4PhysicsList00 and ExG4ActionInitialization0 are derived from toolkit classes.[11]

3.1.1 G4RunManager

The first thing main() must do is create an instance of the G4RunManager class. This is the only manager class in the Geant4 kernel which should be explicitly constructed in the user's main(). It controls the flow of the program and manages the event loop(s) within a run. If the user wants to make the simulation code multi-threaded, G4MTRunManager should be instantiated instead of G4RunManager.
When G4RunManager is created, the other major manager classes are also created.

They are deleted automatically when G4RunManager is deleted. The run manager is also responsible for managing initialization procedures, including methods in the user initialization classes. Through these the run manager must be given all the information necessary to build and run the simulation, including

- how the detector should be constructed,
- all the particles and all the physics processes to be simulated
- how the primary particle(s) in an event should be produced, and
- any additional requirements of the simulation.

After initializing we create objects which specify detector geometry, physics processes and primary particle, respectively, and pass their pointers to the run manager using SetUserInitialization method[11]. The following is the code that does this.

```
runManager->SetUserInitialization(new ExG4DetectorConstruction01);
runManager->SetUserInitialization(new ExG4PhysicsList00);
runManager->SetUserInitialization(new ExG4ActionInitialization01);
```

ExG4DetectorConstruction01 is an example of a user initialization class which is derived from G4VUserDetectorConstruction. This is where the user describes the entire detector setup, including

- geometry
- material used in construction
- definition of sensitive region and
- readout schemes of the sensitive regions

Similarly ExG4PhysicsList01 is derived from G4VUserPhysicsList and requires the user to define

- the particles to be used in the simulation,

- all the physics processes to be simulated.

User can also override the default implementation for

- the range cuts for these particles

Also ExG4ActionInitialization01 is derived from G4VUserActionInitialization and requires the user to define

- user action class that are invoked during the simulation
- which includes one mandatory user action to define the primary particles.

The next instruction is to initialize which performs the detector construction, creates the physics processes, calculates cross-sections and otherwise sets up the run. The following code does this

```
runManager->Initialize();
```

The final runmanager method in main is

```
runManager->beamOn(numberOfEvent);
```

and it begins the run of sequentially processed events. "numberOfEvents" variable passes the number of times the event will be run.The beamOn() method may be invoked any number of times within main() with each invocation representing a separate run. Once a run has begun neither the detector setup nor the physics processes may be changed. They may be changed between runs.
Other manager classes are created when the run manager is created. One of these is the user interface manager, G4UImanager. We obtain a pointer to the interface manager in order for the user to issue commands to the programme. It may be done by the following code:

```
G4UImanager* UI = G4UImanager::getUIpointer();
```

And one can use applyCommand() method to apply command ,which are available, to the programme.

3.1.2 User Initialization and Action Classes

There are two kinds of user classes, user initialization classes and user action classes. User initialization classes are used during the initialization phase, while user action classes are used during the run. User initialization classes should be directly set to G4RunManager through SetUserInitialization() method, while user action classes should de defined in G4VUserActionInitialization class.[11] All three user initialization classes are mandatory. They must be derived from the abstract base classes provided by Geant4:

- G4VUserDetectorConstruction
- G4VUserPhysicsList
- G4VUserActionInitialization

G4RunManager checks for the existence of these mandatory classes when the Initialize() and BeamOn() methods are invoked.

```
#include "ExG4ActionInitialization01.hh"
#include "ExG4PrimaryGeneratorAction01.hh"
void ExG4ActionInitialization01::Build() const
{
SetUserAction(new ExG4PrimaryGeneratorAction01);
}
```

G4VUserPrimaryGeneratorAction is a mandatory class the user has to provide. It creates an instance of a primary particle generator. ExG4PrimaryGeneratorAction01 is an example of a user action class which is derived from G4VUserPrimaryGeneratorAction. In this class the user must describe the initial state of the primary event.

Geant4 provides additional five user hook classes:

- G4UserRunAction
- G4UserEventAction

- G4UserStackingAction
- G4UserTrackingAction
- G4UserSteppingAction

These optional user action classes have several virtual methods which allow the specification of additional procedures at all levels of the simulation application. For our purpose we write out energy deposited to a text file from the EventAction such an additional procedure.

3.1.3 Defining Detector Geometry for RPC

We shall learn how to define detector geometries by making a geometry of the fabricated RPC 15x15cm^2 with variable thickness. The detector is made from a number of volumes. The largest volume is called the World volumes which encompasses, with some margin, all the other volumes in the detector geometries.

For the RPC detector I made the world volume to be a box with dimensions 2x2x2 m^3. This was done by creating an object from G4Box class called the worldBox. All this is done in the construct method of the User Initialiser for Detector Construction inherited from G4VUserDetectorConstruction class.This is done by the following code.

```
G4double world_x = 1.0*m;
  G4double world_y = 1.0*m;
  G4double world_z = 1.0*m;
G4Box* worldBox =  new G4Box("World", world_x,world_y,world_z);
```

Each volume is created by describing its shape and its physical characteristics, and then placing it inside a containing volume.

When a volume is placed inside another volume, we call the former the daughter volume and the latter the mother volume. The coordinate system of the mother volume is used for placing the daughter volume.

To describe a volume's full property, we use a logical volume. It includes the geometrical properties of the solid, and adds physical characteristics like the material of the volume, whether it contains any sensitive detector elements, the magnetic field etc...

So for our world volume we define a logical volume by creating an object of G4LogicalVolume class called worldLog. Before this we have to assign the material properties to the logical volume, which we do by creating an instance of G4NistManager class called nist, and using the method FindOrBuildMaterial() of the G4NistManager class and passing it the argument G4_AIR (which is to create an object of G4Material class with the properties of Air). The object name we pass it to object called Air. Now Air object that will have the physical properties of Air.

```
G4NistManager* nist = G4NistManager::Instance();
G4Material* Air = nist->FindOrBuildMaterial("G4_AIR");
```

And in the constructor we pass on the geometry volume, the material and the name respectively using the following code.

```
G4LogicalVolume* worldLog = new G4LogicalVolume(worldBox, Air,"World");
```

For placing it within the mother volume we use a physical volume and pass the logical volume we just created as an argument. So for our world volume we create a G4VPhysicalVolume object called "World" and we set the position(w.r.t the mother volume) and orientation using the G4PVPlacement method.We also pass it the logical volume. Here we have to specify which is the mother volume for the World Volume. Since this is the world volume we may leave this argument to be 0. The code for doing this is

```
G4VPhysicalVolume* World = new G4PVPlacement(0,G4ThreeVector(pos_x, pos_y,pos_z)
,worldLog,"RPC World",0,false,0);
```

The world volume has been successfully defined.Now for making the Bakelite Material. We make objects of G4Element class called elC,elH,elO. And in the constructors we pass the name, symbol, atomic number, and gram molecular mass of the elements respectively. This is for Carbon, Hydrogen, and Oxygen respectively.

The you make an object of the G4Material class called Bakelite and initialize it with the name, density and number of elements.This is done in the following code.

```
G4Element* elC = new G4Element(name = "Carbon",
symbol="C",z = 6., a=   12.0107*g/mole);
  G4Element* elH = new G4Element(name = "Hydrogen",
  symbol="H",z = 1., a= 1*g/mole);
  G4Element* elO = new G4Element(name = "Oxygen",
  symbol="O",z = 8., a= 16*g/mole);

  density=1.4*g/cm3;
  G4Material* Bakelite =  new G4Material(name = "Bakelite",
   density, ncomponents=3);
```

And we use the method called "AddElement" to add the elements to the objects with the number of atoms.The following is the code.

```
 Bakelite->AddElement(elC,natoms=1);
  Bakelite->AddElement(elH,natoms=4);
  Bakelite->AddElement(elO,natoms=2);
```

The molecular formula of bakelite used is CH_4O_2. Similarly we construct CO_2 object of the G4Material class also using the following code.

```
 density=1.977*kg/m3;

  G4Material* CO2 =  new G4Material(name = "CarbonDioxide",
  density, ncomponents=2);

  CO2->AddElement(elC,natoms=1);
  CO2->AddElement(elO,natoms=2);
```

Now from the G4NistManager object we take the Material Argon by using the argument G4_Ar in the method FindOrBuildMaterial.

```
G4Material* Ar = nist->FindOrBuildMaterial("G4_Ar");
```

Now the density of the Ar+CO_2 Mixture is calculated for different CO_2 percentages. And then we create an object "Gas" from the class G4Material passing the argument to the constructor the name,density and the number of components in the mixture. Then we use the AddMaterial method to add the material with the fractionmass of the components. Now you have the Gas object with the properties of Ar:CO2 with the ratio set by CO_2 percentages The following is the code.

```
co2_percent = 40;
 // percent of CO2 in the mixture.
 density = ((3994.8 + 4.062*co2_percent)/2240)*kg/m3; // calculating
  the density of the mixture of gases at stp.
 G4Material* Gas = new G4Material(name="ArCO2Mix",density,ncomponents=2);
 Gas->AddMaterial(CO2, fractionmass=co2_percent*perCent);
 Gas->AddMaterial(Ar, fractionmass=(100-co2_percent)*perCent);
```

You do this to create the three box shape volume(and its logical and physical volume)and sandwich the Gas volume between the top and bot bakelite plates. The following is the code

```
 thickness = 10;  // in mm
 G4Box* top_bake =  new G4Box("Top_bake", 7.5*cm,7.5*cm,1*mm);
 G4LogicalVolume* toplog = new G4LogicalVolume(top_bake, Bakelite,"Top_bake");
 G4VPhysicalVolume* topbake = new G4PVPlacement(0,G4ThreeVector(0*mm,0*mm,
 (thickness/2 + 1)*mm),toplog,"Top Electrode",worldLog,false,0);

 G4Box* cavity =  new G4Box("cavity",7.5*cm,7.5*cm,(thickness/2)*mm);
 G4LogicalVolume* cavitylog = new G4LogicalVolume(cavity, Gas,"cavity");
```

```
G4VPhysicalVolume* Cavity = new G4PVPlacement(0,G4ThreeVector(0*mm,0*mm,0*mm),
cavitylog,"Gap",worldLog,false,0);

G4Box* bot_bake =  new G4Box("Bot Bake", 7.5*cm,7.5*cm,1*mm);
G4LogicalVolume* botlog = new G4LogicalVolume(bot_bake , Bakelite,"Bot Bake");
G4VPhysicalVolume* botbake = new G4PVPlacement(0,G4ThreeVector(0*mm,0*mm,-
(thickness/2 + 1)*mm),botlog,"Bot Electrode",worldLog,false,0);

fScoringVolume = cavitylog;

return World;
```

Then the sensitive volume is set to the logical volume of the cavity(in the header file we set it to GetScoringVolume() object.) and the "World" object is returned for the method "construct".
And in the Event action class(B1EventAction) inherited from the action class G4UserEventAction, initially we set variable fEdep to be zero inside the method BeginOfEventAction which is called at the beginning of each event. Then this variable is updated and added to fEdep by the method we wrote as AddEdep(Method of B1EventAction) from the stepping action for each step. The energy deposited is calculated using the method GetTotalEnergyDeposit which is a method of G4Step(saves all the relevant information for each step) Class which will return the total energy deposited at each step. Here the Stepping Action class(B1SteppingAction) is inherited from G4UserSteppingAction. By changing the primary action generator class (B1PrimaryGeneratorAction)we can set the momentum and the particle spawn position which will be discussed later.This is how we determine the energy deposited at each event. These are the basics of Geant4 programming we used to get the simulation running.

3.1.4 Physics Processes

All physics processes are derived from the G4VProcess base class. Depending on its nature, a physics process possesses one or more characteristics represented by the following actions handled by the tracking class category.[12]

(1) at rest, for particles at rest (e.g., decay at rest) with virtual method AtRestDoIt;

(2) along step, which implements behaviour such as energy loss or secondary particle production that happen continuously along a step (e.g., Cherenkov radiation) with virtual method AlongStepDoIt;

(3) post step, which is invoked at the end of the step (e.g., secondary particle production by a decay or interaction) with virtual method PostStepDoIt.[12]

Along step actions take place cumulatively, while the others are exclusive. The tracking handles each type of action in turn. Each physics process has a GetPhysicalInteractionLength, which proposes a step, and a DoIt method that carries out the action. The tracking scans all physics processes and actions for the given particle, and decides which one is to be invoked.
[12]

Particle decay: The step length (or life time for the at rest action) is straightforwardly calculated from the mean life of the particle. The generation of decay products is more difficult, using a knowledge of branching ratios and, for 3 or more body decays, theory or parameter or data driven distributions[12].
Electromagnetic physics: Geant4 electromagnetic physics manages the electromagnetic interactions of leptons, photons, hadrons and ions.The electromagnetic package is organised as a set of class categories as follows[12].

- standard: handling basic processes for electron, positron, photon and hadron interactions;
- low energy: providing alternative models extended down to lower energies than the standard category;

- muons: handling muon interactions;
- X-rays: providing specific code for X-ray physics;
- optical: providing specific code for optical photons;
- utils: collecting utility classes used by the other categories.

alternative physics models, obeying the same process abstract interface, are often available for a given type of interaction;
The package includes the processes of ionisation, bremsstrahlung, multiple scattering, Compton and Rayleigh scattering, photo-electric effect,pair conversion, annihilation, synchrotron and transition radiation, scintillation, refraction, reflection, absorption and Cherenkov effect.[12]

Standard Electromagnetic Process: The class G4eIonisation calculates for electrons and positrons the energy loss contribution due to ionisation and simulates the discrete part of the ionisation, namely the Moller and Bhabha scattering and δ-ray production. For each material and for e^+ and e^-; it produces an energy loss, range and inverse range table. The class G4eBremsstrahlung computes the energy loss contribution due to soft bremsstrahlung and simulates the discrete or hard bremsstrahlung. These two physics processes are closely connected by the design adopted. For the electromagnetic processes of hadrons, the G4hIonisation class computes the continuous energy loss and simulates δ-ray production. In this case, energy loss, range and inverse range tables are constructed only for proton and anti-proton; the energy loss for other charged hadrons are computed from these tables at the scaled kinetic energy[12]

Low Energy Electromagnetic Processes: This class category adopts a more complex design approach, by distinguishing the concepts of physics-process and model. A physics process may aggregate various components, each one being represented by a model; models can play complementary or alternative roles. A strategy design pattern is adopted to define the family of physics models, encapsulate them and make them interchangeable. Example is ,for instance, in the low energy hadron ionisation

process (G4hLowEnergyIonisation) where a strategy pattern handles the complementary models of energy lossBethe-Bloch, parameterisation, free electron gas, quantum harmonic oscillatordepending on the energy range and charge of the incident particle. Other strategy patterns handle the models for electronic and nuclear stopping power respectively, while energy loss fluctuation models are treated separately[12].

Muons Category is modelled on standard category. The energy loss of muons is computed by the class G4MuEnergyLoss using a scheme of computation which is the same as in the case of e^+/e^- : The G4MuIonisation class computes the contribution to the continuous energy loss due to ionisation and simulates the corresponding discrete process, knock-on electron or d-ray production. The G4MuBremsstrahlung class calculates the continuous loss due to soft bremsstrahlung and simulates discrete, hard bremsstrahlung[12]. The G4MuPairProduction class gives the contribution to the continuous energy loss due to soft e^+/e^- pairs and performs the simulation of pair production.The features of energy loss are very similar for e^+/e^- ; μ^+/μ^- and charged hadrons so, by design, a common description for them has been adopted. The continuous energy loss is calculated as a sum of the contributions of the different processes. It also proposes a step that, by the mechanism of choosing the smallest step described above, limits the step of all processes in order to preserve precision in a situation where the energy is changing along the step; for example, the stopping range may be required to decrease by not more than some fraction of the total ionisation range, if this limit is not less than some finalRange parameter[12].

Hadronic physics Given the vast number of possible modelling approaches, they have chosen to design an additional set of implementation frameworks to help generate the corresponding code in a distributed manner, and allow significant flexibility to the final user. Further details maybe found at

http://geant4.web.cern.ch/geant4/UserDocumentation/UsersGuides/ForApplicationDevel
fo/BookForAppliDev.pdf

and

http://geant4.web.cern.ch/geant4/UserDocumentation/UsersGuides/PhysicsReferenceMan
BackupVersions/V10.1/fo/PhysicsReferenceManual.pdf

3.2 Physics Processes We Used

There are predefined physics process from the previous section. For our simulation we use such physics lists. We used QGSP_BERT and Shielding Physics List.All of the Geant4 reference physics lists, including Shielding and FTFP_BERT, are templated code which makes it difficult to know which processes, models and cross sections are in use at a given energy for a given particle.

QGSP_BERT

QGSP is the basic physics list applying the quark gluon string model for high energy interactions of protons, neutrons, pions, and Kaons and nuclei. The high energy interaction creates an exited nucleus, which is passed to the precompound model modeling the nuclear de-excitation. And it uses Bertini cascade for primary protons, neutrons, pions and Kaons below ≈10GeV. The Bertini model produces more secondary neutrons and protons than the LEP model, yielding a better agreement to experimental data.

One can refer to http://geant4.cern.ch/support/proc_mod_catalog/physics_lists/hadronic/QGSP_BERT.html for specific classes of hardonic processes used.

Shielding Physics List

The Shielding physics list was originally developed for neutron penetration studies and ion-ion collisions, but it may also be used for high energy calorimetry and for underground or low background experiments. Its high energy part is taken from the FTFP_BERT physics list and radioactive decay has been added to deal with background radiation The detailed description is given in http://www.slac.stanford.edu/comp/physics/geant4/slac_physics_lists/shielding/physlistdoc.html

Chapter 4

RPC Simulation using Geant4

4.1 Setting up the Particle Gun

We created the detector model in the Detector Constructor Class as described previously. Now we have to setup the Primary Event Generator Class which is inherited from G4VUserPrimaryGeneratorAction Class for setting up the particles, position, momentum etc. First you create an object of the G4ParticleGun Class and in the method PrimaryGeneratorAction you setup the particle gun. From G4ParticleTable class we find the particle we want to incident using the method FindParticle() and set this to the object from G4ParticleDefinition class. Pass it on to the SetParticleDefinition method from G4ParticleGun class object that you had earlier created. You can set the momentum and energy of the G4PaticleGun object using SetParticleMomentumDirection and SetParticleEnergy method respectively.

```
G4int n_particle = 1;
fParticleGun  = new G4ParticleGun(n_particle);
G4ParticleTable* particleTable = G4ParticleTable::GetParticleTable();
G4String particleName;
G4ParticleDefinition* particle
  = particleTable->FindParticle(particleName="proton");
fParticleGun->SetParticleDefinition(particle);
fParticleGun->SetParticleMomentumDirection(G4ThreeVector(0.,0.,1.));
```

```
fParticleGun->SetParticleEnergy(6.*MeV);
```

Now you want to set the position of the particle gun.For this we call the method SetParticlePosition on the object of the G4ParticleGun class earlier created and set the position using a G4ThreeVector. This is done inside GeneratePrimaries method of the PrimaryGeneratorAction class. Then you call GeneratePrimaryVertex method to create the primary vertex for the particle and pass on a G4Event Object to it. For the RPC we set the position of the gun to (0,0,-10). The momentum is set to (0,0,1) which is the +z axis. The particle and the energy will be changed using macro files.

```
G4double x0 = 0;//size * envSizeXY * (G4UniformRand()-0.5);
G4double y0 = 0;//size * envSizeXY * (G4UniformRand()-0.5);
G4double z0 = -10*cm;

fParticleGun->SetParticlePosition(G4ThreeVector(x0,y0,z0));

fParticleGun->GeneratePrimaryVertex(anEvent);
```

4.2 GUI image of the Simulation

After this you should have setup the basics to run the simulation. Opening the GUI of the simulation you can see the RPC detector in grey color.Giving the command to run the beam ("BeamOn") for a few protons the GUI calculates and shows the trajectories of the particle and the duaghter particles. The end result is shown in figure 4.1. Here the particle is proton and the energy is 10 GeV.

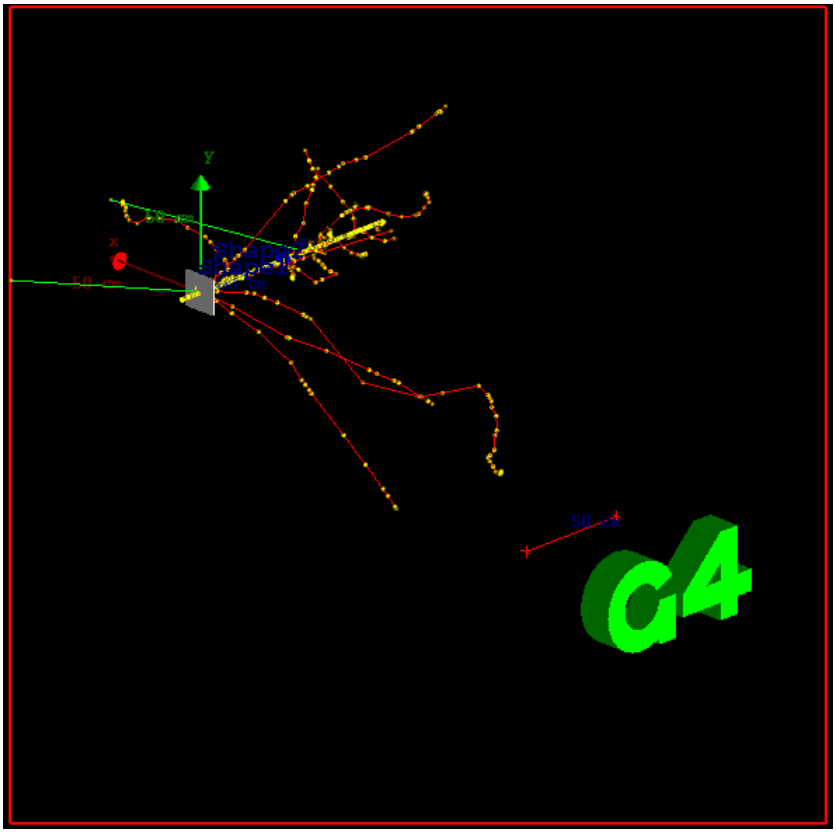

Figure 4.1: Simulation of RPC with 10GeV protons.

The yellow dots represents the points of interactions of the particle. Green lines are neutral particles produced. Red lines are for negative particles and blue are for positive particles.

4.3 Paticles at Different Energies

First thing we do is to run simulation for different particles at various energies and plot the energy distribution. This is done in figures 4.2, 4.3, 4.4, 4.5 for proton, muon+, kaon+, pion+ respectively. Each simulation is done for 100k events with the gap thickness of 2mm and the Ar:CO_2 ratio is 70:30.

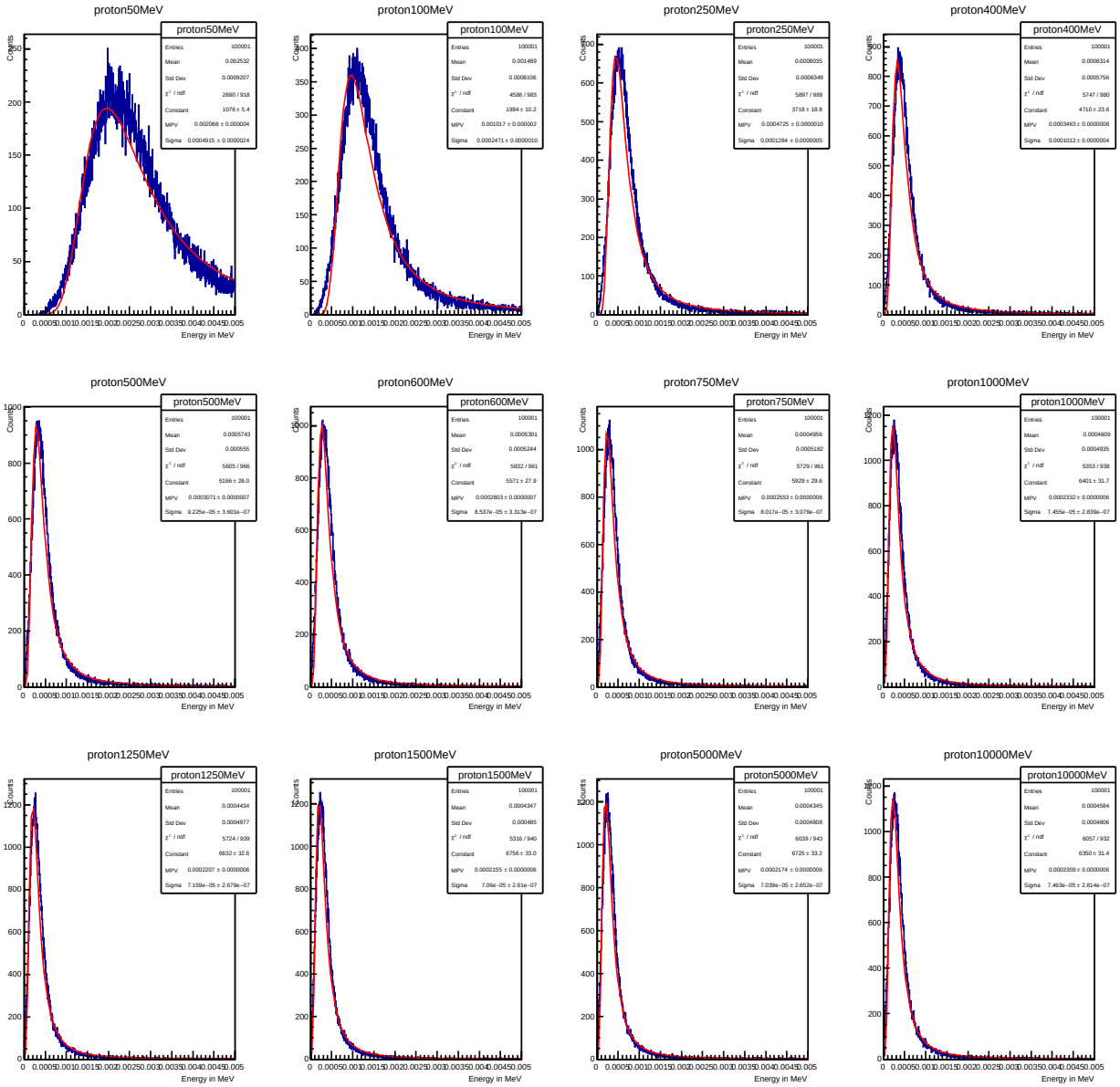

Figure 4.2: Simulation of RPC with Protons 2mm thickness and 70:30 ratio($Ar:CO_2$).

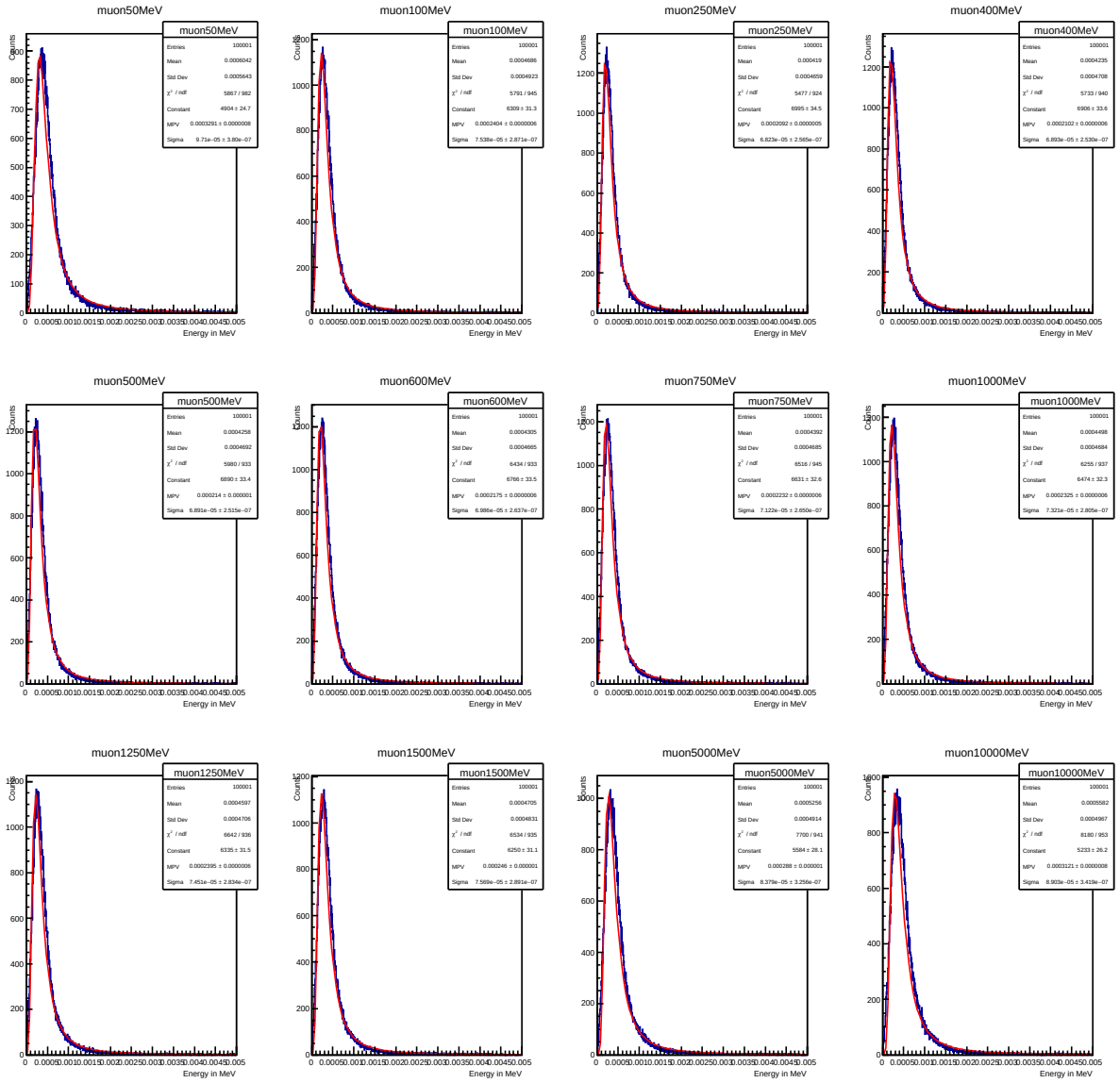

Figure 4.3: Simulation of RPC with Muon 2mm thickness and 70:30 ratio($Ar:CO_2$).

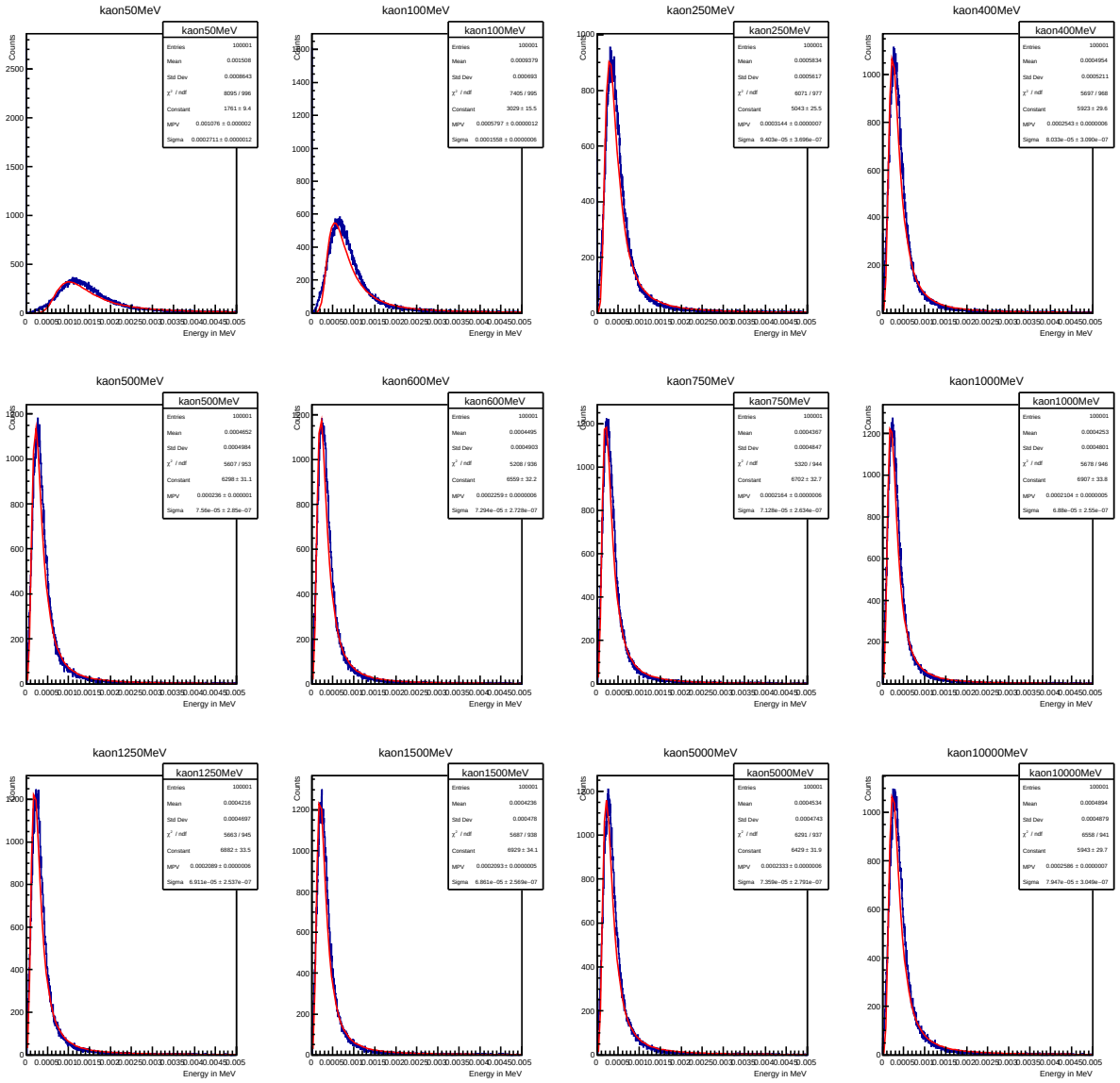

Figure 4.4: Simulation of RPC with Kaon 2mm thickness and 70:30 ratio($Ar:CO_2$).

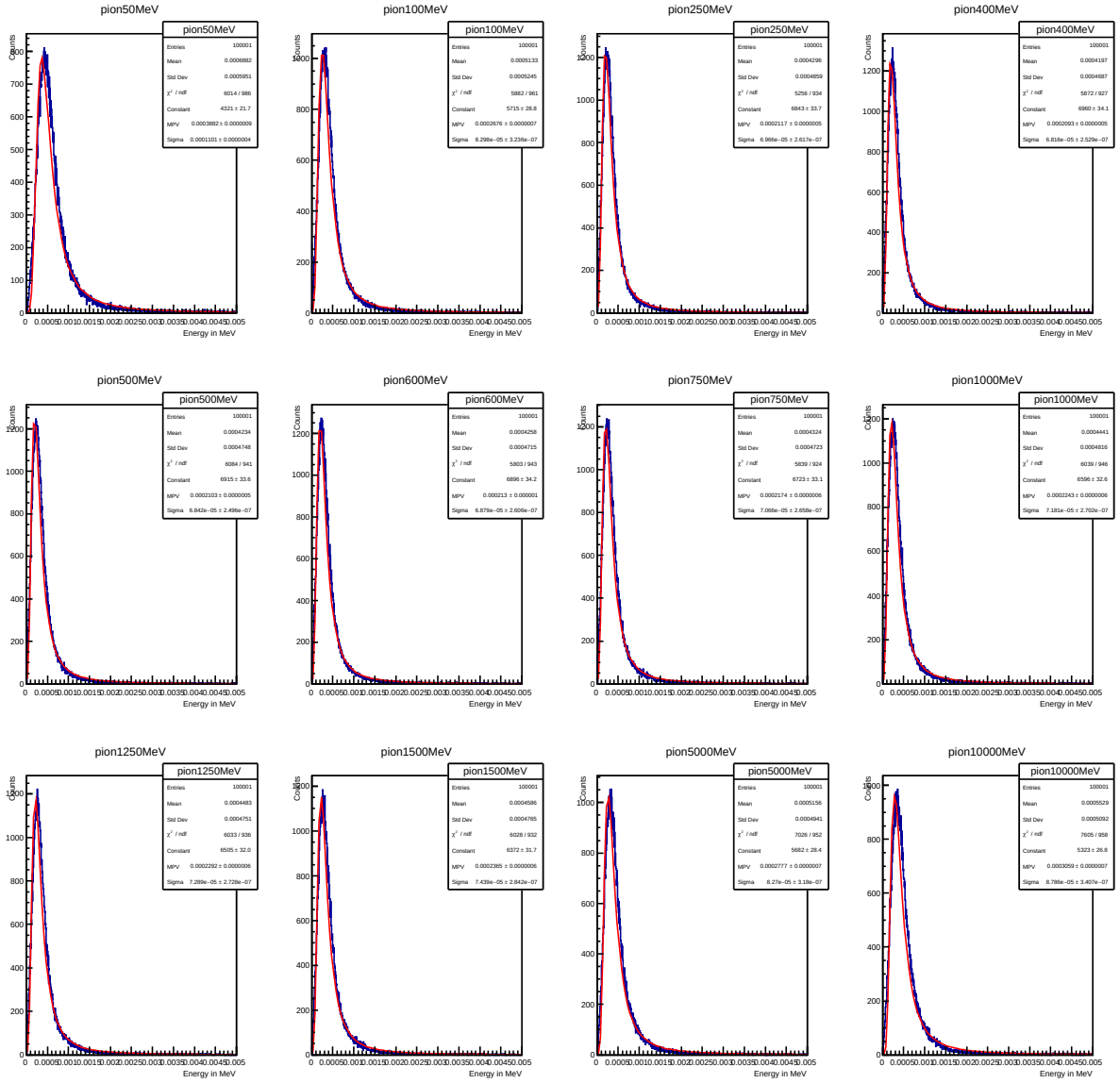

Figure 4.5: Simulation of RPC with Pion 2mm thickness and 70:30 ratio($Ar:CO_2$).

The general trend here is that for higher energy projectile that does not suffer many collisions, can be described by a asymmetric distribution curve called the Landau distribution. This is the case when the absorber is thin or the projectile energy is comparatively high.

On the contrary when the projectile energy is comparatively less that it suffers many collisions, the distribution tends to be a Gaussian distribution because of the Central

Limit Theorem. We can see this clearly for 50 and 100 MeV Kaon + and Proton + in figure 4.4 and 4.2 respectively. For Muon+ and Pion+, because of their low mass values their β values are comparatively larger hence they suffer less collsions.

4.3.1 Mean Energy Deposited

Now, if we can compare the mean energy lost at different energies for different particles we should get something similar to figure 1.5. That is exactly what we get and is shown in figure 4.6

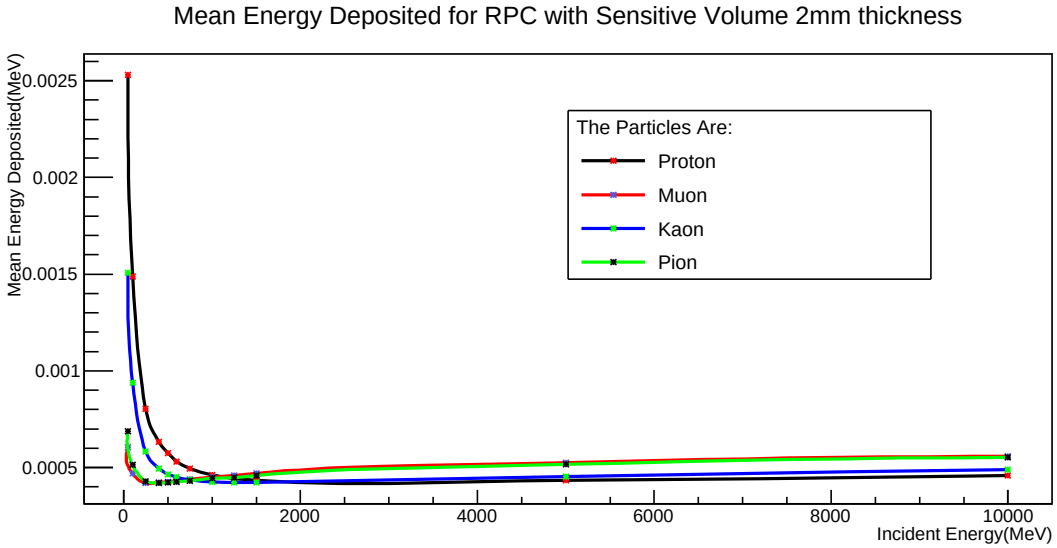

Figure 4.6: Average Energy Deposited in 2mm thickness and 70:30 ratio(Ar:CO_2) for Different Particles.

4.4 Concentrations of CO_2 in Ar-CO_2 mixture

Changing the mixture of the scoring volume gas should have an impact on energy loss as we see that the CO_2 and Ar have different energy loss curves from figure 1.8 and 1.9.

Plotting the average energy deposition for different incident energies yield similar results as that of 1.8 and 1.9. As the concentration of CO_2 increases, the energy deposition tends towards the CO_2 side of the energy loss curve(more energy loss at 100%). This can be seen in figure 4.7

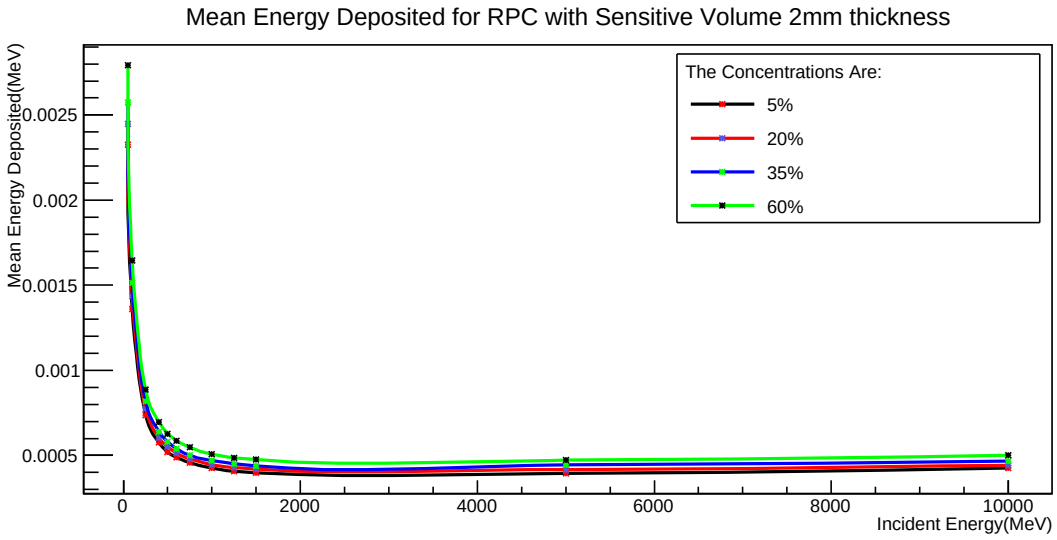

Figure 4.7: Average Energy Deposited in 2mm thickness vs Incident Energy for different CO_2 concentrations Ar-CO_2 Mix by Protons

Similarly if we were to check the variation of energy depostion with concentration for different energies we should get a straight line which is what figure 4.8 is showing.

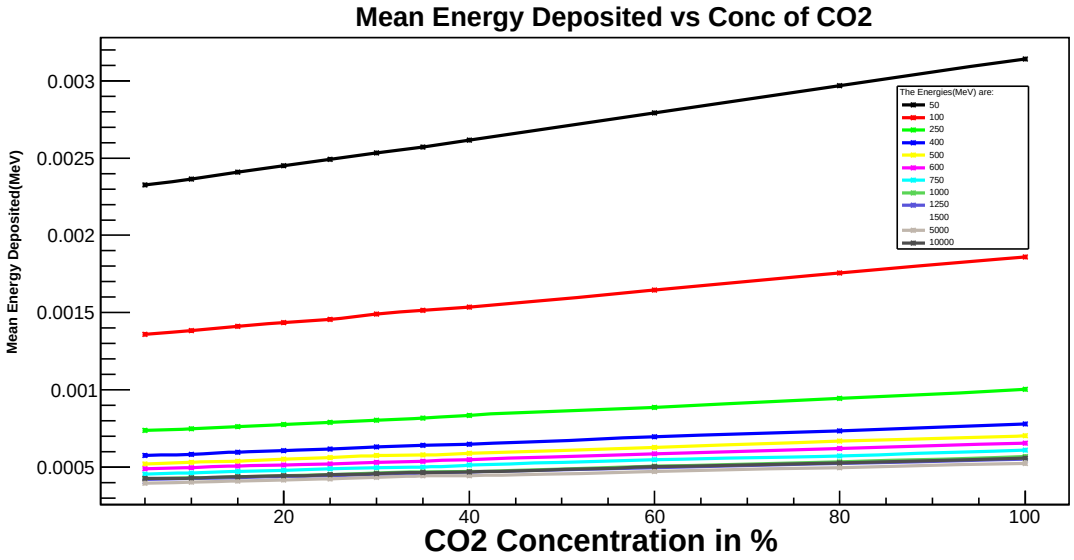

Figure 4.8: Average Energy Deposited in 2mm thickness vs CO_2 concentrations at different incident energies of proton

4.5 Thickness of the Gas volume containing Ar-CO_2 mixture

Another variable to test is the thickness of the gas volume. Increasing this would mean more collisions leading to more energy loss. Figure 4.9 shows the average energy loss curves at different thickness's of the absorber at 70:30 concentration of Ar:CO_2.

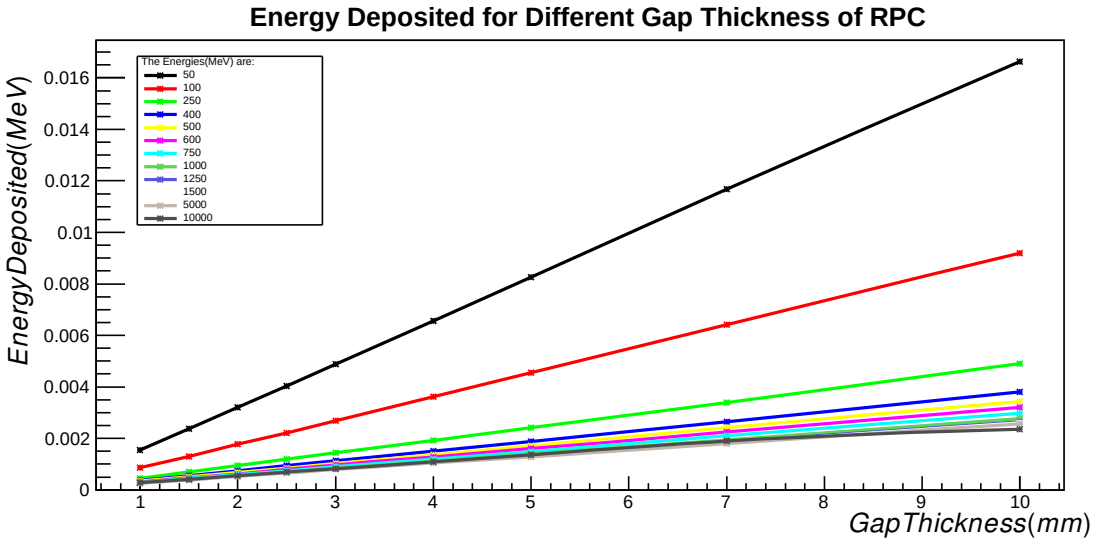

Figure 4.9: Average Energy Deposited vs Thickness of gas volume at different incident energies of proton

Here you can see that the trend is a straight line with positive slope, the value of which varies with different incident energies; the highest being for 50MeV. This may be due to the fact that as the thickness increases, the energy loss also increases, which reduces the β value of the incident particle and at lower energies the change in these values are higher.Like a cascade effect this leads to more energy loss for lower energy particles and as a result the energy loss increases rapidly as the thickness increases for lower energies.

Finally, figure 4.10 shows that the energy deposited curve is not only shifted up when the thickness is increased. You can observe as you decrease the energy the energy deposited increases faster for thicker gas gaps. Because particle will lose energy faster in thicker gaps as you lower incident energy.

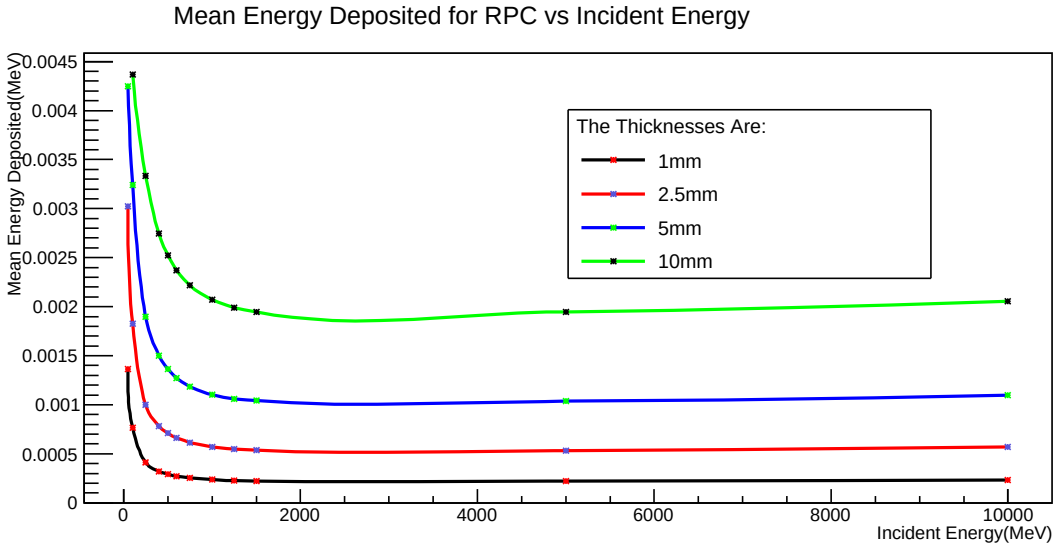

Figure 4.10: Average Energy Deposited vs Incident Energies at different Thickness's of gas volume for proton

Chapter 5

Interaction of Photons with Matter

We studied the charged particle interaction with matter in Chapter 1 mainly considering the inelastic Coulombic Scattering of the particle with the electrons of the target media. However, the interaction of photons in matter is dramatically different compared to the interaction of charged particles. In this chapter we shall mainly focus on the several electromagnetic processes that are involved in the characterization of energy deposition of photons in matter. Unlike charged particles, which release energy all along their trajectory in a trail of ionizing collisions, photons interact with matter in a single encounter, with or without the creation of secondary particles[5].

If the target medium is atomic gas, if the projectile energy is close to the first ionisation potential, then the absorption cross-section is greatly increased, which results in the release of a photoelectron and if the target medium is composed of molecules, the presence of mechanical excitation states(rotational or vibrational) can lead to radiationless absorption below the photo-ionization threshold[2] [5] .

After the absorption starts, till energies of a few tens of keV, the largest fraction of the energy deposited by a photon is due to photoelectric effect, resulting in the release of one or more free electrons and low energy photon[5]. After exceeding few tens of keV gases become transparent and therefore not directly used. Usually to detect the photons, there is a solid converter where the photons interact and the photo-electron released in the interaction is sent to a gas detector to be detected.

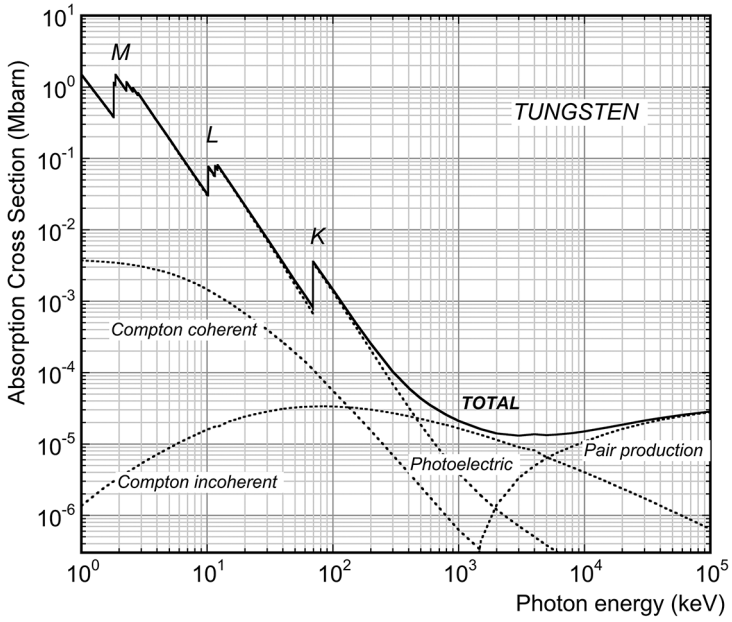

Figure 5.1: Absorption Cross-section vs Incident energy of photons for tungsten [5]

Looking at figure 5 we can see that there are peaks associated with the K,L,M shells of the medium. After each peak there is a drastic decrease in the cross-sections as their corresponding electrons are unavailable for photo-electric effect to take place. These drops are know as edges. So we can observe the K-edge, L-edge, and the M-edge in the figure 5. At higher energies the Pair-production takes over. It is easily observed that Compton scattering occurs at medium to low energies.

5.1 Photo-Absorption

The absorption of a beam of photons with single energy by a uniform layer of material thickness x is described by the exponential law[2] [5] [14]:

$$I = I_0 \exp^{-\mu\rho x} = I_0 \exp^{-\alpha x} \tag{5.1}$$

Here the I_0 is the incident photon intensity, and I is the intensity of photons leaving the target medium. μ is known as the mass absorption coefficient $[M^{-1}L^2]$, and ρ is the density of the material. $\alpha = \mu\rho$ is known as the linear absorption coefficient. It is the probability of interaction per unit length of absorber. $\lambda = \alpha^{-1}$ can be defined as the absorption length.

Theoretical Detection efficiency can be then defined by:

$$\epsilon = \frac{I_0 - I}{I_0} = 1 - \exp^{-\mu\chi} \tag{5.2}$$

Here χ is the reduced material thickness given by $\chi = \rho x$

Now considering σ to be the absorption cross-section for photoelectric effect, we see that the linear absorption coefficient is related to the cross-section by

$$\alpha = N\sigma \tag{5.3}$$

and N is the number of atoms or molecules per unit volume given by

$$N = \frac{N_A \rho}{A} \tag{5.4}$$

where N_A, ρ, A are the Avogadro number, density and the atomic weight respectively.

Now, considering molecules assuming that the constituent atomic properties remains unchanged the mass absorption coefficient can be found by the weighted sum of the individual cross-sections given by equation 5.5.

$$\mu = \frac{N_A}{M} \sum n_i \sigma_i \tag{5.5}$$

where $M = \sum n_i A_i$, n_i is the number of atoms of type i.

Similarly the absorption coefficient for mixtures can be obtained as the sum of the values of components weighted by their mass fraction.

$$\alpha = \sum \mu_i \rho_i \tag{5.6}$$

Note that the absorption coefficient and the consequent derived quantities are dependent on the incident photon wavelength.

5.2 Photoelectric Effect

It is the process by which a photon is absorbed by an atom/molecule and a corresponding photon is ejected from the same atom/molecule. The photo-electron ejected will have energy given by the equation 5.7

$$E = h\nu - B.E \tag{5.7}$$

Free electrons cannot absorb a photon as a consequence of the special theory of relativity and conservation of momentum, and hence can only take place on bound electron with the nucleus absorbing the recoil momentum. Theoretically it is very difficult to treat photoelectric effect rigorously because of the complexity of the Dirac wavefunction[2]. For incident energies above the K-shell ionisation potential, majority of the electrons that participate in the photoelectric effect come from the K shell electrons[2]. Assuming only K-shell electrons participate and the incident energy is non-relativistic i.e., $h\nu = m_e c^2$, the cross-section can be calculated using born approximation[2] and is given by equation 5.8

$$\Phi_{photo} = 4\alpha^4\sqrt{2}Z^5\Phi_0(\frac{m_e c^2}{h\nu})^{7/2}\text{per atom.} \tag{5.8}$$

where $\alpha = 1/137$ is the fine structure constant, $\Phi_0 = 8\pi r_e^2/3 = 6.651 \times 10^{-25} cm^2$

Now, for incident energies that are closer to the K-edge(absorption edge) equation 5.8 must be multiplied by a correction factor. Then the cross-section becomes

$$\Phi_{photo} = \Phi_0 2^7 \pi Z^{-2}(137)^3\left[\frac{\nu_k}{\nu}\right]^4 \frac{\exp(-4\xi\cot^{-1}\xi)}{1-\exp(-2\pi\xi)}\text{per atom.} \tag{5.9}$$

where $h\nu_k = (Z-0.03)^2 m_e c^2\alpha^2/2 \approx$ Binding Energy of the K-shell and $\xi = \sqrt{\dfrac{\nu_k}{\nu-\nu_k}}$.

For example Argon has $h\nu_k \approx 4.3$keV. Later when we build a proportional counter we will use equation 5.8 to find the photocross-section as the incident energy of the photon is $\approx$ 17.5 keV hence ν is not at all close to ν_k and energy is greater than K-edge.

Now, if ν was close to ν_k then equation 5.9 becomes

$$\Phi_{photo} = \frac{6.3\times10^{-18}}{Z^2}\left(\frac{\nu_k}{\nu}\right)^{8/3} \tag{5.10}$$

One can note from 5.9 that close to the K-edge, the cross-section depends on the atomic number via an inverse square law. However at MeV energies of this dependence changes to Z^4 or Z^5 as can be seen from equation 5.8 [2]. Then higher Z materials are favoured for detecting photons.

5.3 Compton Scattering

Compton scattering is the process by which a photon gets scattered by a free electron and the exchange in momenta is reflected on the photon by its change in wavelength. In figure 5.3 the photon of energy $h\nu$ is incident on a free electron. The photon gets scattered with the new frequency ν and an angle ϕ.

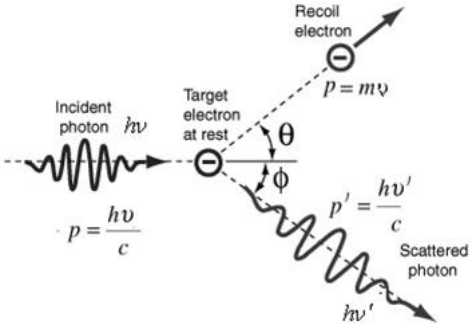

Figure 5.2: Compton Scattering Process[15]

One can solve Compton scattering problem just by applying the conservation of energy and momentum (look at figure 5.3) we get the following relation.

$$h\nu' = \frac{h\nu}{1 + \frac{h\nu}{m_e c^2}(1 - \cos\theta)} \tag{5.11}$$

We are more interested in the cross-section of the Compton scattering happening. Given in equation 5.12 is the Klein-Nishina formula which was calculated using quantum chromo-dynamics.

$$\frac{d\sigma}{d\Omega} = \frac{r_e^2}{2} \frac{1}{[1 + \gamma(1 - \cos\theta)]^2} \left(1 + \cos^2\theta + \frac{\gamma^2(1 - \cos\theta)^2}{1 + \gamma(1 - \cos\theta)}\right) \tag{5.12}$$

Here r_e is the classical electron radius and $\gamma = \frac{h\nu}{m_e c^2}$ Integration of this formula over all solid angle $d\Omega$ will give the total cross-section of Compton scattering

$$\sigma_c = 2\pi r_e^2 \left\{ \frac{1+\gamma}{\gamma^2} \left[\frac{2(1+\gamma)}{1+2\gamma} - \frac{1}{\gamma} \ln(1+2\gamma) \right] + \frac{1}{2\gamma} \ln(1+2\gamma) - \frac{1+3\gamma}{(1+2\gamma)^2} \right\} \tag{5.13}$$

5.4 Pair Production

It is the process by which a photon is converted usually in the presence of a nucleus into an electron-positron pair. The presence of a third body is required in order to conserve linear momentum. For this process to occur, the photon must have a minimum energy of 1.022 MeV. Since the photon energy that we deal with will be few tens of keV, we shall not go into further details.

Chapter 6

Interaction of Neutrons with Matter

Unlike charged particles, neutrons are not subjected to Coulomb interaction with the electrons and nuclei of the target medium. The principle method of energy loss in matter for neutrons is through strong force. And since the strong force is short range, the cross-section of these interactions are rather small leading to comparatively rarer collision events. The energy of the neutrons are deposited only when the neutrons come in close proximity to the nucleus, typically of the order of 10^{-15}m and because the normal matter is usually empty space, the neutrons are highly penetrating particles[2]. Note that unlike photons, the secondary radiations from the neutron interactions are almost always heavy charged particles[3]. Majority of the neutron detectors today employ some kind of conversion method of the incident neutron into secondary charged particle, which is later detected with much greater ease.

6.1 Processes of Neutron Interaction with Matter.

1. **Elastic scattering** from the nuclei. Energy loss of the neutron in MeV range is mostly due to this process.

2. **Inelastic scattering** from the nuclei. In this particular process, the incoming neutron excites the nucleus, and the nucleus may later decay by gamma-ray or some other form of radiative emission[2]. Only neutrons with energy more than a certain energy threshold (usually in the order of 1 MeV) can excite the

nucleus. Neutron with energy lower than this suffer elastic collisions with the nucleus.

3. **Radiative Capture** into the nuclei, where the neutron is captured into the nucleus. The nuclear reaction follows as: n + (Z,A) $\rightarrow \gamma$ + (Z,A+1). The cross-section for this roughly goes as inverse of the velocity of the neutron ($\frac{1}{v}$), hence at lower energies absorption cross-sections are more. Resonance peaks may also be super-imposed on this $\frac{1}{v}$ dependence.

4. **Other Nuclear Reactions** where the neutron is captured and charged particles are emitted can also be an interaction channel although this occurs at relatively low energies. Here also, there is a $\frac{1}{v}$ dependence in the cross-section which can be super-imposed on resonance peaks.

5. **High energy hadron shower** may also be produced at very high energies typically for energies greater than 100 MeV.

Since the cross-sections for the neutron interaction with matter varies dramatically with increasing energy, it is common practise to classify them bases on their energy. Broadly we can classify them into two major categories.

1. Slow Neutrons

2. Fast Neutrons

6.1.1 Slow Neutrons

These neutrons mostly undergo elastic scattering with absorber nuclei as well as undergo different neutron induced nuclear reactions. In elastic interactions very little energy is transferred to the absorber nucleus, hence cannot be used as a method for detecting neutrons even though they are very probable. Such elastic collisions often bring the slow neutrons into thermal equilibrium with the absorber material.[3] Hence most of the slow energy range neutrons will be found in thermal equilibrium which is usually called thermal neutrons and have an average energy of 25 meV at room temperature. There is a category of interactions where slow neutron can be detected.

These slow neutron can induce secondary particles through nuclear reactions with sufficient energy which can be directly detected. Slow neutrons undergoing radiative capture can release gamma particles which can be detected through activation foils, although they are not widely used since it is hard to detect gamma rays. Interaction where secondary particles with charges that are induces are much more favoured since they can be directly detected.

6.1.2 Fast Neutrons

The cross-section of neutron induced reactions that are useful in detecting the neutrons drops of dramatically with the increase in neutron energy as discussed earlier. But, since the fast moving neutrons suffer collisions which can transfer considerable amount of energy, nuclear recoils can occur which can be detected. Here the secondary radiations are the recoiled nuclei. After each such collisions the neutrons lose energy and are slowed or moderated. hence fast neutrons entering matter will undergo collisions, both elastic and inelastic, losing energy till thermal equilibrium is reached with the absorber material. One of the most efficient moderator is hydrogen, which can have interaction with the neutrons such that most of the neutron energy will be lost in a single collision. The recoil proton from such collisions can be directly detected making hydrogen one of the most preferred medium for fast neutron detections.

6.1.3 Scattering of Fast Neutrons

As discussed above the major mechanism of scattering is elastic in the fast neutron regime, and this problem maybe treated non-relativistically with very simple conservation laws.[2].

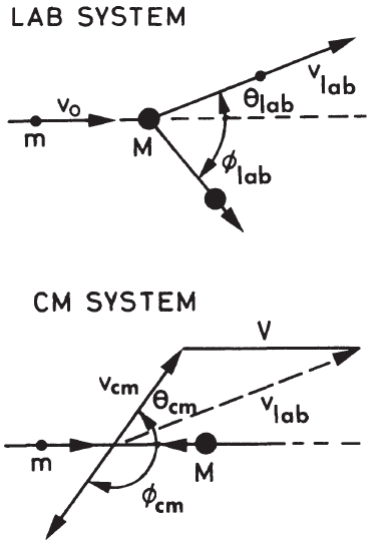

Figure 6.1: Elastic Scattering of a Neutron on a nucleus of mass M[2]

We shall treat this derivation[2] in units of neutron mass to make things simpler. That implies that $m_n = 1$. Then mass of the nucleus is just the mass number A. One may refer to figure 6.1 for the conventions. Considering center of mass system, the velocity of the neutron becomes:

$$v_{cm} = \frac{A}{A+1} v_0 \tag{6.1}$$

Here the nucleus takes the velocity

$$V_{nuc} = \frac{1}{A+1} v_0 \tag{6.2}$$

The magnitude of the velocity of the neutron remains unchanged in the CM frame. Then using trigonometry, the velocity of neutron in the lab frame becomes

$$(v_{lab})^2 = (v_{cm})^2 + V_{nuc}^2 - 2 v_{cm} V \cos(\pi - \theta_{cm}) \tag{6.3}$$

substituting 6.1 and 6.2 into 6.3 we get

$$(v_{lab})^2 = (\frac{A}{A+1} v_0)^2 + (\frac{1}{A+1} v_0)^2 - 2\frac{A}{(A+1)^2} v_0^2 \cos(\pi - \theta_{cm}) \tag{6.4}$$

Ratio of the K.E becomes

$$\frac{E}{E_0} = \left(\frac{v_{lab}}{v_{v_0}}\right)^2 = \frac{A^2 + 1 + 2A\cos\theta_{cm}}{(A+1)^2} \tag{6.5}$$

Looking at 6.5, we can easily deduce that the energy is bounded by

$$\left(\frac{A-1}{A+1}\right)^2 E_0 < E < E_0 \tag{6.6}$$

when we put $\cos\theta_{cm} = \pm 1$.

In the case of Hydrogen as discussed in the above case putting A=1 we get

$$0 < E < E_0 \tag{6.7}$$

This implies that the neutron can lose all its energy to the hydrogen nucleus. Hence the lighter the nucleus, the more energy it absorbs.

6.1.4 Other Classification

An isotope of cadmium, ^{113}Cd, absorbs neutrons below a certain threshold of energy. Because of this neutrons with energy below the cadmium cut-off are classified as slow neutrons and are differentiated from the intermediate and fast neutrons. Looking at figure 6.2 we can see the high selectivity of Cd. Note that the value of this cut-off is around 0.5 eV.

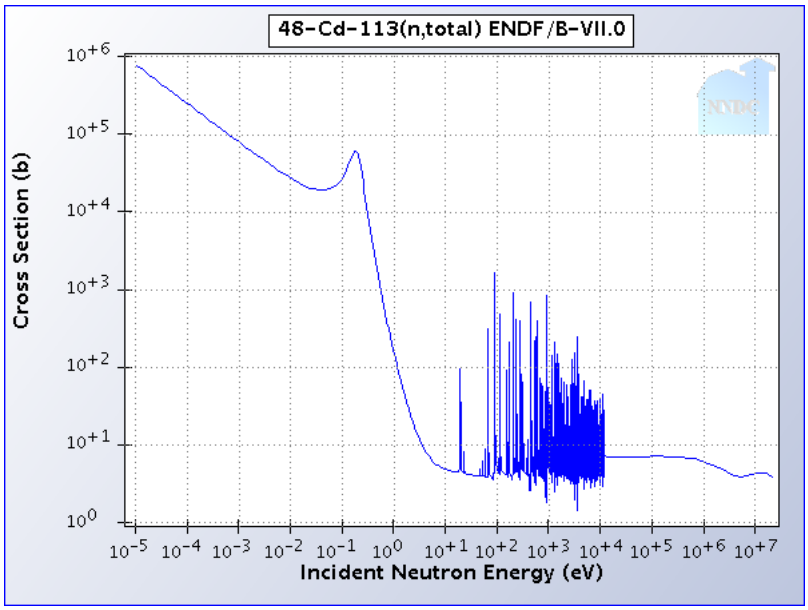

Figure 6.2: Cadmium Cut-off [16]

Typical Classification	Energy Range
High Energy Neutrons	>100 MeV
Fast Neutrons	10MeV-100keV
Epithermal Neutrons	100keV - 0.1eV
Slow Neutrons	>0.5eV
Thermal Neutrons	0.25meV
Ultra Cold Neutrons	$\approx \mu$eV

Table 6.1: Classification of Neutrons

Table 6.1 shows the different classification of Neutrons. Note that the Epithermal Neutrons are where the Nuclear resonance reactions occur.

Chapter 7

Design and Simulation of Double Windowed Proportional Counter

7.1 Aim

To design a double windowed Proportional counter for real-time photon count measurement of 17.5 keV X-rays from Molybdenum source.

7.2 Design

The design of the Proportional counter is made keeping in mind that a small fraction of X-rays entering it should deposit enough energy to produce a signal (ionize the target gas), and a large fraction should exit the detector on the other side so that real-time measurement of the source strength can be done simultaneously while performing experiments. To achieve this, we simulate a test geometry in Geant4 and optimize the length and the target gas to achieve a balance of both efficiency and transmission rate.

Here we design the initial geometry and we choose the well studied cylindrical geometry with the following modifications.

1) The two flat faces of the cylinder will be used as the windows which will be closed by kapton tape for the X-ray to come in and go out.

2) The anode wire will be held in the middle of the cylinder by two holsters 3D printed positioned near the flat faces at the two sides.

3) High voltage will be supplied to the anode wire by means of a coaxial wire from the HV connector placed in the middle of the detector.

Stainless Steel(SS) is chosen as the material for the cylinder as stainless steel pipes are easily available as well as they are durable. Anode holders are 3D printed using plastic. The SHV holder is also made from stainless steel pipe. The detector length is chosen after simulating the geometry. Figure 7.1 shows the solid view of the initial design. There are two holes that are meant for the gas inlet and outlet. Figure 7.2 shows the wire view for a better understanding of the design.

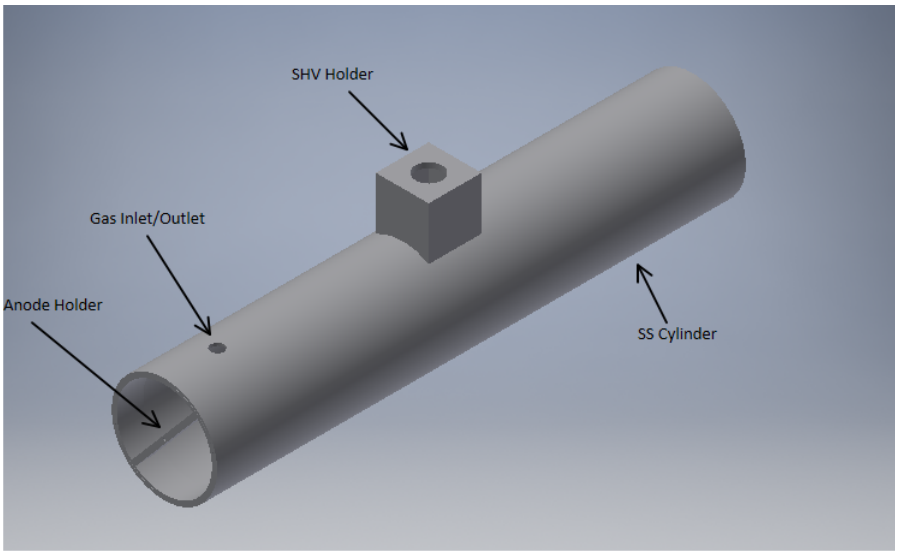

Figure 7.1: Solid view of Detector Geometry

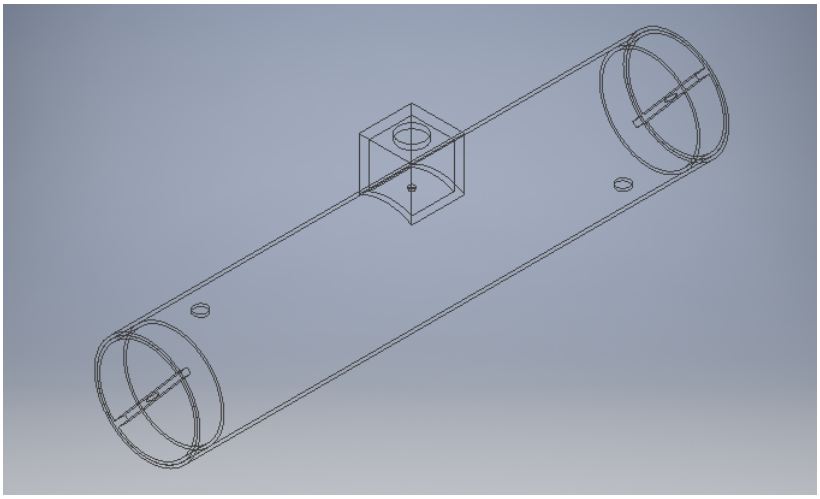

Figure 7.2: Wire view of Detector Geometry

The chamber will be sealed using epoxy adhesive. The anode wire is going to be a copper wire sealed into the holder holes at each faces of the detector. We shall seal the two flat faces of the detector using Kapton tape. Then attach two gas nozzle at the two holes meant for the gas inlet and outlet. After connecting the coaxial wire to the anode, it is taken through the hole under the SHV holder and connected to the SHV connector. Then the SHV holder would be secured in place by epoxy adhesive. Care must be taken to make sure that the two different pipes are grounded.

7.3 Simulation

7.3.1 Specification

The simulation is done using Geant4. The above geometry is constructed in Geant4 using G4Tub class. The source code for the simulation can be found here. Stainless Steel material was constructed using the following code.

```
G4NistManager* nist = G4NistManager::Instance();
G4Element* Cr = nist->FindOrBuildElement("Cr");
G4Element* Mn = nist->FindOrBuildElement("Mn");
G4Element* Fe = nist->FindOrBuildElement("Fe");
G4Element* Ni = nist->FindOrBuildElement("Ni");
```

```
G4Element* Si = nist->FindOrBuildElement("Si");
G4Element* C  = nist->FindOrBuildElement("C");
G4double  density,fractionmass;
G4int ncomponents;
   G4String name;
G4Material* StainlessSteel = new G4Material("StainlessSteel", density= 8.06*g/cm3,
StainlessSteel->AddElement(C, fractionmass=0.001);
StainlessSteel->AddElement(Si, fractionmass=0.007);
StainlessSteel->AddElement(Cr, fractionmass=0.18);
StainlessSteel->AddElement(Mn, fractionmass=0.01);
StainlessSteel->AddElement(Fe, fractionmass=0.712);
StainlessSteel->AddElement(Ni, fractionmass=0.09);
```

Other materials that were used were found from the class G4NistManager (Note in the above code nist is an instance of the G4NistManager) in similar was as was shown earlier in the report. For more information, one may go through the source code and the detector construction file in /src/B1DetectorConstruction.cc which can be found here.

Physics List QBBC was used with G4EMStandardPhysics Class enabled for electromagnetic processes. In this class, all common electromagnetic process that can happen to the photon, that is compton effect and photoelectric effect, is enabled.

Now for the simulation, each run consisted of 10^5 events. The mother volume was kept to be vacuum ignoring any interactions of the X-ray with air surrounding the detector. The beam dimensions were chosen to be 5mm tall by 6mm wide and in this square area used uniform random numbers to generate the photons with energy 17.5 keV. One may refer to the Primary Action Generator for more information on the particle generation and particle gun here. Note that the beam was shot at the detector away from the center as to not hit the anode holders. It was shifted by 0.5 cm.

For the simulation the Stainless Steel(SS) had a inner radius of 1 cm and outer radius of 1.1 cm. The target gas volume had a inner radius of 0.05 cm and outer

radius of 1 cm. The anode wire had an outer radius of 0.05 cm and the inner radius was zero. It was made from copper. Kapton thickness at each faces of the cylinder was kept at 0.1 mm.

The number of photons coming out of the detector volume was counted by checking the prestep volume to be in the kapton volume and the post step volume to be in the world volume. For detailed information click here to see the Stepping Action code.

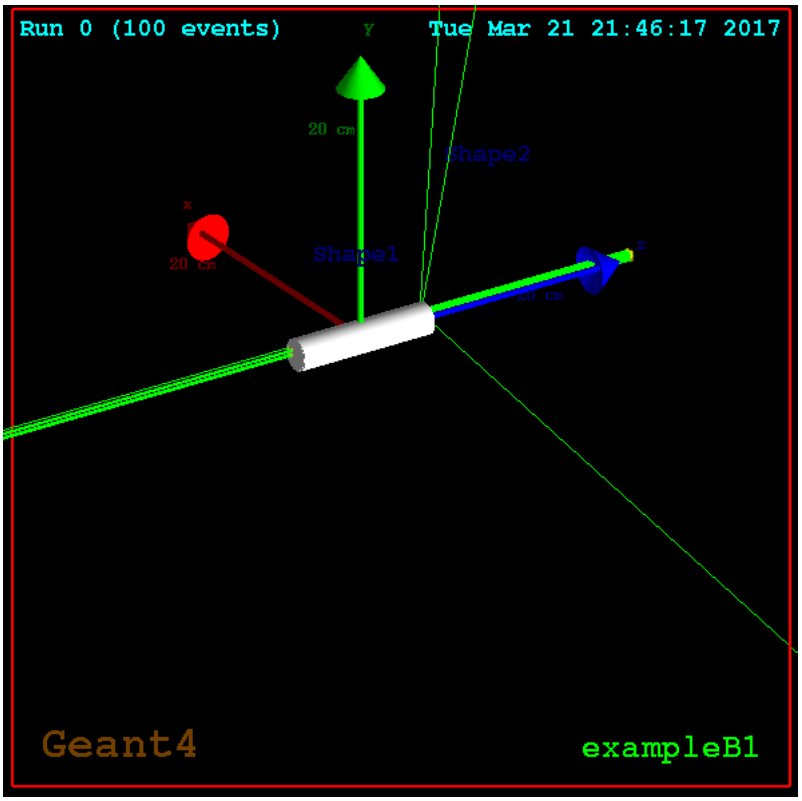

Figure 7.3: Detector being subjected to X-ray radiation

Figure 7.3 shows the X-rays coming from the right side, hitting the detector, some transmitting through. The target gas is Xe and the detector length is 10 cm.

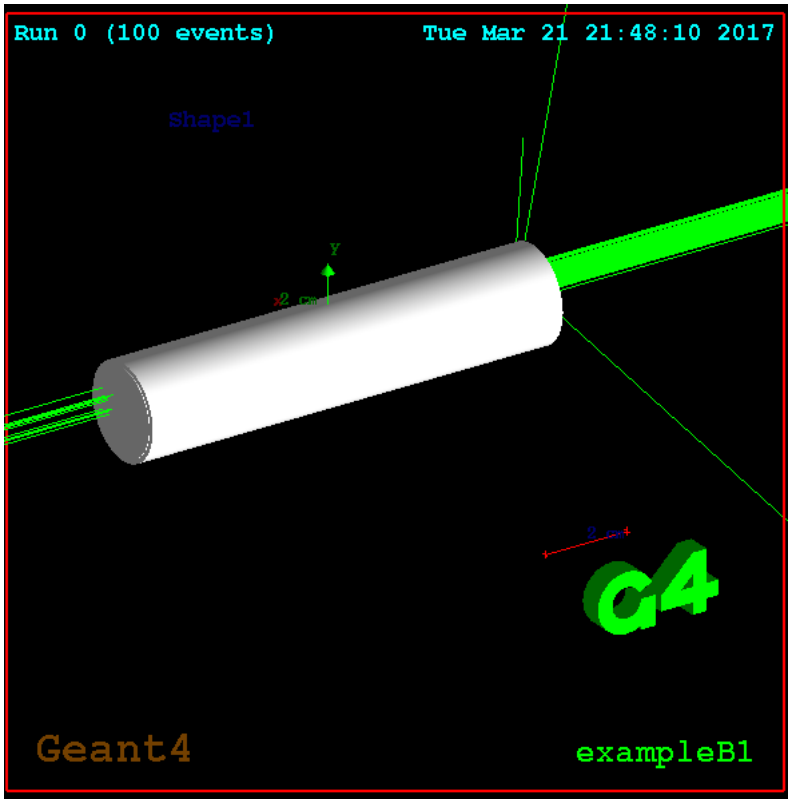

Figure 7.4: Close up of Detector being subjected to X-ray radiation

Close up of the Detector. Here you can see the shape of the beam. It is set to have 5mm width and 6mm height and shifted 0.5 cm to the + x-axis.

In figure 7.5 the detector geometry in wire mesh form is shown. One can observe the photon being absorbed and an electron being ejected. However, since the electric field has not been implemented in the simulation, the electron will be soon absorbed back into the medium itself. The electron track is shown in red.

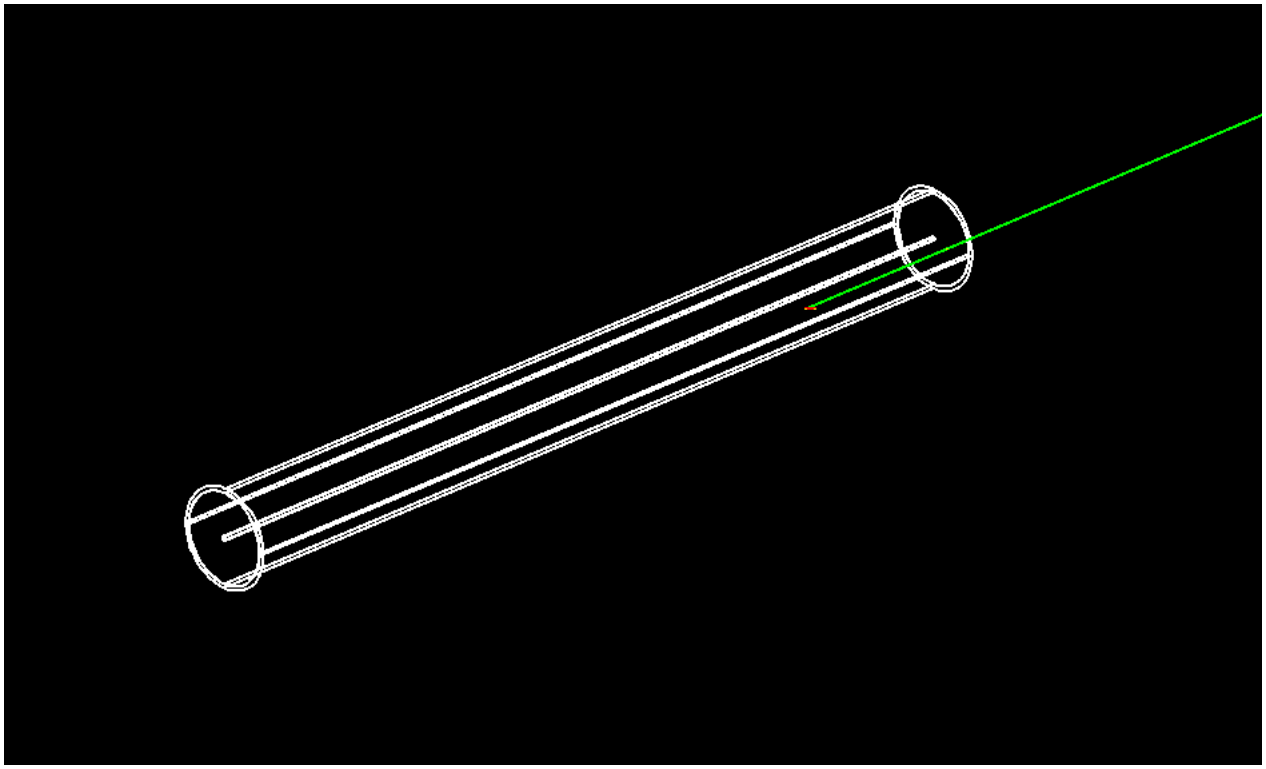

Figure 7.5: Photo-Electric Absorpbtion taking place in Xe gas

7.3.2 Observations

We shall be optimising transmission and efficiency of the detector so that we can do a real time measurement of the photon count while doing an experiment using the outgoing photons. Transmission ratio is defined by

$$T = \frac{\#\text{ of photon exiting the detector}}{\#\text{ of photons incident on the detector.}} \tag{7.1}$$

For understanding the efficiency, we will find out how many electron are being produced by each photon. And claim that if a photon produced more than or equal to one photon, that particular event will get detected. The efficiency will be

$$\eta = \frac{\#\text{of detected events}}{\#\text{ of photons incident on the detector.}} \tag{7.2}$$

And plotting these two quantities for different lengths of the detector geometry and for different target gas we get the following graphs.

Figure 7.6, 7.7, 7.8 shows the transmission and efficiency for 100k events at different detector lengths for Ar CO_2=70:30, Xenon, and Krypton respectively. One can see that the efficiency reaches very high values for Krypton and Xenon, but for Ar:CO_2 mix the maximum is 0.25 compared to the > 0.9 for the other two. The cross-section of the photo-electric absorption increases as atomic number increases, hence probability of photoelectric absorption occurring in Xe, and Kr are more compared to Ar:CO_2 mixture.

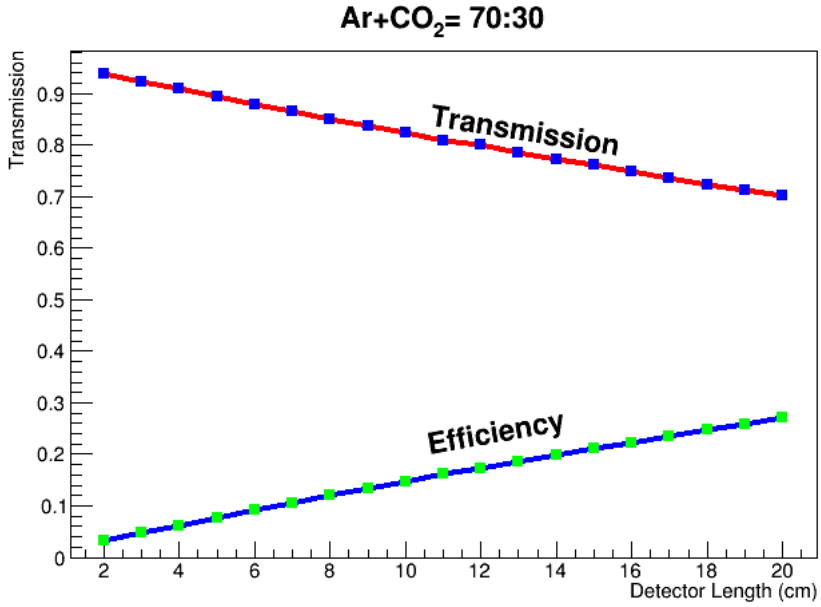

Figure 7.6: Transmission/Efficiency Graph for Ar:CO_2 Mixture (70:30)

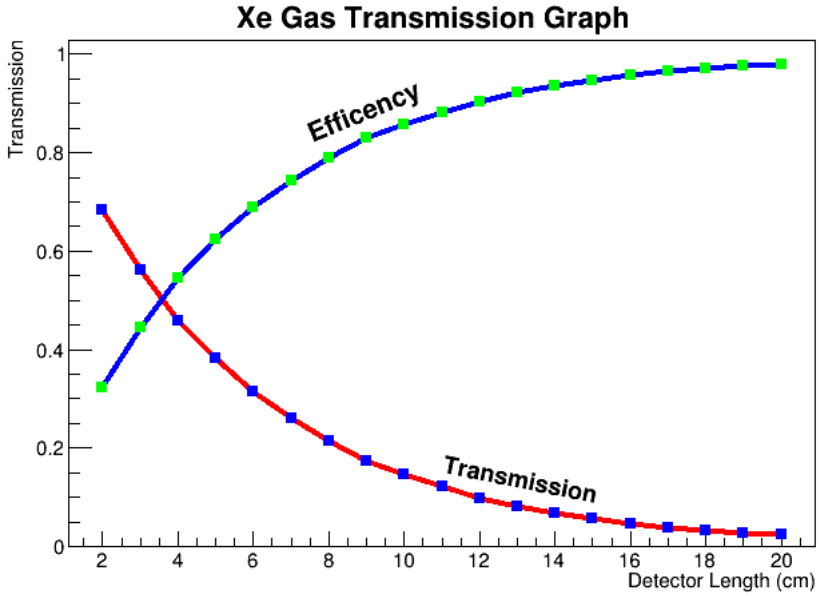

Figure 7.7: Transmission/Efficiency Graph for Xenon

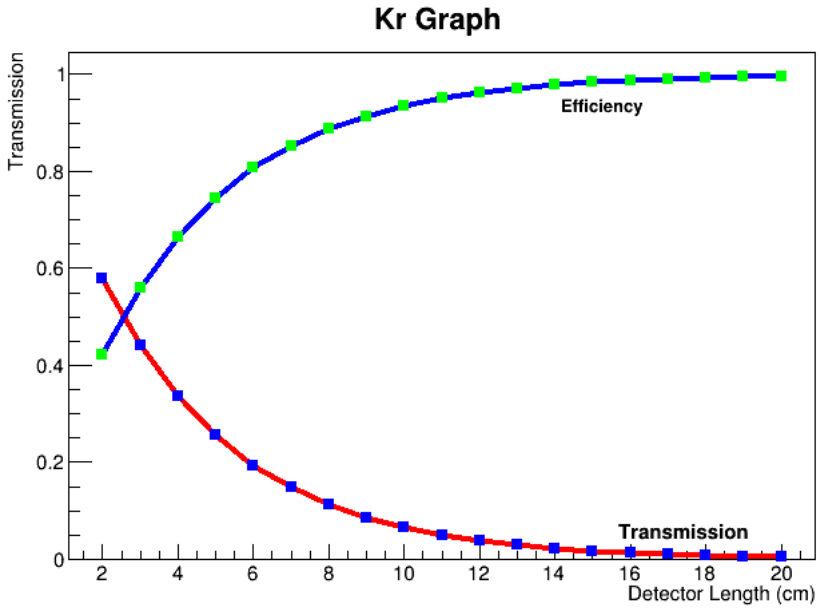

Figure 7.8: Transmission/Efficiency Graph for Krypton

7.4 Remark

After the simulation, the optimisation of transmission and the efficiency is achieved at detector length of around 10 cm in Ar+CO_2 mixture. This will give an estimated efficiency of 14.61 % and a transmission of 82.46 %. We could have used Xe, or Kr but considering the availability and the cost of the gas we will restrict ourselves to Ar+CO_2 mixture which is readily available in the lab. Out graphs are compliant with the theory we discussed in Chapter 5. Looking at equation 5.1 we can see that the transmission decays exponentially. Although the exponential decay cannot be seen in Ar:CO_2 mixture probably because the energy deposition is very less at this particular energy.

Chapter 8

Development of Double Windowed Proportional Counter

The simple proportional counters are usually used to detect low energy X-rays in the order of a few keV. Detection of slow or epithermal neutrons are also possible by filling gases with high neutron capture cross-section like BF_3 or ^3He. These devices work by collecting the ionized electrons and ions created by the passing radiation. These counters are simple to operate, cheap to manufacture, and requires little or no maintenance. They can be employed in such a way as to detect the counts while transmitting the passing radiation. Here we shall employ this proportional counter to measure the photon beam count without adversely affecting the photon transmission rate. Note that although the efficiency rate would be low, the efficiency rate would be a constant which can be measured for that particular beam efficiency, thereby correcting the counts measured by the proportional counter.

In this chapter, we shall discuss the development of the double windowed proportional counter, which aims at detecting a fraction of X-ray photons passing through it, without adversely affecting the beam count of the initial X-ray. Then, experiments which require the initial beam count of the X-rays hitting the sample and the X-rays reflected by the sample could be measured thereby revealing the properties of the sample. The initial design developed in chapter 7 had to be modified because of the constraints in the availability of materials as well as instruments which shall be mentioned in the following sections.

8.1 Working

We shall be working with a simple cylindrical proportional counter, with two thin windows of Mylar sheet for the faces of the cylinder and having conducting walls. Through the axis of symmetry we shall position a thin anode wire. The anode is connected through a middle wire which is insulated to the High Voltage V_0. Through a capacitor we extract the signal and then it is send for signal processing. Refer to figure 8.1 for the basic construction. Note that the outer wall(Cathode) is grounded.

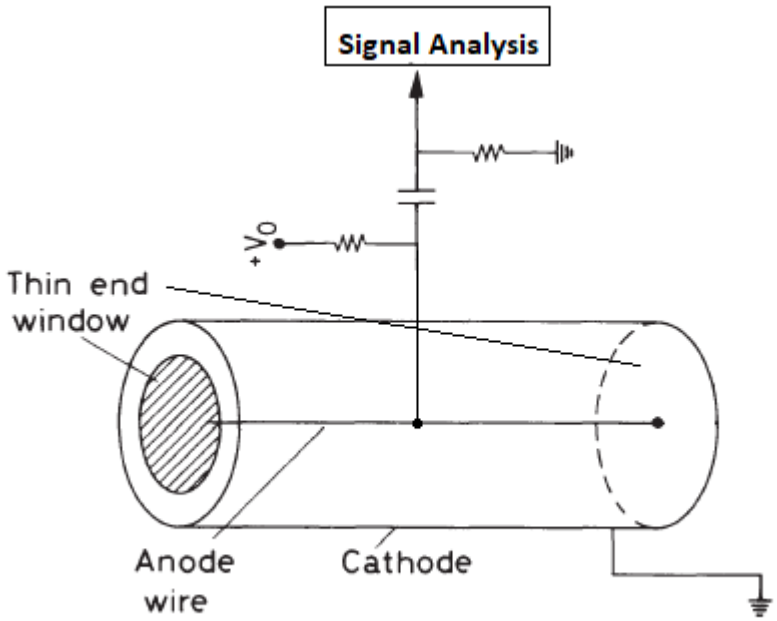

Figure 8.1: Basic Construction of the proportional Counter

This above configuration generates a radial electric field given by

$$E = \frac{1}{r}\frac{V_0}{\ln(\frac{b}{a})} \tag{8.1}$$

where r is the radial distance from the central axis of the cylinder, b is the inner radius of the cylinder, and a is the outer radius of the inner anode wire. When the radiation passes through a finite amount of electron-ion pair would be produced, for our case, mostly through photo-absorption of the photon. Because of the applied electric field,

the electrons shall be accelerated towards the anode and the ions towards the cathode where they are collected. This will induce a potential drop which passes through the capacitor attached to the anode wire towards the signal processing units.

The signal strength obviously depends on the electric field intensity. If the field is not applied, then these electron-ion pair would simply recombine, and hence no charge would be collected. As the field is increased, the recombination forces of the electron-ion pair are overcome and current begins to increase. This current would keep on increasing until all the electron-ion pairs produced are collected.

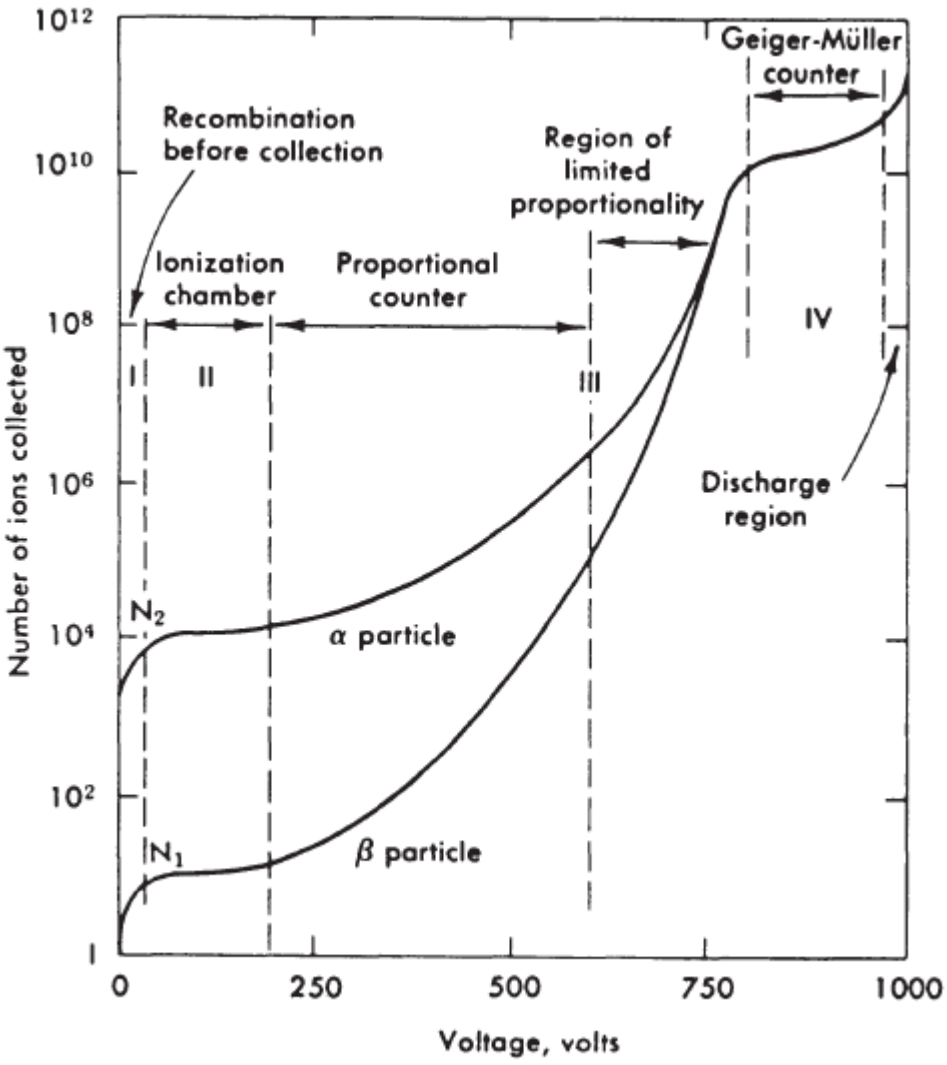

Figure 8.2: Charge collection as a functions of applied Voltage[2]

One can refer to figure 8.2 for the aforementioned phenomenon. Further increasing the voltage would not have an effect on the charges collected. This correspond to the first plateau in figure 8.2. The detector working in this region is called ionisation chamber. Ionisation chambers are generally used for measuring gamma ray exposure. If we were to increase the voltage even further, electric field would be powerful enough to accelerate the ionised electrons to an energy which can cause further ionisation. These secondary ionisations produce cascades of further ionisation resulting in an avalanche of ionizations. Since the electric field is high near the anode wire this avalanche occurs quickly and in the vicinity of the anode wire. The number of ion-electron pairs produced would be proportional to the number of primary electrons that are produced. This configuration results in a state where the proportional amplification of the current occurs, where the gain or the multiplication factor depends on the applied voltage. We shall be operating our detector at this region.

Further increasing the voltage would result in the distortion of the electric field due to the space charge created by the avalanche electron-ion produced. This is the region of limited proportionality. From here the proportionality begins to be lost. Increasing the voltage still higher would result in a chain-reaction of avalanches occurring across the entire length of the anode wire rather than a localised avalanche there by saturating the output current. These secondary avalanches are produced due to emission of photons due to the de-excitations of excited atoms which travels to other parts of the detector to produce further ionisations. These photons can be absorbed by the use of quenching gasses and the photon energy can be drenched into other channels. Detectors working in this voltage are called Gieger-Muller Counter or Breakdown counter. The Geiger voltage region is characterized by a plateau over which the count rate varies little[2]. The width of the plateau depends on the ability of the quencher gases to drain the secondary photon energies into other channels. In the last region the voltage is enough to cause ionisation even with any radiation passing through the gas where complete continuous breakdown occurs. Note that entering this region would damage the detector due to continuous discharges.

8.1.1 Drift and Mobility

After the ionisation occurs the free electrons and ions are accelerated because of the applied electric field. This acceleration is interrupted by collisions with the gas molecules, thereby creating an average velocity called the drift velocity. The charged particle effectively has this drift velocity + the thermal velocity which is random in nature. For ions the drift velocities are low due to their high mass, but electrons can attain higher velocity due to their lower mass. One can define mobility in a given electric field as

$$\mu = \frac{v}{E} \tag{8.2}$$

where v is the drift velocity of the charged particle and E is the electric field. For ions the drift velocity mostly depends linearly on the ratio of $\frac{E}{p}$ where p is the gas pressure. So constant E implies constant mobility at constant pressure. In case of the electrons, their mobility can be high as 10^6 cm/s at electric fields in the order of 1kV/cm and 1 atmospheric pressure

8.1.2 Avalanche Multiplication

In the proportional regime charge multiplication occurs due to the avalanche formation. Hence the primary ionisation is amplified by a factor called multiplication factor. Because the electrons are more mobile than the ions, the avalanche takes the form of a liquid drop with the electrons grouped near the head and the slower ions trailing behind [2]. This can be seen in figure 8.3.

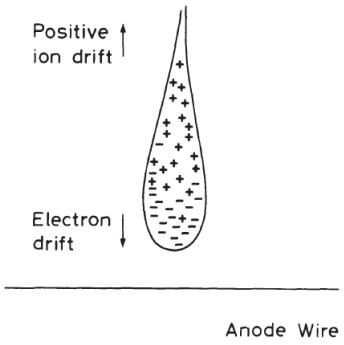

Figure 8.3: Electron liquid drop being formed near the anode. [2]

Now considering λ to be the mean free path of the electron to produce a secondary ionizing collision. Then there is a parameter given by $\alpha = \frac{1}{\lambda}$, known as the first *Townsend coefficient* which is the probability of an ionisation per unit path length. If n number of electrons are there, the number of newly ionised electrons(change in number of electron) in a path length of dx becomes

$$dn = n\alpha dx \tag{8.3}$$

Integrating this equation we get the number of electrons per path length traversed by the primary number of electron n_0 to be

$$n = n_0 \exp(\alpha x) \tag{8.4}$$

The multiplication factor then is

$$M = \frac{n}{n_0} = \exp(\alpha x) \tag{8.5}$$

Considering the case of non-uniform electric field such as in our case, we integrate to get the multiplication factor to be

$$M = \exp(\int_{r_1}^{r_2} \alpha dx) \tag{8.6}$$

There are various model available for calculating the
emphTownsend coefficient α for different gases. One such model we can use is

$$\frac{\alpha}{p} = A \exp(\frac{-Bp}{E}) \tag{8.7}$$

Here A and B are constants which depend on the gas. Knowing the Electric field of the proportional counter we can calculate the multiplication factor to be

$$M = \exp\{\frac{-D}{E}[\exp(-Eb) - \exp(-Ea)]\} \tag{8.8}$$

where $D = pA$ and $E = \dfrac{pB \ln(\frac{b}{a})}{V_0}$.

8.1.3 Choosing the Gas Mixture

There are many factor involved in choosing the gas mixture like low working voltage, high gain, good proportionality and high rate capability. For achieving the ideal factors, we generally require a mixture of gases rather than a pure one. Noble gases are chosen generally because of their low working voltage due to the avalanche formation at considerably low voltages. And due to the cheapness and high specific ionisation Argon gas is usually preferred in proportional counters.

Continuous discharge occurs if we were to use just Ar to obtain gains of more than 10^3-10^4. This is because de-excitation of Ar gives rise to photons of energy 11.6 eV(which is the excitation energy of Ar). And these photons can produce secondary electrons from the cathode metal, since this energy is usually higher than work function of the metal. Here we use Cu cathode which has a work function of 4.7 eV. This would result in unwanted avalanche formations across the detector. Solution to this problem is to mix polyatomic gases such as methane or alcohol. Inorganic gases like CO_2 and BF_3 can also be used. They will absorbs the rogue photons and dissipate this energy through other channels such as vibrational, or rotational, or through dissociation or elastic collisions. Minute amounts of these gases are required to dramatically increase the gain. These gases are called quenchers.

Gain can be further increased by using electronegative gases such as Freon, which will absorb the secondary electrons produced from the cathode before they reach the vicinity of the anode. Gains of upto 10^7 can be reached in this manner.

If we were to use organic quenchers, high fluxes of radiation would result in the dissociation of the molecule and when they combine back, they may produce solid or liquid polymers which can accumulate around the anode or cathode affecting the efficiency of the detector. The remedy to this problem is to add non-polymerization agents such as methylal or propylic alcohol or we could use inorganic gases.

In sealed gas counter there is an additional problem that one may encounter because of the large amount of quencher gas that is consumed, the operational characteristic may be affected. This problem is overcome by choosing a detector where there is continuous gas flow.

To get the ideal gas mixture, we should optimise such parameter to meet the needs of the experiment.

8.2 Design

The design of the proportional Counter had been discussed in chapter 7. We do make some alterations and those will be discussed in this section.

The material of the cylinder is going to be copper pipe instead of Stainless Steel. The following are the dimensions of the cylinder.

```
Inner Radius = 1.28 cm
Anode Wire Thickness = 0.5 mm
Cylinder Length = 10 cm
```

The anode holders were 3D printed using Polylactic Acid and from the CAD file which can be accessed from here

8.3 Simulation

After setting the parameters corresponding to our detector design(with the changes we made), we do the simulation of the detector geometry with Geant 4 toolkit. Here we observe similar result to that of the simulation that we did in chapter 7. Similar to figure 7.6 given in that chapter, we observe around 17.85 % efficiency and 79.11 % transmission at 10 cm. In figure 7.6 we see that at 10cm the transmission is around 82.46 % and efficiency is around 14.61 %. This is expected as the former is a mixture of Ar and CO_2 and the latter is pure Ar gas at STP. Not adding a quencher gas would reduce the gain of the proportional counter. The simulation of pure Ar gas is given in figure8.4

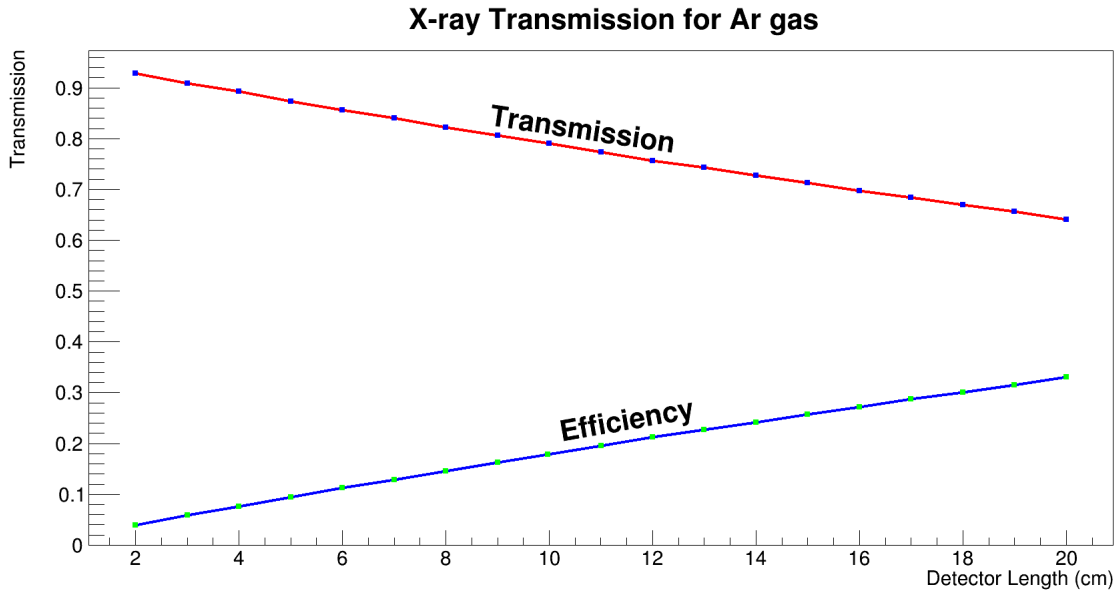

Figure 8.4: Simulation of the Efficiency and Transmission of Proportional Counter

After this we simulate to find the average energies deposited in Ar by photo-electric effect and Compton effect as given in figures 8.5 and 8.6 respectively.

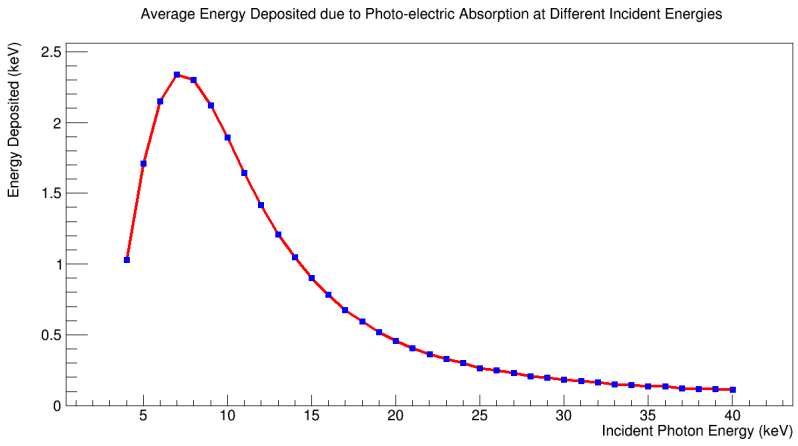

Figure 8.5: Simulation for Average Energy deposited (in Ar gas) due to Photo-electric absorption for Different Incident Energies

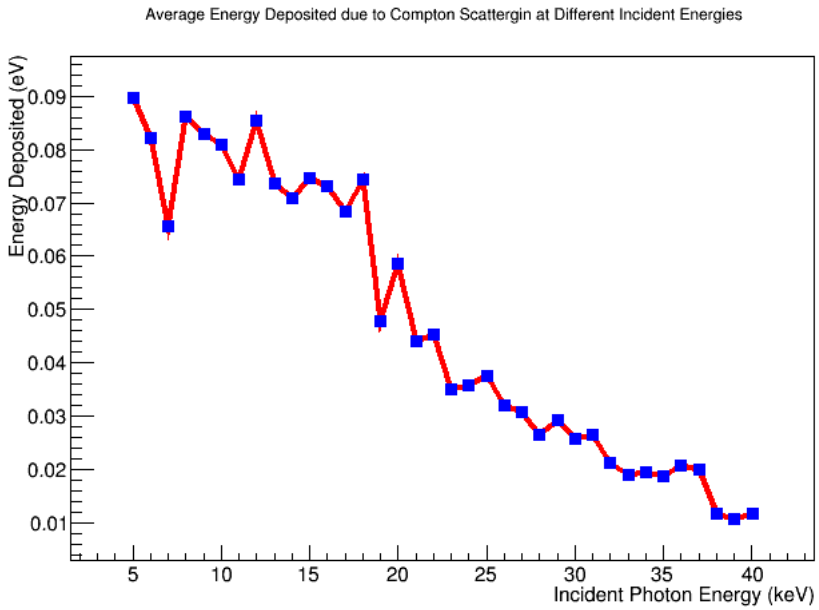

Figure 8.6: Simulation for Average Energy deposited (in Ar gas) due to Compton Scattering for Different Incident Energies

Looking at figure 8.5 the energy deposited by photo-electric effect in Ar is highest around the incident energy range of 6 keV. This gives us an indication that Ar gas detectors can have the maximum efficiency at around this energy of photons hence be used to detect X-rays of this energy range. However, we do not want every photon to be detected. Only a fraction should be detected and the rest should pass through. Hence Ar can be used in our energy range. One more thing to note is that the majority of the energy deposition occurs due to photo-electric effect.

Looking at figure 8.6 we see that the general trend is for the Compton effect to decrease at higher energy. And the Compton effect only deposits an average energy of less than a eV at these energy ranges.

8.4 Fabrication

A suitable Copper pipe of desired radial dimensions were found and was cut to 10 cm length. Another 5 cm length cylinder from the same tube was cut as well which would serve as the holder for the SHV connector. From another copper tube of outer radius

2 mm and inner radius enough for gas flow to occur two pieces of 5 cm long tubes were cut to be served as gas nozzles. In the 10 cm long tube we drilled three holes, two for the gas nozzle and one for the connection to the anode wire in the center. The two gas holes were drilled diagonally opposite to each other to ensure optimum gas flow . Figure 8.7 shows the cylinder after cutting and drilling were done.

Figure 8.7: proportional Counter after cutting and drilling holes.

All these were welded together according to the design given in chapter 7. Figure 8.8 shows the welding being done. Professional help was sought during the welding.

Figure 8.8: Welding being Done

Figure 8.9 shows the proportional Counter after the welding and cleaning.

Figure 8.9: proportional Counter after welding and Cleaning

After cleaning with sand paper, one anode holder is placed into position using araldite epoxy adhesive as can be seen from figure 8.10.

Figure 8.10: After One Anode Holder has been placed.

After this the copper wire intended for the anode wire which is at least 50 cm was brought and the enamel protection was removed. Then we wrapped another copper wire (with enamel) with Kaptop tape which acts as the connection from the SHV cable to the anode wire. Then we inserted the enamelled wire through the proportional counter and took it out through one of the faces of the cylinder after which wire was soldered onto the anode wire; This can be seen in figure 8.11.

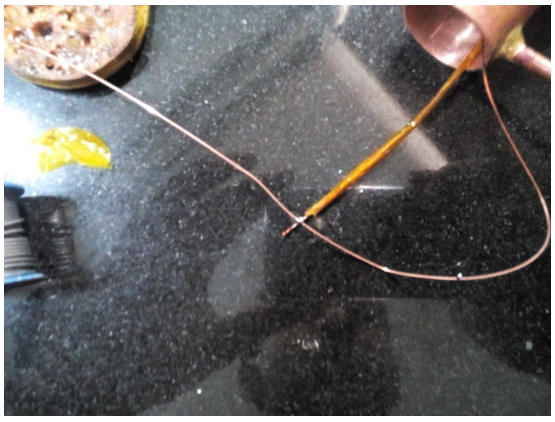

Figure 8.11: After the anode wire is soldered onto the connection wire.

Extreme caution was taken to make sure that the enamel had been completely removed. Take out the 50 cm long anode wire through both the anode holders(

remember that one is held in place by adhesive) on either sides of the detector. As we were doing this carefully, the connection wire was pulled to making sure that we did not apply excessive force. Adjustments was stopped when the anode wire was more or less aligned through the central axis.

Tying the ends of the anode wire to each of the hacksaw-blade hooks while pulling-screw was loosened up we created a setup to adjust the tension in the anode wire. Tightening the pulling-screw of the hacksaw-blade would pull anode wire straight. Figure 8.12 shows this particular trick in action. The connection wire is adjusted such that the point of contact with the anode wire is in the center of the proportional counter.

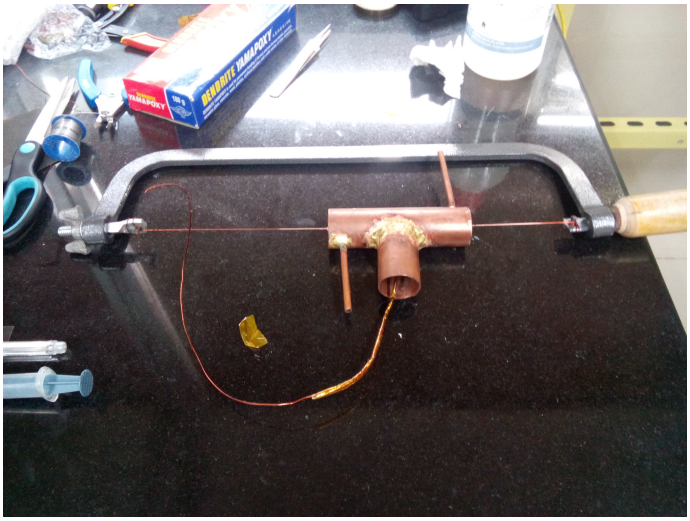

Figure 8.12: Attaching the anode wire to the hacksaw-blade holder

After this the other anode holder was placed and epoxy adhesive was applied. Figure 8.13 shows this process. Similarly the hole through which the connection wire was brought outside was also closed using epoxy adhesive ensuring that there was no gas leak(look are figure 8.14). The anode wire was also secured to the anode wire holder through the same adhesive. This was then kept in position for the adhesive to cure for more than 24 hours.

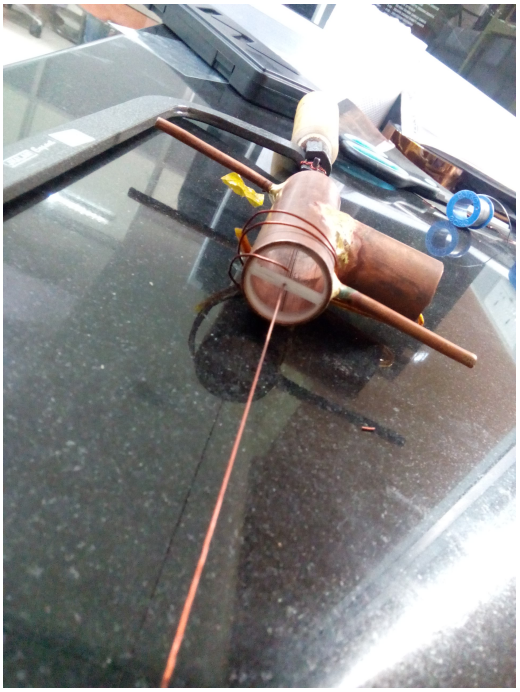

Figure 8.13: After tightening the hacksaw-blade pulling-screw, the holders are glued in place

Figure 8.14: The connection hole is closed using epoxy adhesive

After the adhesive cured, we cut the excess anode wires off. Cutting circular mylar sheets we sealed the two faces of the proportional counter again using the

epoxy adhesive. We put the m-seal to completely seal the detector, especially around the edge faces of the detector.

Now, we attach the connection-wire to the SHV connector after placing the SHV connector onto a Cu sheet (through the hole made in the dimensions of the SHV connector). Then this Cu-plate is soldered onto the main body. After making sure that all the connections made are secured using Kapton tape.

The detector after applying the conductive copper tape and some more final adjustments is shown in figure 8.15.

Figure 8.15: The detector after final adjustments

8.5 Leak Test

The gas leak of the detector is checked using Riken GH-202F Gas Leak Checker. After flowing the gas (Ar+ CO_2 at 70:30 v/v was used here) and adjusting the gas

flow rate we check for gas leak at each point where the detector has been sealed. It was found that there was no gas leaks. Having gas leaks would waste the gas, affect the flow rate of the gas. Additionally if the gas is not environment friendly, then the detector would be not suitable for operation because of the leaks. A better method for observing gas leaks would have been to use U-Tube Manometer where the change in water would indicate the gas leaks.

8.6 Flushing of Gas

The gas that was flowed through was Argon, without any quencher gas. After connecting the gas tubes to the nozzles with sealing tape and tightening the clamps we flowed the gas for atleast 4-6 hours so that the initial gases and impurities that were present inside the proportional counter were flushed out. This flow rate was continued through out the experiment. To measure the flow rate, we kept a beaker with water and dipped the exit end of the gas tube in it and monitored the bubbles that were coming out.

8.7 Coupling the Detector to the XRD Machine

The detector after the leak test was brought to X-Ray Diffractormeter facility at Institute of Physics and there it was prepared for testing. The source here is $\approx$ 17.5keV x-rays produced by a rotating target made of the Molybdenum metal. The anode (Mo) is rotating for heat management. The X-rays comes out at an angle of 6 degrees from the horizontal and using Bragg diffraction we can select the X-ray energy using a single crystal monochromator(silicon (111) that was used). Now using a NaI scintillation detector we scan for the peak and maximise the X-rays by adjusting the monochromator. The proportional counter is now placed inbetween the monochromator and the NaI detector. The angle and height of the proportional counter is adjusted and it is secured in place using adhesive tape. After maximising the counts in the NaI detector, start flushing the gas. Table 8.1 shows

Sr.No.	Accelerating Potential	Count with PC	Counts without PC	Transmission
1	20kV	2378	3109	0.76
2	30 kV	30874	40889	0.75

Table 8.1: Coupling the X-rays to Proportional Counter(PC)

Looking at 8.16, we can see the setup that was used for coupling Detector to the XRD

Figure 8.16: After flushing the detector and coupling to the XRD

8.8 Testing

The high voltage supply was connected to the proportional counter through the pre-amplifier (Model Ortec 142IH). Increasing the voltage in the reverse bias(forward bias would lead to the saturation of the preamplifier faster) started seeing noise signal (without the X-ray source) at 1000V. Keeping it at that voltage for some time usually reduced the frequency of these noise signals. Look at figure 8.17 to see the noise signal. The voltage could not be ramped up further as the preamplifier signal malfunctioned. It saturated the output signal at +10V DC drowning any signal that might have come. Note that the open gain of the amplifier is 40,000.

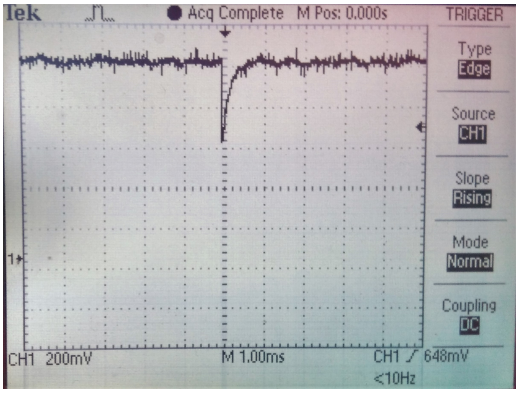

Figure 8.17: Random Fluctuation Signal

8.9 Remark

Fabrication and preliminary testing of the proportional counter was successfully done. The connectivity of the anode wire to the SHV connector was double checked after sealing the detector with M-Seal epoxy adhesive with the help of a thin wire inserted through one of the gas nozzle we find that the anode wire was connected properly to the SHV connector. The gas-leak test was done with the help of a sniffer and it was made sure that there were no leaks. The proportional counter was brought to Institute of Physics XRD facility where further testing was carried out. The gas was flushed for more than a days time, and the bias voltage was ramped up in reverse bias mode as the pre-amplifier saturated with a DC off-set in the forward bias mode. We weren't able to observe signals due to the insufficient bias voltage that was applied because the pre-amplifier malfunctioned. The High Voltage supply that was used didn't have a current measure, so we couldn't measure the current. We fabricated a high voltage capacitor using mylar sheet and aluminium foil in-order to overcome the pre-amplifier fault which is given in the appendix.

Chapter 9

Conclusion and Outlook

Our theory's main focus in the first section was on the mean energy deposition of a charged particle using Bethe-Bloch equation given by 1.32, which we derived classically using special theory of relativity. The quantum mechanical derivation introduces a $-\beta^2$ term into the equation. And the empirically calculated correction factors, that are the density correction and shell corrections, were added in which improves the energy loss at high β values and low β values respectively. These equations were studied by plotting them in different scenarios with the parameters taken from the appendix 2 of the PDG-93-06 article on energy loss in matter by heavy particles. One of the interesting finds was that the energy loss curve is characteristic of the incident particle before the minimum ionising energy and this can be used to identify particles in most cases(Goto page 15 for more info). The Bethe-Bloch gives accurate results to within a few percent for velocity from relativistic region to $\beta \simeq 0.1$. However, many assumption inherent in the energy loss equations breakdown at low energies ($\beta \leq 0.05$) , so even with corrections the equation becomes invalid in this region.

In the next section we talk about the 15x15cm^2 RPC. The fabrication procedures were successfully done, and the RPC was found to be leak proof, functional and produced a maximum efficiency of detecting the cosmic ray muons of 75.1% at 15kV. The RPC was operated in avalanche mode and no coincidence signal was found until a comparatively high bias voltage of 12kV was applied. This might be due to the fact that it was in avalanche mode and the grade of bakelite used. The bulk resistivity of

the bakelite might have been high so the effective voltage that the gap would have seen might have been less. In future experiments the bulk resistivity also have to be measured to be certain. The gas mixture that was flown through the RPC was 95.2% Freon(R134A) 4.5% Isobutane and 0.3% SF_6. The average surface resistivity on both the sides were found to be 675 $k\Omega/\Box$ & 683 $k\Omega/\Box$. The current was very unstable when we initially started to ramp-up the voltage, fluctuating by a considerable amount. After keeping the detector biased at a high voltage over a long period of time, the leakage current and the fluctuations reduced. The efficiency was measured by coincidences of signals from two other finger scintillators, and cosmic ray muons were the major contributors to the signal. The leakage current of the top and bottom electrodes were almost same, which is what we expect. The two fold count rate fluctuated because of environmental reasons like rains etc altering the cosmic ray muon flux. This might have been the reason for noise to be fluctuating as well. Efficiency saturates around 15kV bias voltage as can be seen from figure 2.13. One thing to be mentioned was that there were unequal intervals between measurements of efficiency (each measurement was done for 1800 seconds), sometimes hours. This might have been the reason for the fluctuations that you can seen in figure 2.13. We didn't coat the inside surface of the RPC with silicon oil. Doing so might have increased the efficiency of the detector by making the surface even , reducing the noise and extending the lifetime of the detector. Needless to say, the experiment was successful and served the purpose of introducing oneself to the procedures of fabricating and testing a Resistive Plate Chamber detector.

In the third section we did simulations of the RPC using Geant4 with the physics list QGSP_BERT. We constructed the detector by taking bakelite to be composed of CH_4O_2. The gas mixture that was used in the simulation was Ar:CO_2 in 70:30 v/v and incidented by proton unless otherwise mentioned . After running the simulation with different settings (different particles, concentration, thickness's) we were able to observe different trends. Firstly, EnergyLoss distribution was an asymmetric distribution called the Landau distribution and it tends towards a Gaussian distribution when the collisions increases(Incident energy is less or the thickness of the absorber is

more). Figure 4.6 show the same characteristics as figure 1.5 with the particles crossing each other at around 1GeV. Simulation and the theory hence agrees. Changing the concentration of CO_2 in the gas mixture , we find the energy loss curve to shift up or down depending on increase or decrease in CO_2 concentration. This is as expected after looking at the trend in fig 1.8 & 1.9.
And changing the thickness we see that energy loss curve becomes steeper as you decrease your incident energy. And this steepness increases as you increase the thickness of the gap. These simulations were done for 100k events with proton as incident particle.

In the fifth section we discussed the primary mechanism of photon interactions at sub 100 keV energies. As we were discussing the theory for developing a proportional counter we restrained ourselves to this aforementioned energy range. Photo-absorption was described using the exponential law, which was verified in chapter 7 during the simulation and design of the proportional counter. Photo-electric and Compton scattering theory as well as the corresponding cross-sections of occurrence were discussed.

As the part of discussing neutral particle interaction with matter we discussed neutron interactions. One of the primary tasks were to classify neutrons into two broad categories to differentiate the mechanism of energy loss leading to the different techniques used in detecting them. Using non-relativistic conservation laws we treated the elastic collisions of fast neutrons where by we came across the atomic number of the scatterer for energy deposition. We showed why Hydrogen nucleus was a good medium for absorbing the energy of the neutrons.

With the aim of developing a counter to be used in X-ray Diffractometer experiment we designed as well as simulated using Geant4 the suitable materials and dimensions of a double windowed proportional counter. Optimised values of detector transmission of 82.5% and an efficiency of 14.6 % was obtained at 10 cm length for Ar:CO_2 in 70:30 v/v mixture. Compromising the efficiency was required since we wanted high transmission rate. This was because the detector was intended to be used while the experiment was being conducted from the X-rays leaving the double windowed proportional counter.

Using chapter 7 as a guide we developed a double windowed proportional counter with some minor modifications from the original designs due to constraints. Simulation of the modified design yielded similar results as chapter 7.Simulations of the average photo-absorption energies revealed that average energy deposited was the highest for Ar at around 6 keV range implying that we can make a highly efficient detector with Ar for photons of this energy. And average energy deposited due to Compton scattering reduced at higher incident energies and was less than 1 eV. The efficiency increased to 17.85 % and the transmission decreased to 79.11 %. This is because we changed the gas mixture from Ar:CO_2 to pure Ar. Fabrication was successfully done and preliminary tests were done. After which we flushed the gas and coupled the detector to the XRD Machine. We measure the Count rate with and without the Proportional Counter which lead to the observed transmission of $\approx 76\%$. Biasing was done, gradually ramping up the voltage. Around 1000 V in the reverse bias, we observed noise signals which has been reported. Due to the malfunction of the pre-amp further ramping up was terminated and was not able to observe any signals from X-ray source. We fabricated a high voltage capacitor using mylar sheet and aluminium foil in-order to overcome the pre-amplifier fault which is given in the appendix.

9.1 Outlook

We should start by testing the proportional counter and finding the optimum working voltage. Then the detector can be tested for time resolution, transmission ratio, dead-time etcetera. The gas mixture of the detector can be then optimised even further to give more signal to noise ratio as well as other desired parameters. The gas flow can be stopped and we can check the degradation of the efficiency with time. If the degradation is found to be not there, we can permanently seal the detector. Simulation of the electric field that was applied was not done. We can extend out current simulation results by including the electric field using Garfield programme.

We had discussed the interaction mechanism of neutrons with matter. We can fill the proportional counter with BF_3 or ^{3}He gas to develop a detector to detect fast

neutrons. Simulations could be done on these detectors with Geant4 and compared with the theory we discussed.

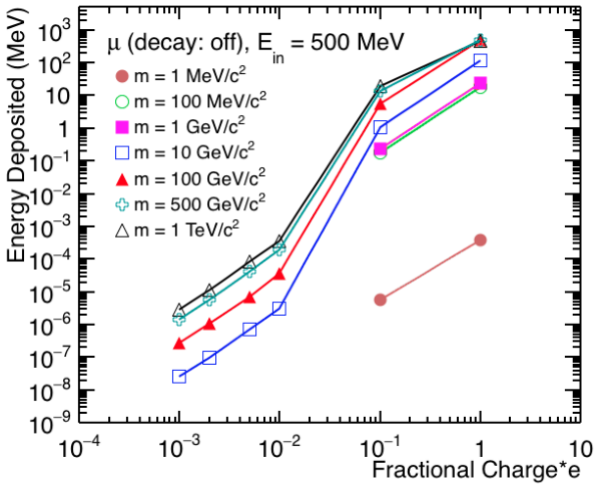

Figure 9.1: Average Energy Loss vs Fractional Charge [17]

Lastly, simulation of the "elusive" fractionally-charged-particles which can be a possible candidate for dark matter can be done. We shall be making the geometry of the Germanium detector(in Geant4) which is the detector that will be used for Super CDMS experiment in SNOLAB. And shall be experimenting with muon-like particles with fractional charges of different masses incidented on Ge Detectors and study the background from neutrons as well. According to the Bethe-Bloch Equation, the energy loss goes as a function of (z^2) but the profile looks somewhat similar to figure 9.1 which is a simulation taken from one of the LIPS Analysis talks.

References

[1] *Principles of Radiation Interaction in Matter and Detection*
by Claude Leroy and Pier-Giorgio Rancoita

[2] *Techniques in Nuclear and Particle Physics Experiment*
by W.R Leo

[3] *Radiation Detection and Measurement*
by Glenn F. Knoll

[4] *Particle Detectors*
by Claus Grupen and Boris Shwartz

[5] *Gaseous Radiation Detectors*
by Fabio Sauli

[6] *Energy Loss in Matter by Heavy Particles*
Particle Data Group Notes, Don Groom, Lawrence Berkeley Laboratory.

[7] *Design and Characterisation Studies of Resistive Plate Chambers*
by Satyanarayana Bheesette, IIT Bombay, India

[8] *Building of a Bakelite Resistive Plate Chamber Prototype*
by Himangshu Neog, Sharmili Rudra, M.R. Bhuyan, S. Biswas, B. Mohanty,Rudranarayan Mohanty, P.K. Sahu and S. Sahu

[9] *Development of High Resolution Gas Filled Detectors for High Energy Physics Experiments*
by Saikat Biswas, University of Calcutta

[10] *First Direct Limits on Lightly Ionizing Particles with Electric Charge Less than e/6* R. Agnese et al. (CDMS Collaboration)Phys. Rev. Lett. 114, 111302 Published 18 March 2015

[11] *Geant4a simulation toolkit*
Geant4 Collaboration http://dx.doi.org/10.1016/S0168-9002(03)01368-8

[12] *Geant4 User's Guide: For Application Developers*
http://geant4.web.cern.ch/geant4/UserDocumentation/UsersGuides/ForApplicationDeveloper/fo/BookForAppliDev.pdf

[13] *Geant4 Physics Reference Manual*
http://geant4.web.cern.ch/geant4/UserDocumentation/UsersGuides/PhysicsReferenceManual/BackupVersions/V10.1/fo/PhysicsReferenceManual.pdf

[14] **Gamma-Ray Absorption Coefficients** *C M Davisson and R D. Evans Rev. Mod. Phys. 24, 79* https://doi.org/10.1103/RevModPhys.24.79

[15] Image from https://sites.google.com/site/puenggphysics/home/unit-iv/compton-effect

[16] *Nuclear Data Sheets, vol. 107, pp. 2931-3060, 2006. M.B. Chadwick, P. Oblozinsky, M. Herman at al*

[17] Presentation on *Geant4 Simulation for LIPS*
by Chitrasen Jena, NISER Bhuabaneswar.

Appendix A

Fabricating a High Voltage Capacitor for Extracting the Proportional Counter Signal

The pre-amplifier malfunctioned during the testing of the proportional counter. The malfunction was that, at voltages greater than 1000V the preamp would have a DC offset saturating the output voltage to $\pm$10V depending on the applied High Voltage (HV) Bias. While we test the preamplifier using a function generator it operated fine, implying that the high voltage capacitor that was used to extract the signal from the HV line was at fault. So we developed a high voltage capacitor using mylar sheet and aluminium foil.

Figure A.1 shows the High Voltage Capacitor that was developed. It uses a A4 sized mylar sheet as the dielectric with a rated dielectric constant of 3.7. And two Aluminium foils acts as the two metal conductors. The aluminium is cut in a way that when superposed with the mylar sheet the aluminium would be away from the edges by 1 inch to ensure there is no current leakage through the edges. The aluminium foils were secured into place via insulation tape. After which we attached copper tape onto the aluminium and soldered a wire to make the capacitor.

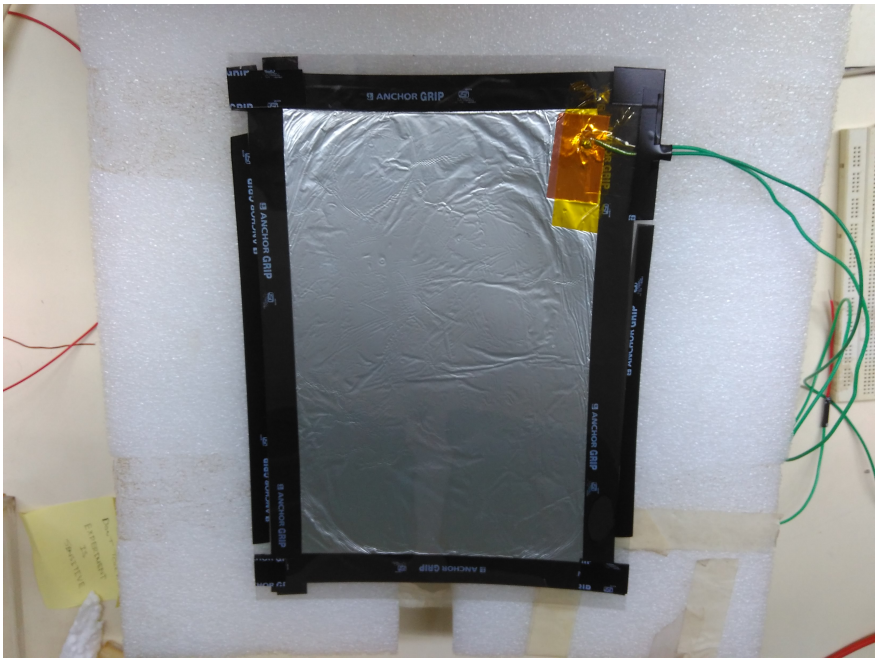

Figure A.1: High Voltage Capacitor developed using Mylar sheer and Aluminium Foil

A.1 Capacitance and Impedance

Dimensions of the mylar sheet are 210x297 mm^2 and it is 100μm thick. So calculating the effective area of 0.1592 x 0.2462 = 0.03919 m^2 Capacitance of a parallel plate capacitor is given by

$$C = \frac{\epsilon_r \epsilon A}{d} \tag{A.1}$$

here d is the separation which is 100 μm, $A = 0.03919$ m^2 is the area, $\epsilon_r = 3.7$ is the dielectric constant, and ϵ to be permittivity of free space.

The calculated C is 0.1283 nF. This will have an impedance of

$$Z = \sqrt{R^2 + (\frac{1}{\omega C})^2} = 1.24\Omega \tag{A.2}$$

considering a frequency of 10^9 Hz at R=0. In order to match the impedance of the preamp we set the R =100 Ω .

A.2 High Voltage Supply

Since we didn't have a High Voltage supply we used a Cockcroft-Walton generator of 4 stages. The effective voltage applied is 2676 V as the voltage after the first stage was measured to be 669 V. The picture of the generator is given in figure A.2. Note that the Cockroft-Walton generator was designed for 6021 V (total of 9 stages) but the voltage was taken out from stage 4.

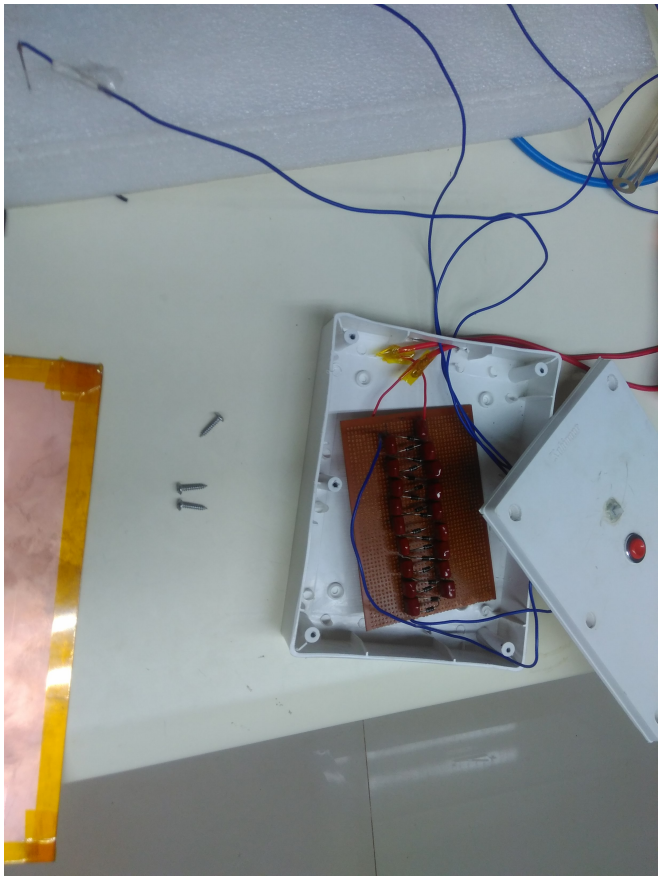

Figure A.2: Cockcroft-Walton Generator

The capacitor was tested to withstand this voltage by directly apply the voltage. There was a characteristic humming that was observed.

A.3 Testing

We connected the circuit as given in figure A.3

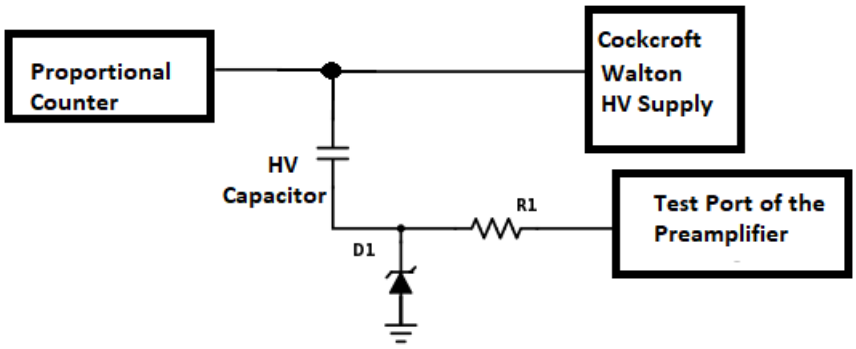

Figure A.3: Schematic of the connections made.

Here we added a zener diode in reverse bias as a safety precaution since it will keep the voltage level constant through the high voltage breakdown regime. We connected the proportional counter to the HV generator through the SHV stage made. We properly grounded the stage and the SHV connectors as well as the HV generator. Picture of the stage is given in figure A.4 as well as the other connections that were made. To the test connector we give the signal line through a BNC cable.

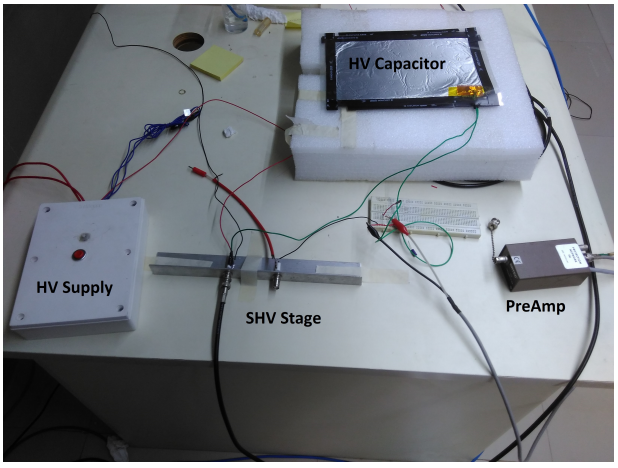

Figure A.4: Connections that were made

A.4 Results

The output was full of noise. We didn't observe any signal, through the oscilloscope. Probably if we had a stable enough HV power supply the noise would have been reduced.